11-2008

Real-Time Vertical Track Deflection Measurement System

Sheng Lu
University of Nebraska - Lincoln, lushengsam@gmail.com

REAL-TIME VERTICAL TRACK DEFLECTION MEASUREMENT SYSTEM

by

Sheng Lu

A DISSERTATION

Presented to the Faculty of
The Graduate College at the University of Nebraska
In Partial Fulfillment of Requirements
For the Degree of Doctor of Philosophy

Major: Engineering
(Mechanical Engineering)

Under the Supervision of Professor Shane M. Farritor

Lincoln, Nebraska

December, 2008

REAL-TIME VERTICAL TRACK DEFLECTION MEASUREMENT SYSTEM

Sheng Lu, Ph.D.

University of Nebraska, 2008

Adviser: Shane M. Farritor

Track quality is a major factor in railroad safety, and one accepted indicator of track quality is the vertical track deflection. Measuring track deflection from a moving railcar is difficult because there is no stable reference for the measurements.

A system developed by researchers at the University of Nebraska to measure track deflection from a moving railcar in real-time is described in detail. The system consists of a loaded hopper with a camera/laser sensor system to detect the vertical deflection of the rail relative to the wheel/rail contact point. Modeling and simulation of the system is also presented along with the mathematical models which can be used to estimate track modulus.

The measurement system has been used to conduct revenue service tests over three thousand miles of track. A special validation test was also performed. The results from these tests have shown that the system's measurement is repeatable and accurate; the system has notable ability to indicate track support problems.

ACKNOWLEDGEMENT

I would like to thank Dr. Shane Farritor, who has been a wonderful advisor and mentor. Without his guidance, none of these will be possible. Thanks to Dr. Richard Arnold who has also been a great teacher. I would also like to thank my colleagues Curt Greisen, Haoliang Duan and Cory Hogan for the help and supports during the research.

Thanks to my parents and my sister, for supporting me throughout my life. Their supports and love have been the major motivation and inspiration of my life.

This project is funded by Federal Railway Administration (FRA). Thanks to UPRR and BNSF for operational support and track access for testing.

Table of Contents

LIST OF FIGURES

1 INTRODUCTION

The economic constraints of both passenger and freight railroad traffic are moving the railroad industry to higher-speed vehicles and higher axle loads. The heavy axle loads and high speeds of modern freight trains produce high track stresses leading to quicker deterioration of track condition. As a result, the need for track maintenance increases. Fast and reliable methods are needed to identify and prioritize track in need of maintenance in order to minimize delays, avoid derailments, and reduce maintenance costs.

The condition and performance of railroad track depends on a number of different parameters. Some of the factors that influence track quality are track modulus, internal rail defects, profile, cross-level, gage, and gage restraint. Monitoring these parameters can improve safe train operation by identifying track locations that produce poor vehicle performance or derailment potential. Track monitoring also provides information for optimizing track maintenance activities by focusing activities where maintenance is critical and by selecting more effective maintenance and repair methods.

Automated methods of inspection are available for most of the parameters that are included in track geometry (Li et al, 2002). An example of an automated vehicle is the Federal Railroad Administration's (FRA) high-speed track geometry vehicle, referred to as the T-18. The T-18 is capable of measuring rail head profile, gage restraint, and other track geometry parameters (Research Results, 2001). Another example is an ultrasonic and inductive test vehicle capable of 60 mph produced by Sperry (Wanek, 2004).

However, at the present time, there is no vehicle available to measure one of the most important parameters – track modulus at normal track speeds in real-time. Track modulus is defined as the coefficient of proportionality between the rail deflection and the vertical contact pressure between the rail base and track foundation (Cai et al, 1994). In other words, track modulus is the supporting force per unit length of rail per unit rail deflection (Selig and Li, 1994). Track modulus is a single parameter that represents the effects of all of the track components under the rail (Cai et al, 1994). These components include the subgrade, ballast, subballast, ties, and tie fasteners.

Track modulus is important because it significantly affects track performance and maintenance requirements. Both low track modulus and large variations in track modulus are undesirable. Low track modulus has been shown to cause differential settlement that subsequently increases maintenance needs (Read et al, 1994; Ebersohn et al, 1993). Large variations in track modulus, such as those often found near bridges and crossings, have been shown to increase dynamic loading (Zarembski and Palese, 2003; Davis et al, 2003). Increased dynamic loading reduces the life of the track components, resulting in shorter maintenance cycles (Davis et al; 2003). It has been shown that reducing variations in track modulus at grade (i.e. road) crossings leads to better track performance and less track maintenance (Zarembski and Palese, 2003). It has also been suggested that track with a high and consistent modulus will allow for higher train speeds and therefore increase both performance and revenue (Heelis et al, 1999). Ride quality, as indicated by vertical acceleration, is also strongly dependent on track modulus.

Previous localized field testing has shown that it is possible to measure areas of low track modulus, variable track modulus, void deflection, variable total deflection, and

inconsistent rail deflection (Sussmann et al., 2001; Ebersohn and Selig, 1994). In the past, such systems have been used to identify sections of track with poor performance. These measurements have been useful. However, they are expensive and have only been made over short distances (in the range of tens of meters). The ability to make these measurements continuously over large sections of track is desirable (Ebersohn and Selig, 1994; Read et al., 1994).

Previous onboard track modulus measurement systems are similar to systems developed by the military and used in highway research (Carr, 1999). The systems use a long rigid truss that rides on two unloaded wheels. This truss creates a straight line, or cord, that is used as a reference for the measurement. A third wheel is then used to apply a load at the midpoint of the cord (or truss) and the relative displacement between the loaded wheel and the unloaded truss is measured. The truss must be long enough so that the two endpoints are not affected by the load at the center of the truss. This method requires two measurements, one with a light load, made with a similar truss, and one with a heavy load, to distinguish between changes in geometry and changes in modulus. The output of this approach is a measurement of the relative displacement of the loaded wheel with respect to the unloaded wheel. Using this measurement, track modulus is then estimated.

One vehicle, called the Track Loading Vehicle (TLV), uses this approach (Thompson and Li, 2002). This vehicle is capable of measuring track modulus at speeds up to 16.1 km/hr (10 mph). The TLV uses two cars, each with a center load bogie capable of applying loads from 4.45 kN to 267 kN (1 to 60 kips). A light load (13.3 kN or 3 kips) is applied by the first vehicle while a heavier load is applied by the second

vehicle. A laser-based system on each vehicle measures the deflections of the rail caused by the center load bogies. The test procedure involves two passes over a section of track – first applying a 44.5 kN (10 kip) load and then a 178 kN (40 kip) load (Thompson and Li, 2002).

Although the TLV is operational, it does have limitations. First, tests are often performed at speeds below 16.1 km/hr (10 mph) so it is difficult to test long sections of track (hundreds of miles). Second, significant expense in both equipment and personnel is required for operation. For these reasons the TLV has not yet been widely implemented.

This thesis presents a method to measure vertical track deflection from a moving railcar. These deflection measurements can then be used to estimate track modulus. The system uses a non-contact vision sensor system to make displacement measurements with respect to the wheel/rail contact point. The system is inexpensive and does not require significant support equipment and personnel. The system is capable of automated testing and operation at higher speeds.

2 BACKGROUND

The relationship between applied loads and track deformations is an important parameter to be considered in proper track design and maintenance. A representative mathematical model that accurately describes this relationship is desirable.

2.1 Problem Definition

Figure 2-1 shows a free-body diagram of the rail under a one-wheel load. The rail is considered as a continuously supported beam where *x* represents the distance along the beam and *w(x)* represents the vertical beam deflection. The approximation that the rail is continuously supported improves as the cross-tie spacing decreases and as the rail bending stiffness increases. The applied load, *P*, is assumed to be a point load and creates a vertical load on the rail, *q(x)*, where $P = \int_{0^-}^{0^+} q(x)dx$. The supporting structure supports the bottom of the rail with a reaction distributed force, *p(x)*. In real track, the supporting structure consists of tie plates, fasteners, cross-ties, ballast, etc. In this model the supporting structure is an infinite medium.

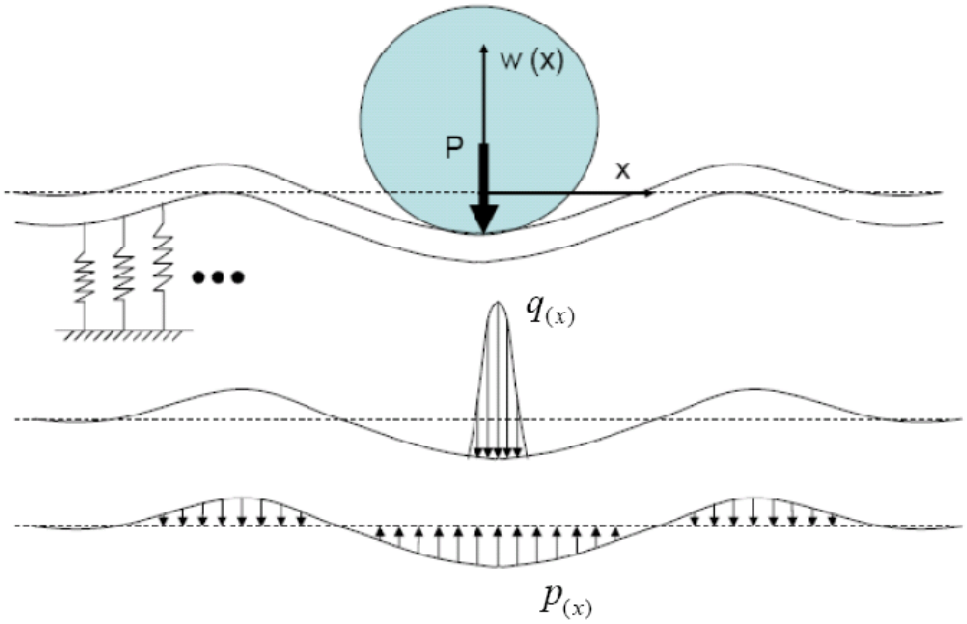

Figure 2-1: Free-body Diagram of the Rail

The difference in the vertical distributed force applied to the beam (*q(x)* - *p(x)*) causes curvature in the beam as given by the following differential equation:

$$EI\frac{d^4w}{dx^4} + p(x) = q(x) \qquad \text{Equation 2-1}$$

where:

E is the modulus of elasticity of the rail

I is the moment of inertia of the rail

x is the longitudinal distance along the rail

The solution to the differential equation is dependent upon the boundary conditions of the beam as well as the loading conditions. A free body diagram that shows sections of the beam is shown in Figure 2-2. The figure shows that the concentrated

applied load P must be supported by the foundation reaction distributed force $p(x)$ on each half of the infinite beam such that:

$$\int_0^\infty p(x)dx = \frac{P}{2} \qquad \text{Equation 2-2}$$

In addition, symmetry and the stiffness of the beam demand that the slope of the beam be zero at the point of loading.

$$\left.\frac{dw}{dx}\right|_{x=0} = 0 \qquad \text{Equation 2-3}$$

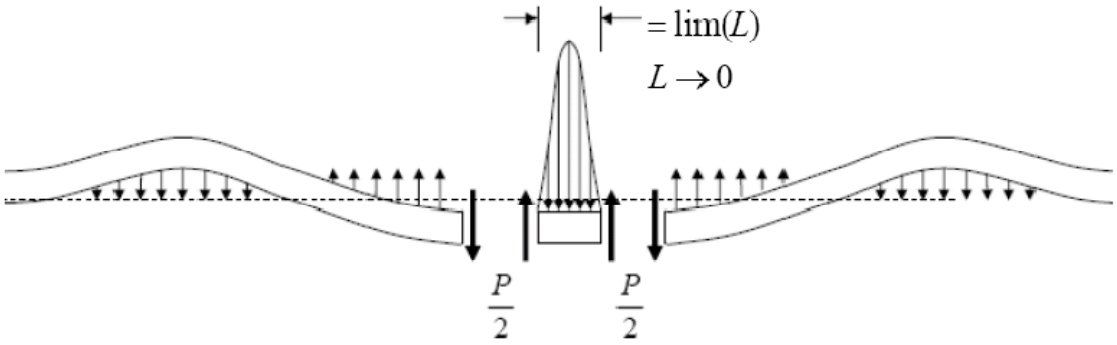

Figure 2-2: Boundary Conditions of the Rail

The above differential equation and boundary conditions can now be set up and solved in different ways to represent various track behaviors.

2.2 Beam on Elastic Foundation Model

The Beam on an Elastic Foundation (BOEF) model, proposed by Winkler (1867), describes a point load applied to an infinite beam on an infinite elastic foundation. It assumes the distributed supporting force of the track foundation is linearly proportional to

the vertical rail deflection (i.e. $p(x)=uw(x)$). Here, the coefficient u is defined as track modulus. The differential Equation 2-1 then becomes

$$EI\frac{d^4w(x)}{dx^4}+uw(x)=q(x) \qquad \text{Equation 2-4}$$

This model has been shown to be an effective method for determining track modulus (Raymond, 1985; Meyer, 2002) and derivations can be found in (Kerr, 1976; Boresi and Schmidt, 2003). The vertical deflection of the rail, w, as a function of longitudinal distance along the rail x (referenced from the position of the applied load) is given by:

$$w(x)=-\frac{P\beta}{2u}e^{-\beta|x|}[\cos(\beta|x|)+\sin(\beta|x|)] \qquad \text{Equation 2-5}$$

where:

$$\beta=\left(\frac{u}{4EI}\right)^{\frac{1}{4}} \qquad \text{Equation 2-6}$$

P is the load on the track

u is the track modulus

When multiple loads are applied, the rail deflections caused by each of the loads are superposed (assuming small vertical deflections) (Boresi and Schmidt, 2003).

A plot of the rail deflection given by the Winkler model over the length of a four-axle coal hopper is shown in Figure 2-3. The deflection is shown relative to the wheel/rail contact point for five different reasonable values of track modulus (6.89, 13.8, 20.7, 27.6, and 34.5 MPa corresponding to 1000, 2000, 3000, 4000, and 5000 psi

respectively). This example assumes 115 lb rail with an elastic modulus of 206.8 GPa (30,000,000 psi) and an area moment of inertia of 2704 cm^4 (64.97 in^4).

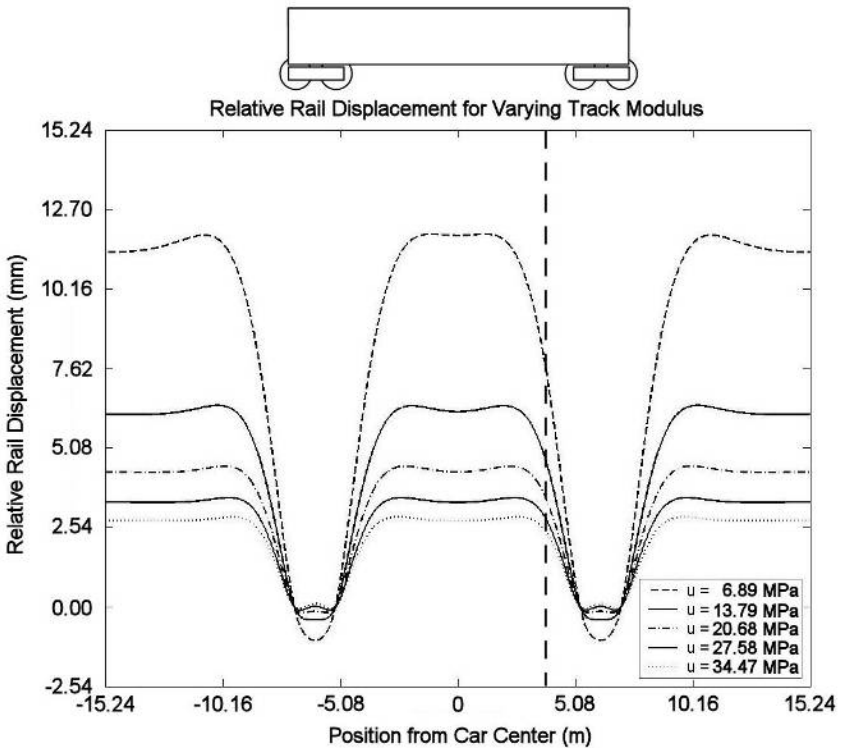

Figure 2-3: Relative Rail Displacement for Different Loads under a Railcar

The limitations of the Winkler model are clear given the widely accepted non-linearity of track structure. However, this model is often used because it does provide a clear closed-form solution to the relationship between load and deflection in track structure.

2.3 Nonlinear Cubic Model

Field tests conducted by the ASCE-AREA Special Committee on Stresses in Railroad Track (1918) clearly showed that the vertical rail deflections were not linearly

proportional to the wheel loads. An extensive experimental study conducted by Zarembski and Choros (1980) also clearly documented this nonlinear response.

Figure 2-4 shows the experimental results of the track responses under various applied loads. Rail deflection was measured at given locations using linear variable differential transformers (LVDTs) as a short, slow moving train of known weight passed. The axles of the train carried 150,600 N (33850 lbf), 60,230 N (13540 lbf), and 30650 N (6890 lbf). The LVDTs were mounted to steel rods (about 1m (3ft)) driven into the subgrade to provide a stable reference. The LVDTs then measured the vertical motion of the flange relative to the steel rod. The results from four LVDTs are shown in Figure 2-4. Here the LVDTs were placed at 1m (3ft) increments along the track (x=1m, 2m, 3m, 4m).

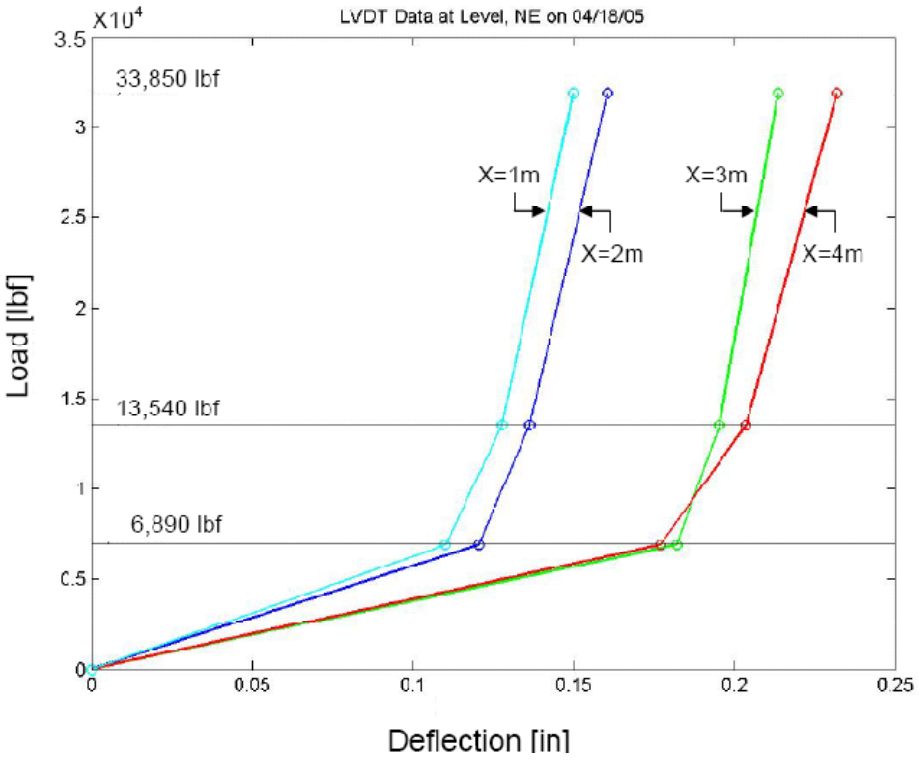

Figure 2-4: Deflection of Track under Three Loads

These measurements, along with many others dating back to the Talbot Report (ASCE-AREA Special Committee, 1918) clearly indicate that the vertical rail deflections are not linearly proportional to the wheel loads. It is also important to note that the "degree" of non-linearity can change dramatically over very short distances along the track. Note the deflection of the track under the 30650 N (6890 lbf) load increased about 60% over a distance of one meter. This non-linearity and variability greatly complicates determining and modeling track structure. Several methods have been developed for calculating modulus with each method assuming a different definition of track modulus that approximates the non-linear behavior of real track.

Here, a new model is proposed that represents the relationship between vertical rail deflection and the distributed rail support force as a cubic polynomial. To define this relationship the experimental results of (Zarembski and Choros, 1980) are plotted in Figure 2-5 along with a cubic polynomial curve fit. The polynomial fits the experimental results very well (R^2=0.9987).

Using a cubic polynomial has several advantages. First, it clearly captures the behavior of real track in that it provides for low stiffness at low loads and higher stiffness at higher loads. Also, negative displacement of the track (track lift) does not result in significant downward forces being applied to the rail. Unlike the previous models, the cubic polynomial closely represents the fact that if the track rises slightly, the ballast does not pull the track down.

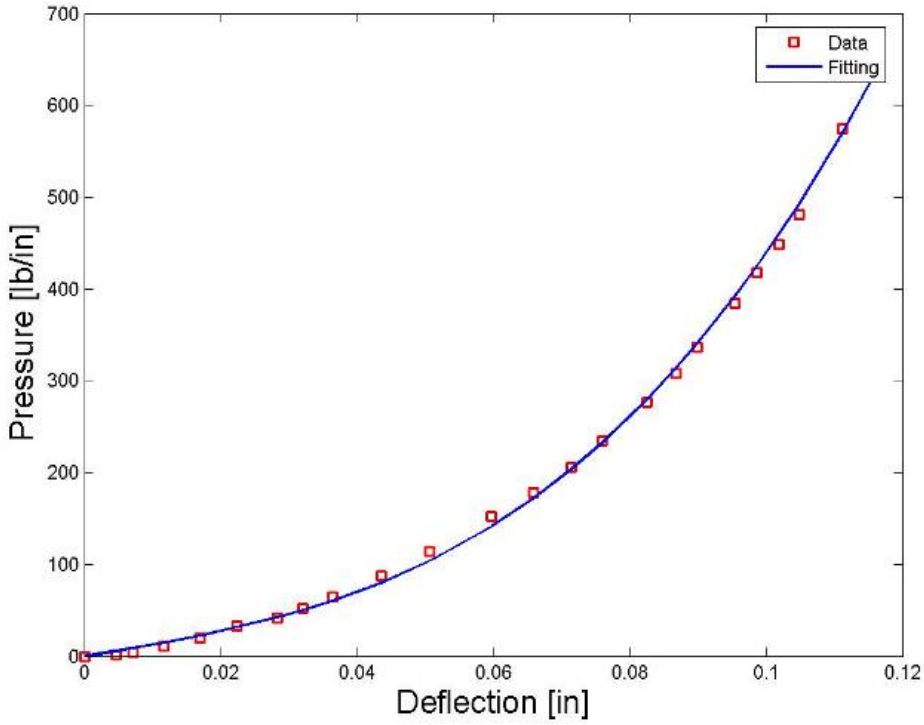

Figure 2-5: Experimental Data (Zarembski and Choros, 1980) and Curve Fitting

Here, the supporting distributed load *p(x)* has a cubic relationship between *p(x)* and *w(x)*:

$$p(x) = u_1 w(x) + u_3 w^3(x) \qquad \text{Equation 2-7}$$

Note that symmetry about the applied load requires the second order term to vanish. Substitution into the BOEF model gives the following differential equation:

$$EI\frac{d^4 w}{dx^4} + u_1 w + u_3 w^3 = q \qquad \text{Equation 2-8}$$

Equation 2-8 is a nonlinear differential equation, and a closed form analytical solution is not straightforward. One analytical approximation based on Cunningham's

method can be found in McVey (2006). However, a numerical solution for this boundary value problem (BVP) can be obtained.

The BVP can be written in state space notation as:

$$\underline{w'} = \frac{\partial}{\partial x}\begin{bmatrix} w(x) \\ w'(x) \\ w''(x) \\ w'''(x) \end{bmatrix} = func(\underline{w}, x) \qquad \text{Equation 2-9}$$

Given Equation 2-9 the BVP becomes:

$$\frac{\partial}{\partial x}\begin{bmatrix} w(x) \\ w'(x) \\ w''(x) \\ w'''(x) \end{bmatrix} = \begin{bmatrix} w'(x) \\ w''(x) \\ w'''(x) \\ -\frac{1}{EI}\left(u_1 w(x) + u_3 w^3(x)\right) \end{bmatrix} \qquad \text{Equation 2-10}$$

As the name implies, the fourth order BVP described above requires the values of four boundary conditions which are displayed in the following equations:

$$\begin{aligned} w(x)|_{x=\infty} &= 0 \\ w(x)|_{x=-\infty} &= 0 \\ w'(x)|_{x=0} &= 0 \\ w(x)|_{x=0} &= w_o \end{aligned} \qquad \text{Equation 2-11}$$

Now, since the BVP can have more than one correct solution, an initial "guess" for the last boundary condition is needed in order for the solution to converge to an expected solution. In this case, the initial guess is provided by the Winkler model evaluated at $x=0$ and $u=u_3$.

$$w(0) = w_o = -\frac{P\beta}{2u_3} \quad \text{where}: \beta = \left(\frac{u_3}{4EI}\right)^{\frac{1}{4}} \qquad \text{Equation 2-12}$$

The mechanics of this problem also require that the solution be found subject to the additional constraint given by the free body diagram in Figure 2:

$$\int_0^\infty \left(u_1 w + u_3 w^3\right) dx = \frac{P}{2} \qquad \text{Equation 2-13}$$

The unique solution that satisfies each of these constraints will give the rail deflection. Many numerical techniques can be used to solve this well-posed BVP. In this work the "bvp4c" function in Matlab (Kierzenka J. and Shampine L. F., 2001) was used.

While the cubic model closely represents the deflection test data over the entire range of wheel loads, the accuracy of the linear analysis depends on the magnitude of the test load.

Since the cubic spring is initially softer than the one in the Winkler model, the rail must deflect more before the base can pick up the full load. This means that the distributed load will be spread over a wider span than for the linear model as shown in Figure 2-6. Meanwhile, the deflection at the contact point for the cubic model is slightly larger than the one for the Winkler model when the applied load is relatively large.

Although the cubic model represent the real track response more accurately, it is not easy to apply. In other words, for a given load and known maximum deflection, it is not possible to depict the actual track response. However, modulus can be simply calculated from the applied load and maximum deflection using Winkler model.

Therefore, the application of cubic model is limited and the Winkler model is widely used in the industry.

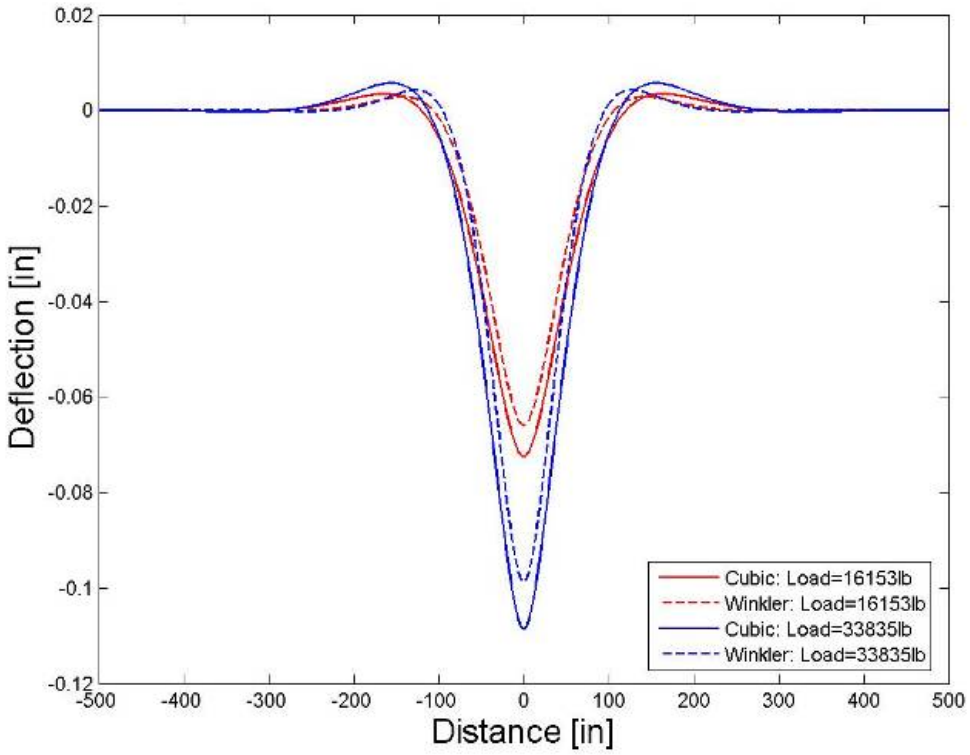

Figure 2-6: Comparison of Cubic and Winkler Models

2.4 Methods for Determining Track Modulus

Many methods and models have been developed and used to determine track modulus. The methods include the Beam on Elastic Foundation method, Deflection Basin method. In these methods, a static load must be applied to the rail, and rail deflection measurements must be made before and after the load is applied. Focused on the nonlinear cubic model, a new method is proposed to calculate modulus at characteristic load.

2.4.1 Beam On Elastic Foundation (BOEF) Method

The most straightforward method to estimate track modulus at a given track location is to simply measure the vertical deflection at the point of an applied known load, *P*. This produces the measurement of the track stiffness, *k*, which is the ratio between applied load and maximum deflection under the wheel, but this measurement can be related to track modulus, *u*, using the BOEF model and assuming that the relationship between rail supporting load *p(x)* and deflection *w(x)* is linear and elastic (i.e. *p(x)=uw(x)* as in Selig and Li, 1994; Cai et al, 1994). These assumptions lead to the Winkler model. The resulting track modulus is given by:

$$u = \frac{1}{4}\left(\frac{1}{E1}\right)^{\frac{1}{3}}\left(\frac{P}{w_0}\right)^{\frac{4}{3}} \qquad \text{Equation 2-14}$$

where: *u* is the track modulus

E is the modulus of elasticity of the rail

I is the moment of inertia of the rail

P is the load applied to the track

w_0 is the deflection of the rail at the loading point

This method only requires a single measurement and it has also been suggested to be the best method for field measurement of track modulus (Zarembski and Choros, 1980). However, as shown in Figure 2-4, it is clear that this linear approximation has large error for real track. Using a single applied load and a single measurement of deflection does not capture the changes in the load-deflection curve present in real track.

2.4.2 Deflection Basin Method

The Deflection Basin Method uses the vertical equilibrium of the loaded rail and several deflection measurements to estimate track modulus more directly. In this approach, rail deflection caused by point loads is measured at several (ideally infinite) locations along the rail and the entire deflected "area" calculated. The deflection basin for two applied loads is shown in Figure 2-7.

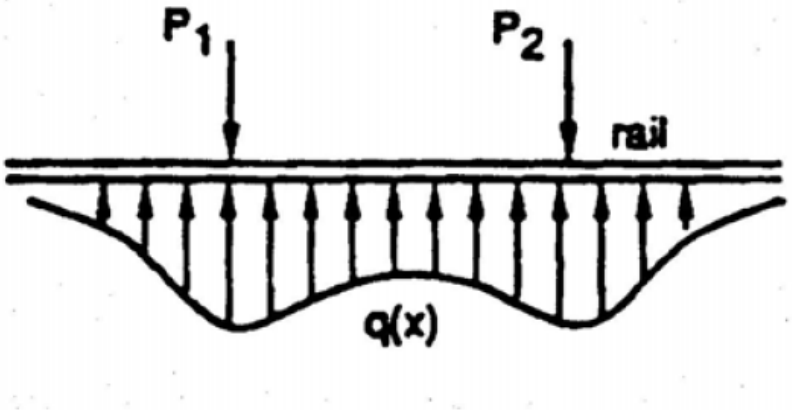

Figure 2-7: Deflection Basin (Selig and Li, 1994)

Using the concept of vertical equilibrium, the applied load can be shown to be proportional to the integral of the rail deflection or the deflection basin area (Selig and Li, 1994; Cai et al, 1994). For a single applied load, the equation is:

$$P=\int_{-\infty}^{\infty} q(x)dx=\int_{-\infty}^{\infty} uw(x)dx=uA_w \qquad \text{Equation 2-15}$$

where: P is the load on the track

$q(x)$ is the vertical supporting force per unit length

u is the track modulus

$w(x)$ is the vertical rail deflection

A_w is the deflection basin area

x is the longitudinal distance along the track

This method requires several deflection measurements over the section of track that supports the load(s), which makes it very time consuming (Selig and Li, 1994). When using this method, the non-linearity caused by slack in the rail should be removed by using a light load for the base measurements and a heavy load as deflected measurements. This method is not recommended because it is more time consuming and is based on some questionable assumptions (Kerr and Shenton, 1985).

2.4.3 Heavy-Light Load Method

Many have represented the load/defection curve as piece-wise linear with a low stiffness at low loads and a much higher stiffness at higher loads (Kerr and Shenton, 1986). This is seen in real track as slack in the rail and can be caused by many things such as the ties not contacting the ballast. As the rail is loaded, a low stiffness is experienced until the tie contacts the ballast, resulting in a higher stiffness. This leads to a measurement of track stiffness using two loads as shown in Figure 2-8, that are ideally both in the high stiffness range (e.g. slack is removed) (Ebersohn and Selig, 1994; Read et al, 1994, Kerr, 2003).

The Equation 2-16 demonstrated how to calculate track stiffness by using the two different loads (seating load and full load). This calculated track stiffness can then be related to track modulus.

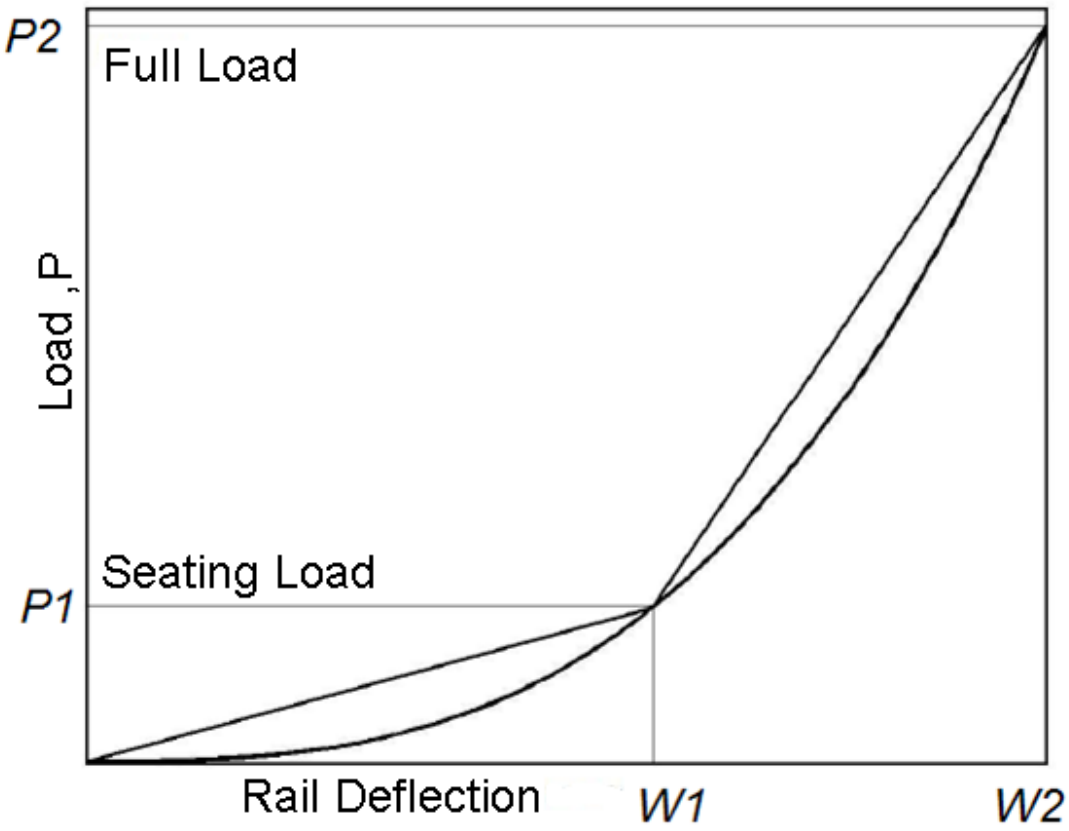

Figure 2-8: Piece-wise Linear Approximation for Track Load-Deflection Behavior

$$k = \frac{P_2 - P_1}{w_2 - w_1}$$ Equation 2-16

where: k is the track stiffness

P_i are the applied loads

w_i are the corresponding deflections

Again, a linear assumption is used to transform the stiffness measurements of the two loads to track modulus. The clear difficulty with this measurement is that the real load/deflection relationship is not piecewise linear and the resulting stiffness varies with

the selection of the two loads, P_1 and P_2. It is also clear that any two choices of loads will give a different value of track modulus.

2.4.4 Track Modulus at Characteristic Load

It is proposed that a good definition of track modulus is the variation in supporting distributed force relative to the variation in deflection near the characteristic load for a given track (Lu et al., 2008). This characteristic load might be defined as the nominal axle load for a given freight line (e.g. 160kN or 286,000/8=36kips). This can be expressed mathematically as the derivative of the pressure-deflection curve evaluated at the characteristic load P^*:

$$u^* = \left.\frac{\partial p}{\partial w}\right|_{P^*} \qquad \text{Equation 2-17}$$

where: u is the track modulus

p is the supporting force per unit length of rail

P^* is the characteristic load corresponding to a given rail line

To evaluate the derivative at the characteristic load, the load must again be transformed to a distributed load. This can be done with the linear assumptions as described previously (the Winkler model). This definition of track modulus has been used in field measurements (Arnold et al., 2006).

Finally, in the nonlinear cubic model described previously, the track modulus at characteristic load can be calculated as:

$$u^* = \left.\frac{\partial p}{\partial w}\right|_{P^*} = \left.\frac{\partial\left(u_1 w + u_3 w^3\right)}{\partial w}\right|_{P^*} = u_1 + 3u_3 w^2\Big|_{P^*} \qquad \text{Equation 2-18}$$

This definition of track modulus is compared to the Winkler model as shown in Figure 2-9. In this figure, the load-deflection curve is plotted from the experimental data of (Zarembski and Choros, 1980) shown in Figure 2-5.

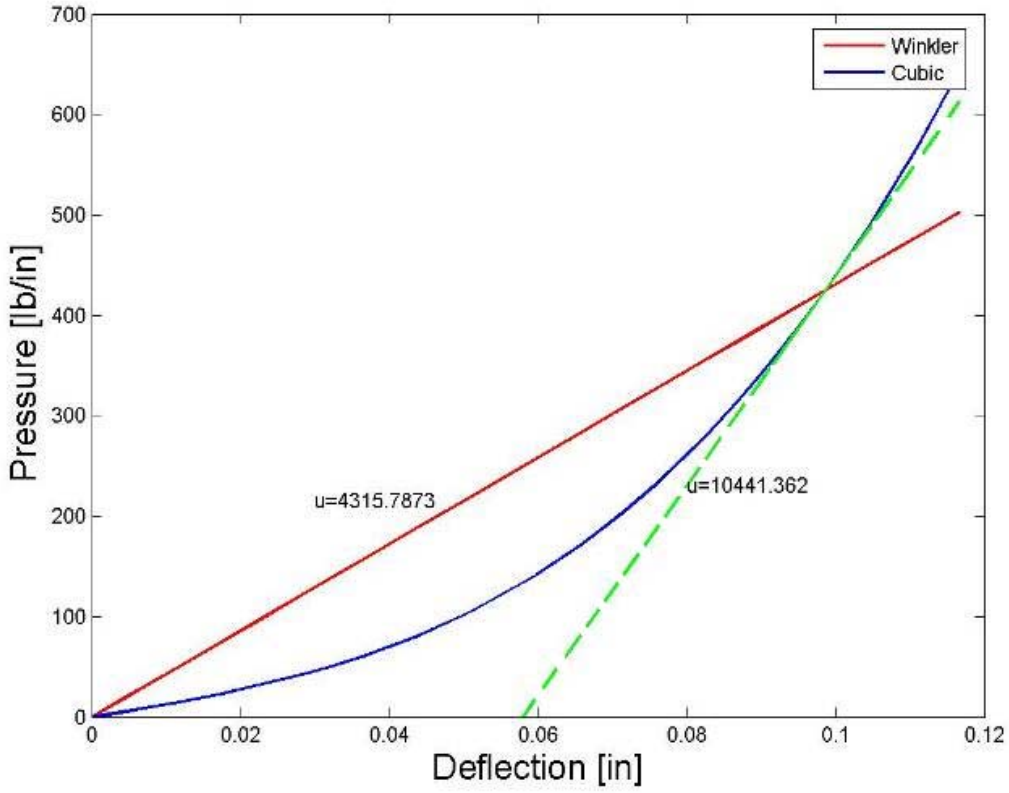

Figure 2-9: Modulus Calculations in Winkler and Cubic Model

It is clear that for single data points at higher loads the Winkler model will always underestimate the actual track modulus (Figure 2-9). The Winkler model will also poorly represent changes in deflection with respect to changes in load at these higher values.

2.5 Factors Influencing Track Modulus

Railroad track structure is demonstrated in Figure 2-10. Railroad track has several components that all contribute to track modulus, including the rail, subgrade, ballast, subballast, ties, and fasteners. The rail directly supports the train wheels and is supported on a tie pad and held in place with fasteners to ties. The crossties rest on a layer of rock ballast and subballast used to provide drainage. The soil below the subballast is the subgrade.

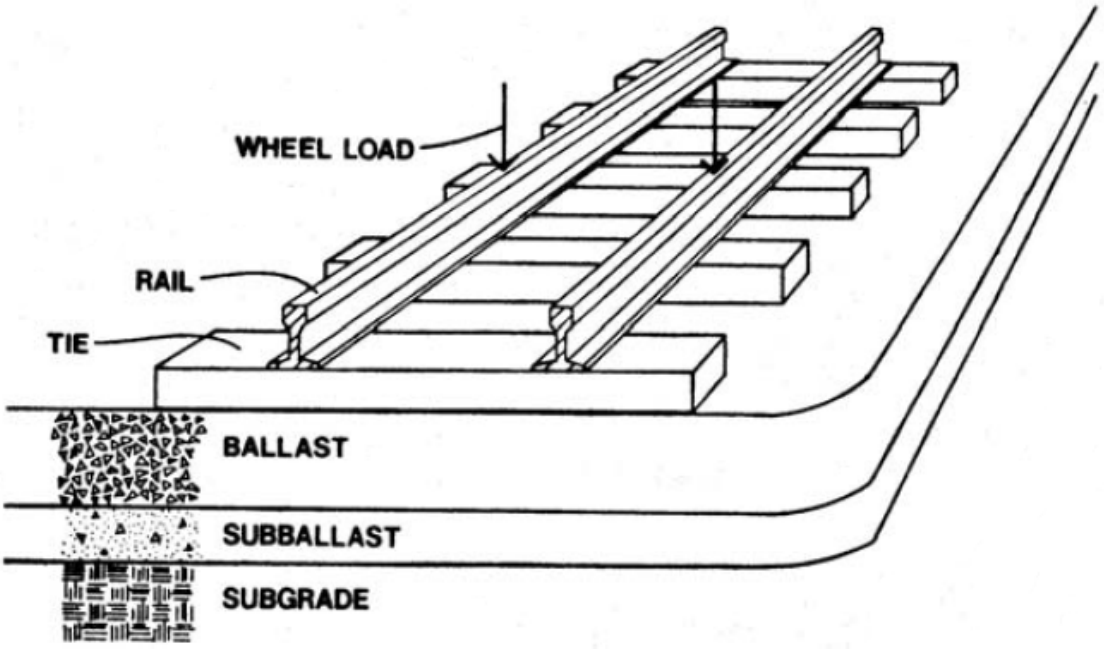

Figure 2-10: Track Structure (Chang et al. 1980)

The subgrade resilient modulus and subgrade thickness have the strongest influence on track modulus. These parameters depend upon the physical state of the soil, the stress state of the soil, and the soil type (Li and Selig, 1994; Selig and Li, 1994). Track modulus increases with increasing subgrade resilient modulus, and decreases with increasing subgrade layer thickness (Selig and Li, 1994). Ballast layer thickness and

fastener stiffness are the next most important factors (Selig and Li, 1994; Li and Selig, 1998). Increasing the thickness of the ballast layer and/or increasing fastener stiffness will increase track modulus (Stewart, 1985; Selig and Li, 1994). This effect is caused by the load being spread over a larger area. The system presented in this dissertation measures the net effective track modulus that includes all of these factors.

3 SYSTEM MODELING AND SIMULATION

In this chapter, the measurement principle and methodology will be described. Based on Winkler model, the relation between system's measurement and track modulus will be analyzed so that modulus can be estimated from the system's measurement. Simulations will show that track geometry variations will affect system's measurement. Therefore, a method is developed to eliminate this effect.

3.1 Measurement Principle and Methodology

The geometry of the measurement system is shown in Figure 3-1. An instrument beam rigidly mounted on the side frame of the hopper car extends a few feet away from the wheels. A sensor head which includes a laser/camera system is attached to the end of the beam. The sensor system has two line lasers and a camera as shown in Figure 3-2. The line lasers intersect the rail surface at an acute angle to create curves across the surface of the rail. Using line lasers allows the system to compensate for lateral movement of the rail relative to the camera and for changes in rail profile. The camera captures images showing two curved laser lines on the rail surface and the distance between the lines d is obtained by an image processing program. This distance d is then converted to the distance between the beam and the rail surface under the camera h. A track model is then used to calculate the track modulus.

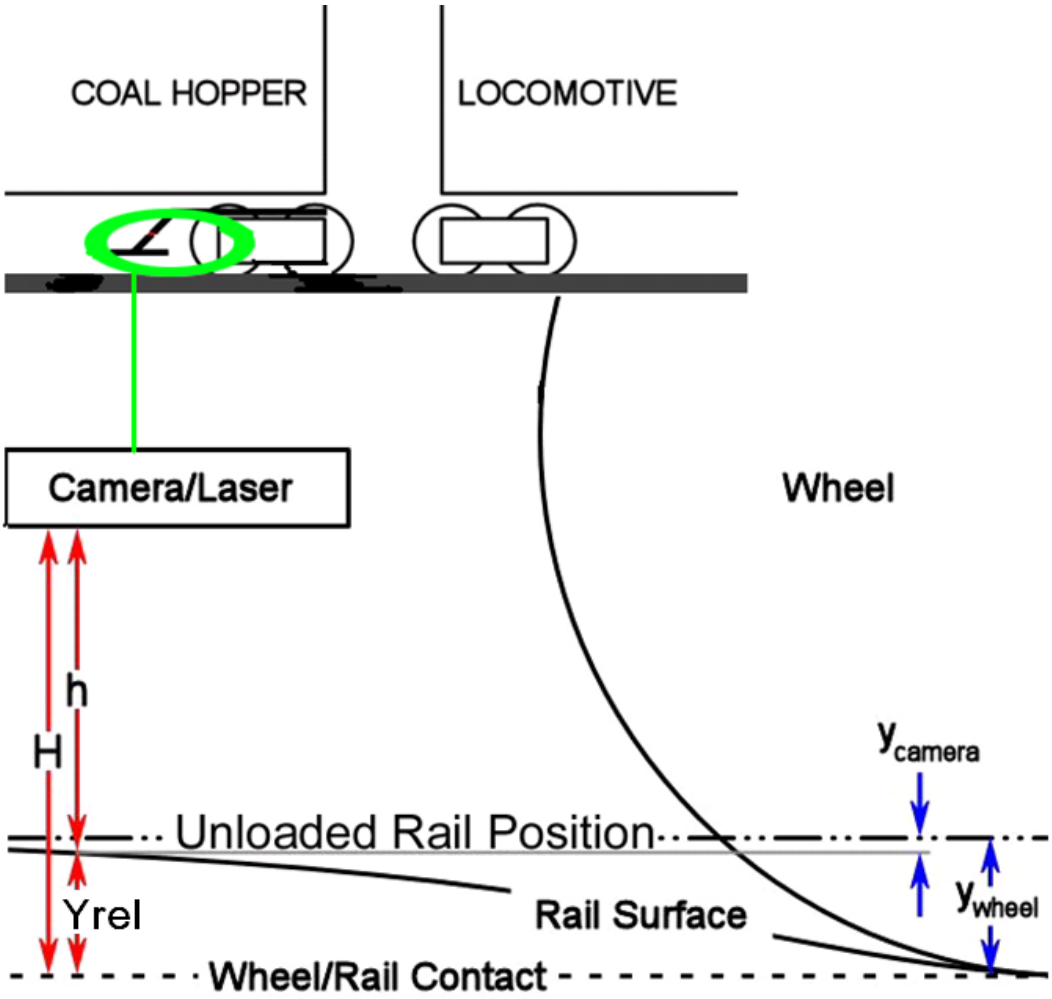

Figure 3-1: Diagram of Measurement Principle

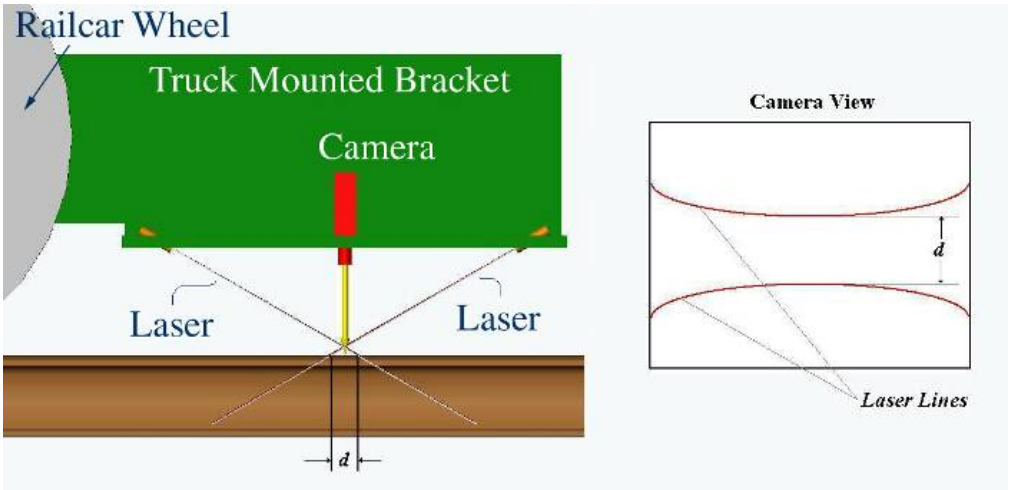

Figure 3-2: Camera/Laser System

Figure 3-1 illustrates that the fixed distance between the wheel/rail contact point and the sensor, *H*, relates the relative rail displacement, *Yrel*, to the measured height of the sensor above the rail surface, *h*. Here y_{camera} is the deflection of the rail at the location underneath the camera/lasers and y_{wheel} is the deflection of the rail at the wheel/rail contact point. The deflections are negative in value because the positive axis is defined upwards.

The sensor system measures the distance between the camera image plane and the rail surface, *h*. Then, the displacement of the rail surface with respect to the wheel/rail contact plane, *Yrel* (Figure 3-1) can be found. The displacement, *Yrel*, can then be related to the absolute rail deflection of the wheel/rail contact point (with respect to the unloaded rail), y_{wheel} (Figure 3-1) by using the Winkler model or the Cubic model.

The mathematical model relates the measured distance between the laser lines to the track modulus. The rail deflection measured by the sensor is dependent on the four wheel loads. The sensor will measure the relative rail displacement between the rail and wheel/rail contact point. This measurement can be made if it is assumed that the instrument beam, truck, and wheels are rigid. With this assumption, the distance between the sensor system and wheel/rail contact point can be assumed constant (*H* is constant). This is a reasonable assumption as the instrument beam, side frame, and wheels are all massive, nearly rigid elements and these elements do not include the suspension of the railcar. Rotation of the side frame could cause this distance (*H*) to change, but this rotation has been experimentally shown to be insignificant (Norman, 2004).

The sensor reading, which is the measured distance between the lasers, is geometrically related to the height of the sensor above the rail. The sensor in effect measures its height above the rail by measuring the distance between the lasers. As the sensor moves closer or farther from the rail surface, the distance between the lasers changes. A schematic of the sensor is shown in Figure 3-3.

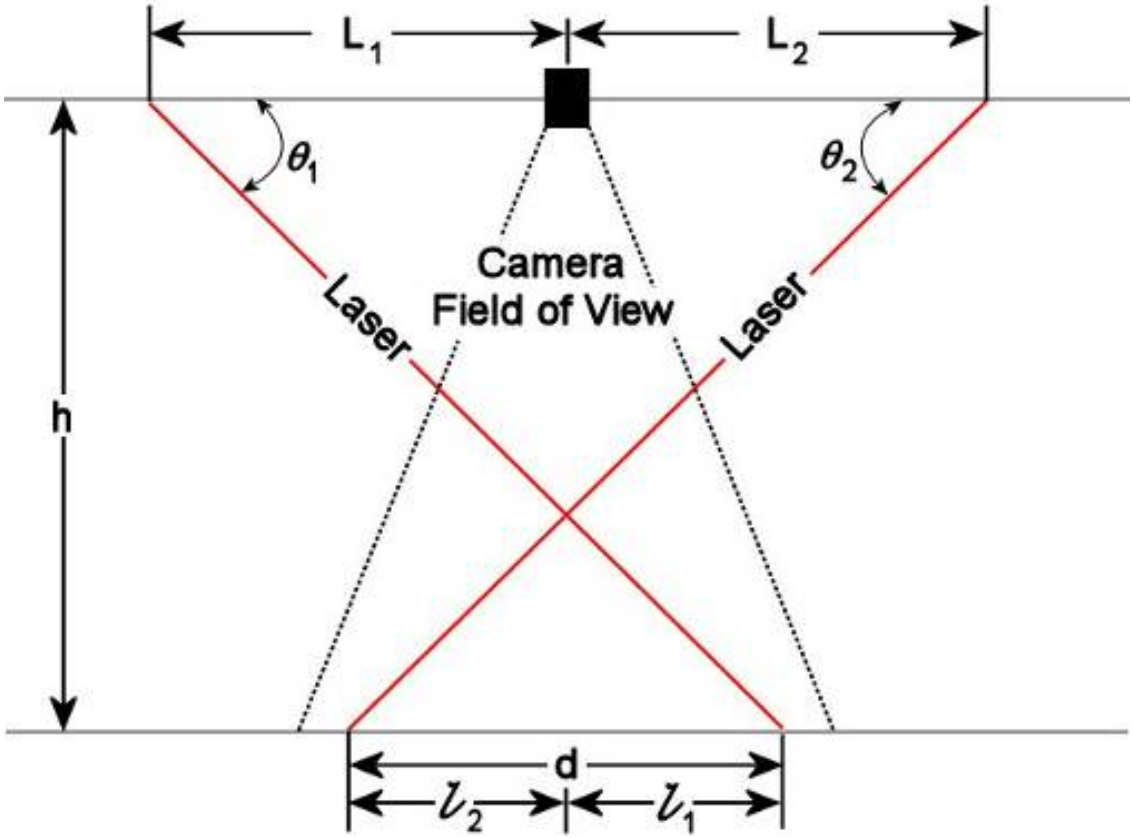

Figure 3-3: Sensor (Lasers and Camera) Geometry

From the above figure, the following equations can be written:

$$(L_1 + l_1)\tan\theta_1 = h \qquad \text{Equation 3-1}$$

$$(L_2 + l_2)\tan\theta_2 = h \qquad \text{Equation 3-2}$$

$$d = l_1 + l_2 \qquad \text{Equation 3-3}$$

where L_1 and L_2 are the horizontal displacement of the lasers from the camera, θ_1 and θ_2 are the angles between the lasers and the horizontal, l_1 and l_2 are the horizontal distance between the center of the camera and laser/rail intersection, h is the vertical distance between the camera/lasers and the surface of the rail, and d is the distance between the lasers on the rail surface. Solving these equations results in:

$$d = \frac{h}{\tan\theta_1} + \frac{h}{\tan\theta_2} - (L_1 + L_2) \qquad \text{Equation 3-4}$$

Combining Equation 3-1 to Equation 3-4, a sensor reading can be calculated for a value of track relative deflection.

Combining this information with the track model (e.g. Winkler model) the sensor reading d can be related to the track modulus u. On softer track the rail will rise relative to the wheel/rail contact point and the laser lines as observed by the camera will move closer together. Conversely, the distance between the lasers will be large for stiffer track.

3.2 The Relation between Yrel and Modulus (Winkler Model)

Figure 3-4 shows the rail deflection from multiple loaded axles.

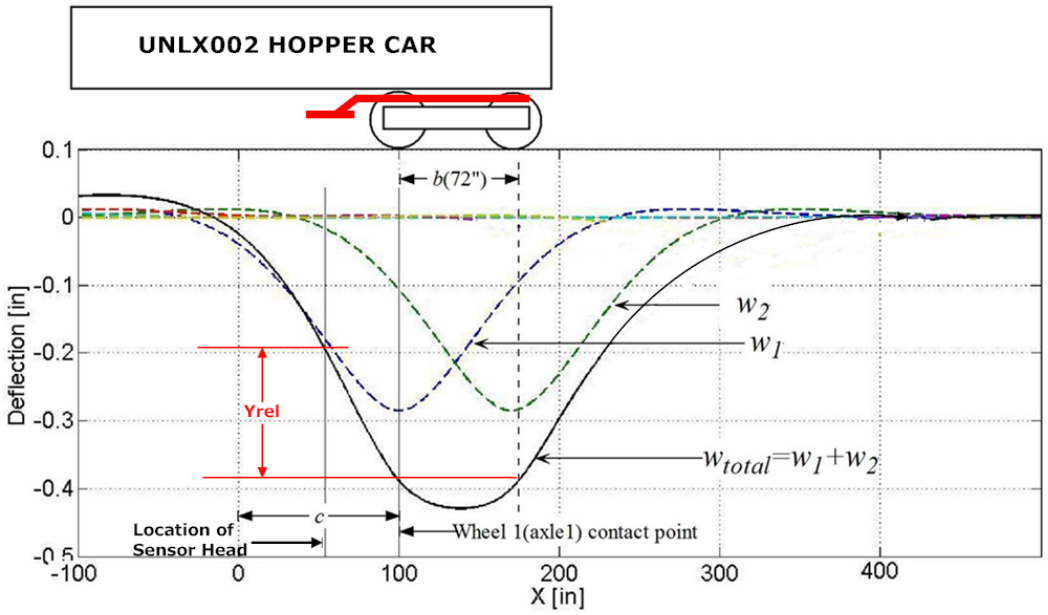

Figure 3-4: Superposition of the Deflections from Two Loads

In Figure 3-4, assuming the loads of wheel one (the left one) and wheel two (the right one) are the same (P), w_1 is the deflection of the rail attributed to wheel one and w_2 is the deflection of the rail attributed to wheel two. The total rail deflection is the superposition of w_1 and w_2.

From the Winkler model,

$$w_1(x) = -\frac{P\beta_1}{2u(c)} e^{-\beta_1|x-c|}\left[\cos\left(\beta_1|x-c|\right)+\sin\left(\beta_1|x-c|\right)\right] \qquad \text{Equation 3-5}$$

where:

$$\beta_1 = \left(\frac{u(c)}{4EI}\right)^{\frac{1}{4}}$$

E is the modulus of elasticity of the rail.

I is the moment of inertia of the rail.

x is the longitudinal distance along the rail.

c is the position of wheel one in the x coordinate (see Figure 3-4).

and $$w_2(x) = -\frac{P\beta_2}{2u(c+b)} e^{-\beta_2 \cdot |x-c-b|} \left[\cos\left(\beta_2 |x-c-b|\right) + \sin\left(\beta_2 |x-c-b|\right)\right]$$ Equation 3-6

where: $$\beta_2 = \left(\frac{u(c+b)}{4EI}\right)^{\frac{1}{4}}$$

b is the distance between the two wheel axles (72”).

(c+b) indicates the position of wheel two in the x coordinate frame.

The total deflection of the rail is the superposition of the two expressions:

$$w_{total}(x) = w_1(x) + w_2(x)$$

Then the total deflection at the wheel-rail contact point of wheel one is:

$$w_{total}(x)\big|_{x=c} = w_1(c) + w_2(c) = -\frac{P\beta_1}{2u(c)} - \frac{P\beta_2}{2u(c+b)} e^{-\beta_2 \cdot b}\left[\cos(\beta_2 b) + \sin(\beta_2 b)\right]$$ Equation 3-7

and the deflection of the rail under the sensor head which is four feet away from wheel one is:

$$w_{camera}(x)\big|_{x=c-a} = w_1(c-a) + w_2(c-a)$$
$$= -\frac{P\beta_1}{2u(c)} e^{-\beta_2 \cdot a}\left[\cos(\beta_2 a) + \sin(\beta_2 a)\right] - \frac{P\beta_2}{2u(c+b)} e^{-\beta_2 \cdot (a+b)}\left[\cos(\beta_2 (a+b)) + \sin(\beta_2 (a+b))\right]$$

Equation 3-8

Then,

$$Yrel = w_{total}(c) - w_{camera}(c-a)$$

Assuming the track is absolutely uniform (i.e., u is a constant), then

$$\beta_1 = \beta_2 = \beta = \left(\frac{u}{4EI}\right)^{\frac{1}{4}} \qquad \text{Equation 3-9}$$

Therefore,

$$\begin{aligned} Yrel &= w_{total}(c) - w_{camera}(c-a) \\ &= -\frac{P\beta}{2u}\{1 + e^{-\beta\cdot b}\left[\cos(\beta b) + \sin(\beta b)\right] \\ &\quad - e^{-\beta\cdot a}\left[\cos(\beta a) + \sin(\beta a)\right] - e^{-\beta\cdot(a+b)}\left[\cos(\beta(a+b)) + \sin(\beta(a+b))\right]\} \end{aligned} \qquad \text{Equation 3-10}$$

The result of Equation 3-10 is shown in Figure 3-5 where modulus is plotted as a function of Yrel using a look-up table. In this model, 132 RE rail was chosen (I=87.9 in^4); E is set to be 30,000,000 psi; the load on each wheel is 32500 lb; and the distance between the two axles is six feet. The typical values of modulus for various main-line track conditions (Kerr, 2003) are listed in Table 3-1 along with the corresponding Yrel value.

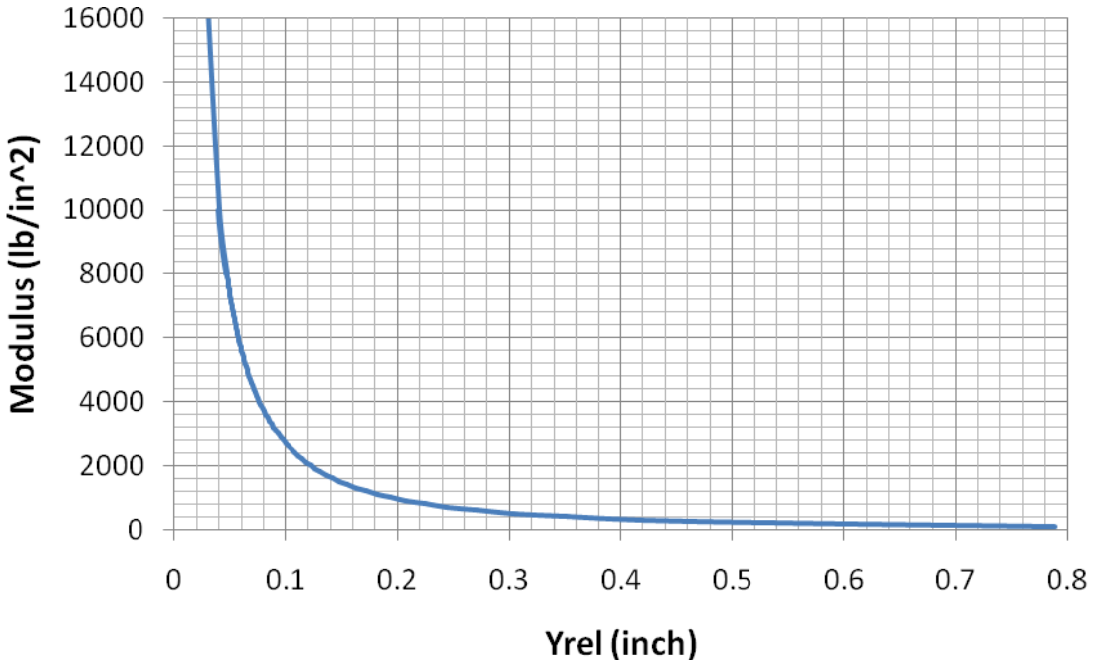

Figure 3-5: Relation between Yrel and Modulus (Winkler model)

Table 3-1: Modulus and Yrel for typical track conditions

Track Condition Description	Modulus (psi)	Yrel (inch)
Wood-tie track, after tamping	1000	0.2
Wood-tie track, compacted by traffic	3000	0.095
Concrete-tie track, compacted by traffic	6000	0.058
Wood-tie track, frozen ballast and subgrade	9000	0.044

The relation between the rail deflections at the wheel-rail contact point and relative deflection (Yrel) is shown in Figure 3-6. This non-linear relation is based on the Winkler model and superposition. For relatively small deflections (0~0.2 inch), Yrel is about 60% of the total deflection (deflection at the wheel-Rail contact point).

Figure 3-6: Relation between the Total Deflection and Yrel (Winkler model)

3.3 Effects of Track Geometry

The measurement of relative deflection (Yrel) uses the wheel/rail contact line as a reference as shown in Figure 3-1. The measurement assumes the unloaded rail is perfectly straight. However, if the rail has a significant pre-existing geometry variation over a length comparable to the four feet between the measurement point and wheel/rail contact point, the system's measurement will be affected. Large vertical "dips" that occur over a short length of track affect the measurement result.

The relationship between modulus and geometry is complex. In real track, areas of geometry variations often correlate with areas of modulus variations and vice versa.

A case study was chosen to investigate this relationship. Figure 3-7 shows a section of track where there is a significant geometry variation and a significant modulus variation. Measurements at the site indicated that the unloaded rail drops by 0.5" over a length of about 200". A geometry variation of this shape is significant and easily visible. The light colored ballast seen at this site also suggests tie "pumping" and low track stiffness.

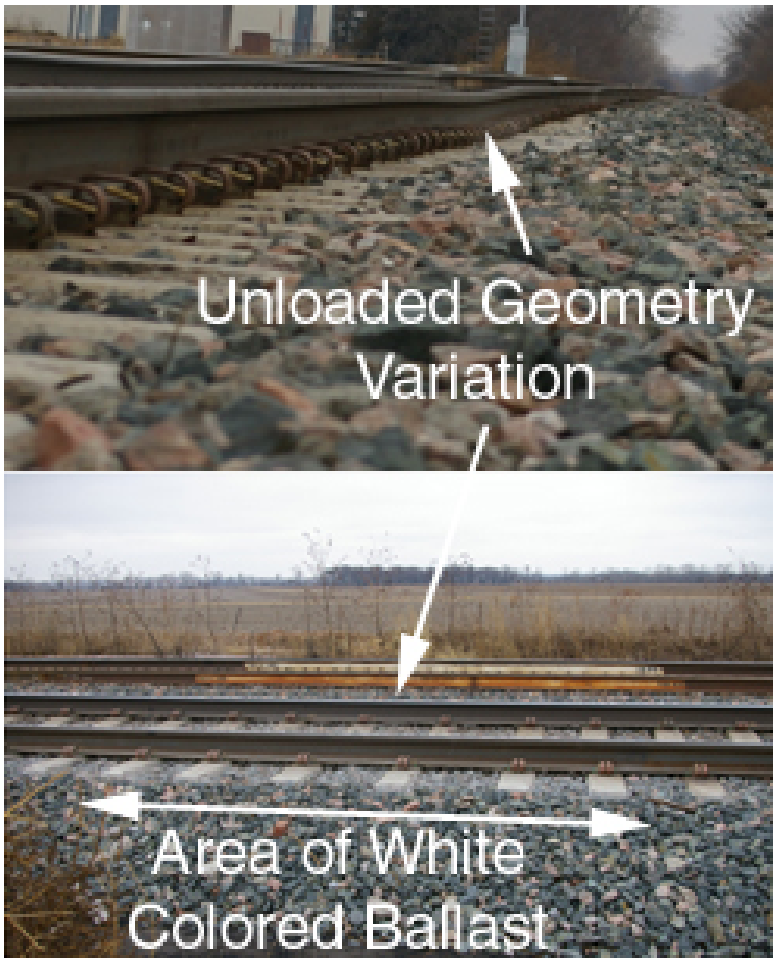

Figure 3-7: An Example Site with Both Significant Unloaded Geometry and Low Track Stiffness

Relative rail deflection (Yrel) from the measurement system at this site is 1.1". Simulations, based on the Winkler model, have been conducted to quantify the effects of track geometry on the measurement of relative deflection.

Figure 3-8 shows an example simulation result. In this simulation, a section of track has both geometry and modulus variations. The unloaded track geometry is described in the top subplot in Figure 3-8. It has a maximum "dip" of 0.5" in depth and it occurs over 200" (between 100" and 300") of track.

In the simulation it was assumed that the modulus over this section of track varies as a cubic curve with a minimum at the center of the geometry variation, (the middle subplot in Figure 3-8). The bottom subplot in Figure 3-8 shows the Yrel measurement for this site. Here, the "total" measurement replicates the value of 1.1" as it did in the real measurement when the measurement system passed over the location shown in Figure 3-7. To create this value it was found that the modulus for this location had to drop from 3000 psi (assumed as a reasonable value for "normal" track) to 800 psi in addition to the unloaded geometry profile. This measurement is then broken into two "elements" – a modulus element and a geometry element. The geometry element is the measurement that would be made if the same unloaded geometry (top subplot) existed on a perfectly rigid track. The modulus element in the remaining portion is the total measurement minus the geometry element.

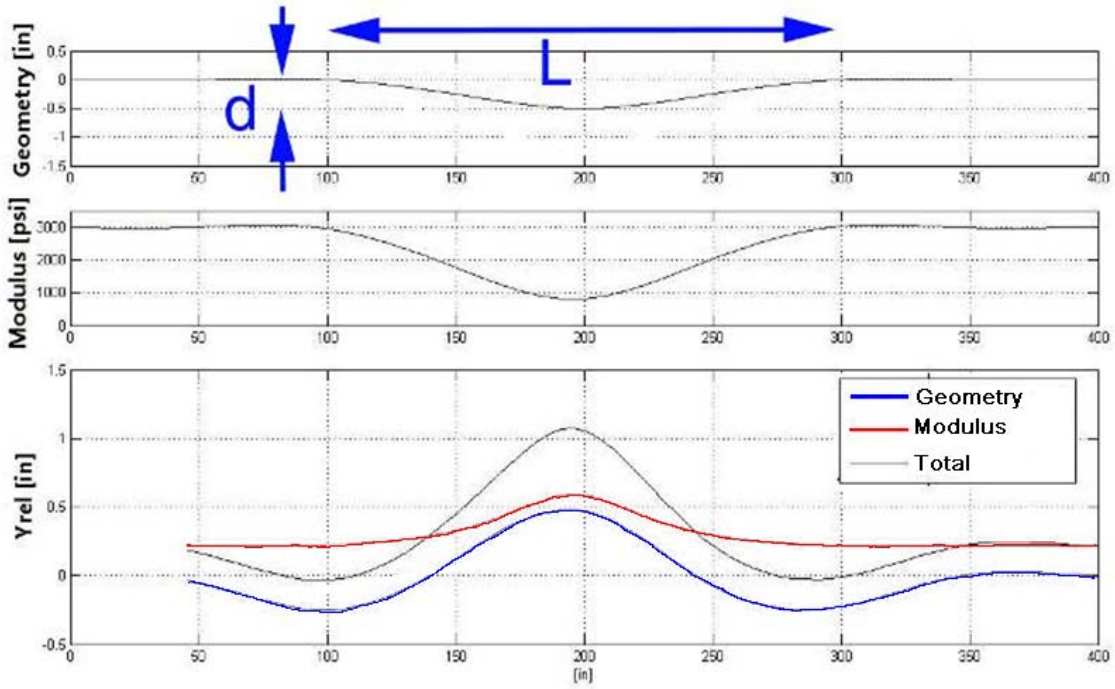

Figure 3-8: Simulation on the Effects of Track Geometry

It can be seen that in this case the contribution of geometry (the geometry element) is about equal to the contribution of modulus (the modulus element). However, both are required to make the measurement large.

Now, the simulation can be used to study the relative contribution of geometry and modulus as the length of the geometry variation (L) and the depth of the geometry (d) vary. The simulation result is shown in Figure 3-9.

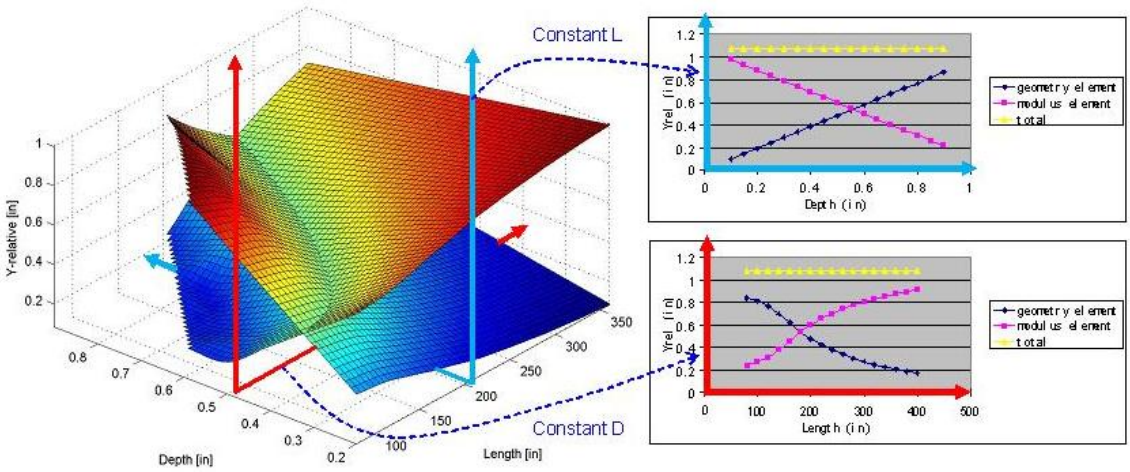

Figure 3-9: Effects of Unloaded Geometry of Various Length (L) and Depth (d)

It can be seen in Figure 3-9 that there is a complex relationship between modulus and geometry and that the effects vary depending on the length (L) and depth (d) of the geometry variation. The three-dimensional plot on the left shows the relative size of the geometry element and the modulus element. It can be seen that there is a curve where the elements are equal in magnitude.

The two graphs on the right show two cross sections of these surfaces. The top right graph shows the effects of variations in the length of the geometry defect (L) at a constant depth (d=0.5”). The bottom right graph shows the effects of variations in the depth of the geometry defect (d) at a constant length (L=200”).

Again, the conclusions that can be drawn from these simulations are that (1) only large vertical geometry defects occurring over a short distance significantly contribute to the Yrel measurement, and (2) both geometry and modulus problems are generally present to measure very large Yrel values.

3.4 Eliminating the Effects of Track Geometry Variation

As seen in the simulation and analysis in the previous section, track geometry can greatly affect the output of the system in terms of measuring rail deflection. In order to eliminate the effects of track geometry variation and get the real rail deflection results, rail profile data from track geometry measurement vehicles was introduced into the system.

A track geometry vehicle is a railed vehicle used for non-destructive diagnosis of railroad tracks. It measures various parameters including position, curvature, and alignment of the track, smoothness and the cross-level of the two rails, etc. The space curve channel of the geometry car uses multiple high-precision accelerometers onboard to produce the rail profile.

3.4.1 10-ft ECO (End-Chord Offset) Calculation from Rail Profile

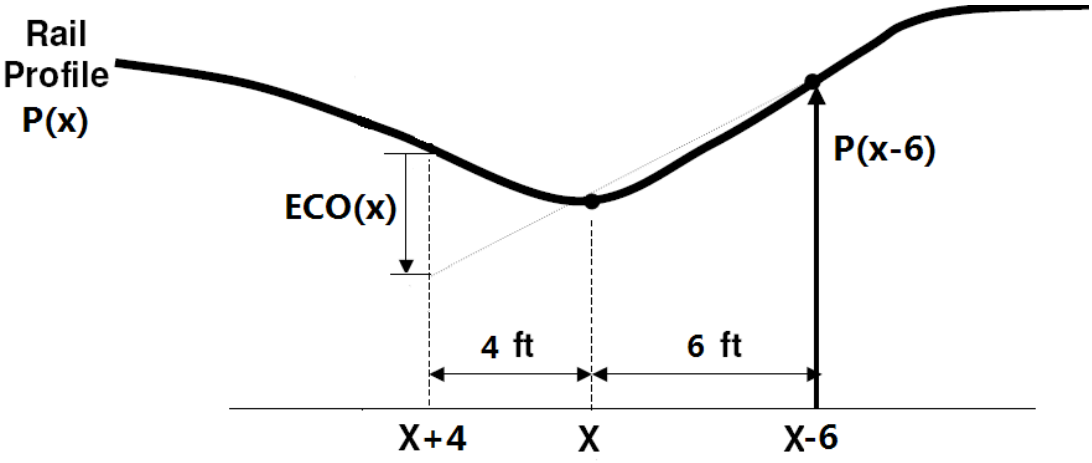

Figure 3-10: 10-ft ECO Calculation

As shown in Figure 3-10, *P(x)* is the rail profile from the space curve channel of the track geometry data. The longitudinal position of the track is defined as *x* (units of

foot). *ECO(x)* is the 10-ft end-chord offset when the leading wheel's longitudinal position is *x*. (*ECO* is positive if the string is above the rail.) Here, the 6 ft and 4 ft were chosen because they are the distance between the two wheel axles and the distance from the sensor head to the inboard wheel axle respectively.

From the geometry relation in Figure 3-10:

$$\frac{P(x-6)-P(x)}{P(x)-[P(x+4)+ECO(x)]}=\frac{6}{4} \qquad \text{Equation 3-11}$$

Therefore,

$$ECO(x)=\frac{2}{3}\cdot[P(x)-P(x-6)]+P(x)-P(x+4) \qquad \text{Equation 3-12}$$

3.4.2 Subtracting -ECO from Yrel

In Figure 3-11, *P(x)* is the vertical position of the inboard wheel-rail contact point when the inboard wheel's longitudinal position is *x*. *P(x-6)* is the vertical position of the inboard wheel-rail contact point when the inboard wheel's longitudinal position is *x-6*. If it is assumed the two wheels always have the same space curve, then *P(x-6)* is the vertical position of the trailing wheel-rail contact point when the inboard wheel's longitudinal position is *x*. *P4(x)* is the rail's vertical position four feet ahead of the inboard wheel when the inboard wheel's longitudinal position is *x*.

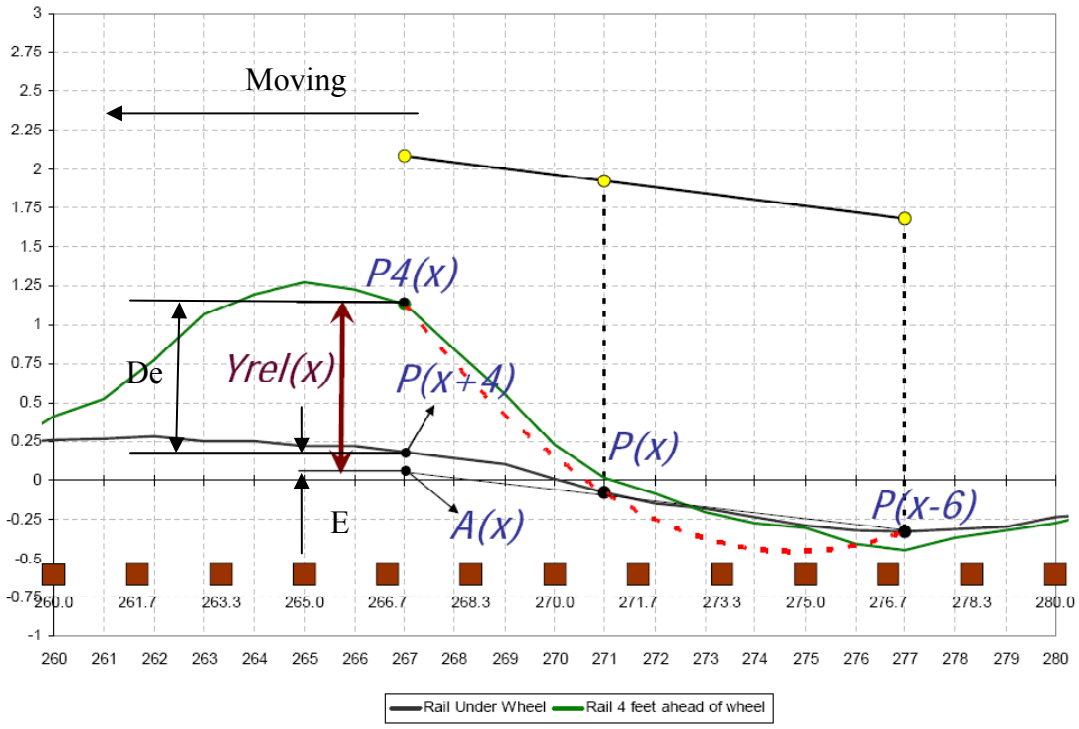

Figure 3-11: Deflection Calculation

Let *A(x)=P4(x)-Yrel(x)*, then from geometry relation in Figure 3-11, we have:

$$\frac{P(x-6)-P(x)}{P(x)-A(x)}=\frac{6}{4}$$

So,
$$A(x)=\frac{1}{3}\cdot[5P(x)-2P(x-6)] \qquad \text{Equation 3-13}$$

Therefore,
$$P4(x)=A(x)+Yrel(x)=\frac{1}{3}\cdot[5P(x)-2P(x-6)]+Yrel(x) \qquad \text{Equation 3-14}$$

The vertical position of the rail at location x+4 may be determined when the inboard axle is at location x. The vertical rail position at the same location may be determined again when the inboard axle is actually at location x+4. Then, the difference between these two measurements (*P4(x)-P(x+4)*) may be calculated by:

"Deflection" = P4(x)-P(x+4)

$$= \frac{1}{3} \cdot [5P(x) - 2P(x-6)] + Yrel(x) - P(x+4)$$

$$= \frac{2}{3} \cdot [P(x) - P(x-6)] + P(x) - P(x+4) + Yrel(x) \qquad \text{Equation 3-15}$$

$$= ECO(x) + Yrel(x)$$

It should be noted that the so-called "Deflection" calculated above is not the maximum deflection of the rail attributed to the loads. Rather, it is a relative deflection of the rail from partially loaded (when the axle is four feet away) to fully loaded (when the axle is right at the point).

Therefore, Yrel can be accounted for by two parts. One part is ECO, attributed to the track geometry variations, and the other part is the deflection related to track modulus variations.

3.5 Stress and Strain on the Rail

One potential output from the measurement system is that rail stress and strain can be estimated from system's measurement. Here, some primary studies are demonstrated trying to relate Yrel data to rail stress and strain.

The bending moment on the rail is calculated as:

$$M(x) = -EIw''(x) \qquad \text{Equation 3-16}$$

The axial stress in the rail is given by

$$\sigma_x(x,z) = \frac{M(x)z}{I} \qquad \text{Equation 3-17}$$

where z is the vertical distance from the neutral axis.

Therefore, the strain of the rail is

$$\varepsilon_x(x,z) = \frac{\sigma_x(x,z)}{E} = \frac{M(x)z}{EI} \qquad \text{Equation 3-18}$$

For two axles, superposition was applied to obtain the rail response from each load. The rail bending moment can be related to Yrel by using the same parameters shown in the model described in section 3.2, (E=30,000,000psi; I=87.9inch^4 for RE 132 rail; 32500 lb load on each axle) and by combining Equation 3-10, Equation 3-16 and Equation 3-18. This analysis is based on the Winkler model with the assumption that the track has no geometry variation.

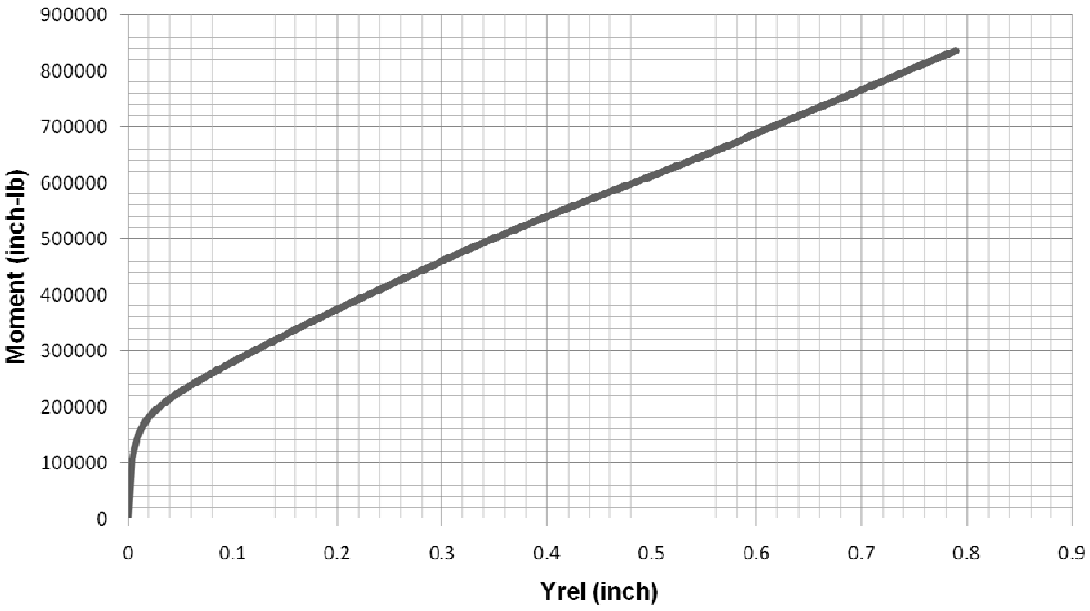

Figure 3-12: Relation between Rail Bending Moment and Yrel

The relations between Yrel and rail strain and between Yrel and rail stress are plotted in Figure 3-13 and Figure 3-14 respectively.

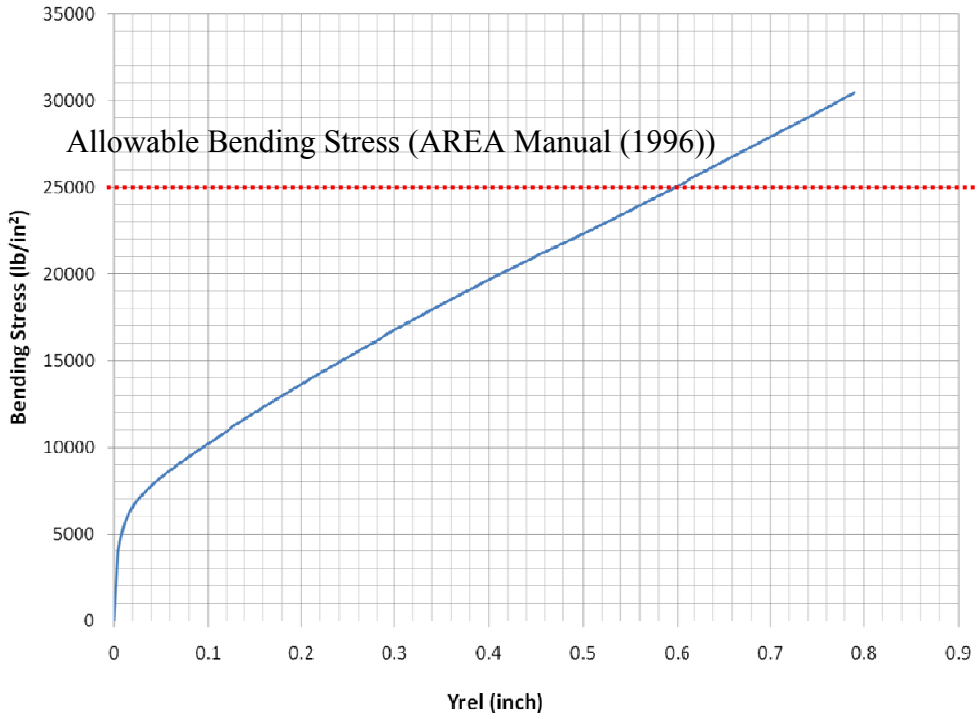

Figure 3-13: Relation between Rail Bending Stress (RE132, bottom) and Yrel

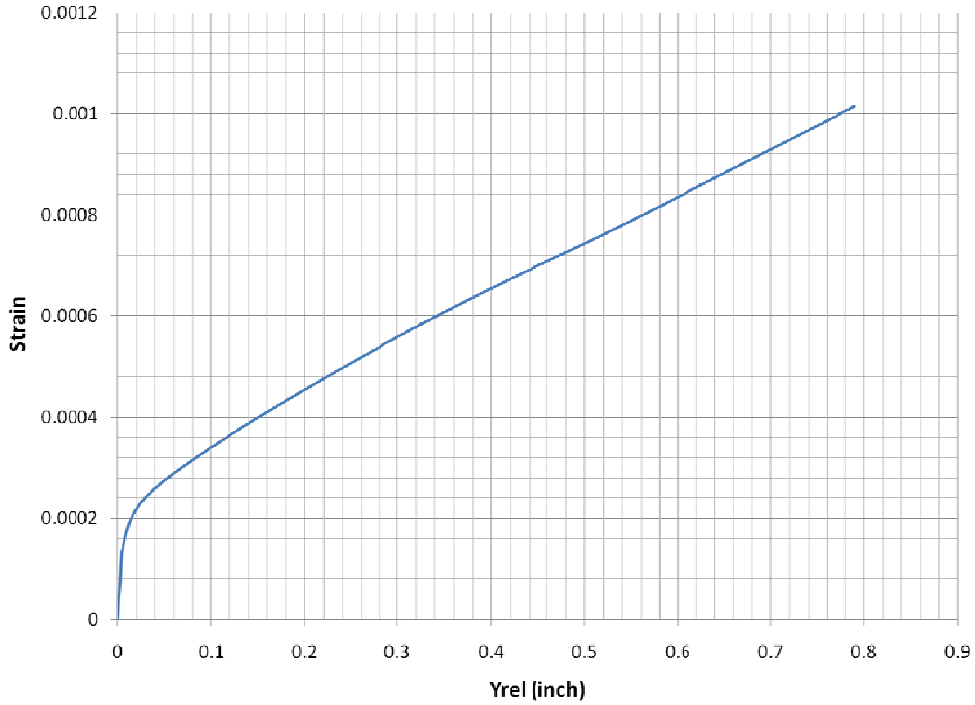

Figure 3-14: Relation between Rail Strain (RE132, bottom) and Yrel

According to the AREA Manual (1996, Chapter 16, 10.2.2,5), the allowable bending stress for a rail is determined as follows:

$$\sigma = \frac{\overbrace{70{,}000}^{\sigma_y} - \overbrace{20{,}000}^{\sigma_N}}{\underbrace{1.2}_{Lateral\_Rail\_Bending} \times \underbrace{1.25}_{Track\_Condition} \times \underbrace{1.15}_{Rail\_Wear\&Corrosion} \times \underbrace{1.15}_{Unbalanced\_elevation}} = 25{,}000 lb/in^2$$

where σ_y is the yield stress.

The denominator consists of four reduction coefficients. Note that the inclusion of the lateral rail bending coefficient avoids the need for a more involved bending-torsion rail analysis with an uncertain force input. The use of the rail wear and corrosion coefficient simplifies the analysis by allowing the use of the moment of inertia of a new rail. The subtraction of the axial thermal stress from σ_y leads to another simplification of the analysis.

Therefore, when Yrel is larger than 0.6", the stress at the bottom of the rail will exceed the allowable bending stress. However, it should be noted that Figure 3-13 is based on the Winkler model and simple superposition which are not very suitable for analyzing large deflection situations. In addition, Yrel measurements are usually combined with geometry effects, and the complexity of the track (joints, switches, bridges, etc.) will also contribute to large values of Yrel. All these complex factors were not considered in the analysis in Figure 3-13, so it will be difficult to evaluate stresses on the rail just based on Yrel measurements, especially when large deflections occur.

3.6 Different Loads

From Equation 2-5, it can be observed that rail deflections are linearly proportional to the applied loads given a constant track modulus. Based on the Winkler model and superposition, the relations between Yrel and modulus under various loads are illustrated in Figure 3-5. The values of load shown here are the loads on each axle. Two axles as in Figure 3-4 were taken into consideration in this model. This figure shows that given a certain modulus, the Yrel measurements increase linearly as the loads increase. Therefore, the weight of the measurement vehicle is a major factor to be considered when designing the measurement system. Clearly, heavier weights will generate larger deflections.

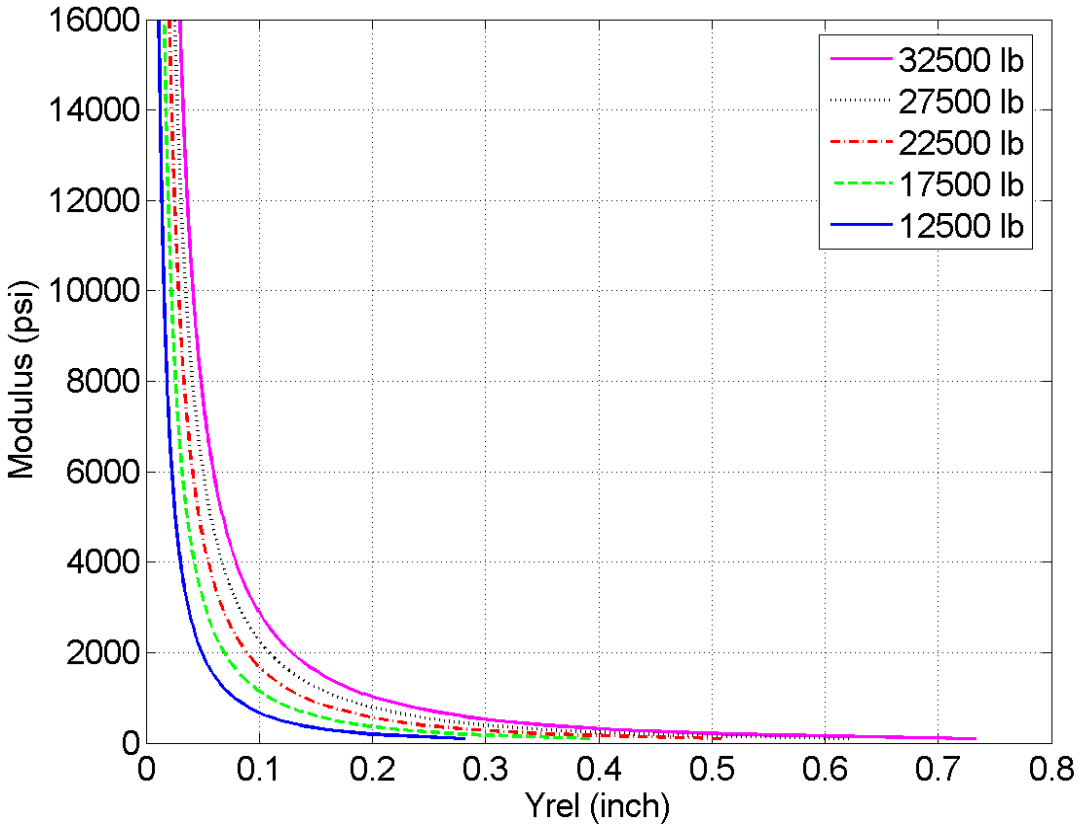

Figure 3-15: Effect of Different Loads on Yrel-Modulus Relation

4 MEASUREMENT SYSTEM

In this chapter, all of the components of the measurement system will be described in detail. These components include sensors, GPS and encoder, power supply and management system, remote supervision, data downloading system, and a database for testing results. The methods and procedures of image processing and calibration will be illustrated. The potential errors in the measurements will also be analyzed.

4.1 Instrumentation

The measurement system is installed on a refurbished hopper car. The hopper car is filled with sand such that the total weight of the car and sand is about 260,000 lb. As shown in Figure 4-1, the system includes two rigid beams attached to the side frames (structural members that connect the axles of a truck) of the hopper car, two sensor heads holding cameras and lasers at the ends of the rigid beams, a solar panel array, a GPS (Global Positioning System) antenna on the top of the car and an enclosed box containing two computers, a data acquisition (DAQ) boards and a GPS receiver for on-board image processing and data computation.

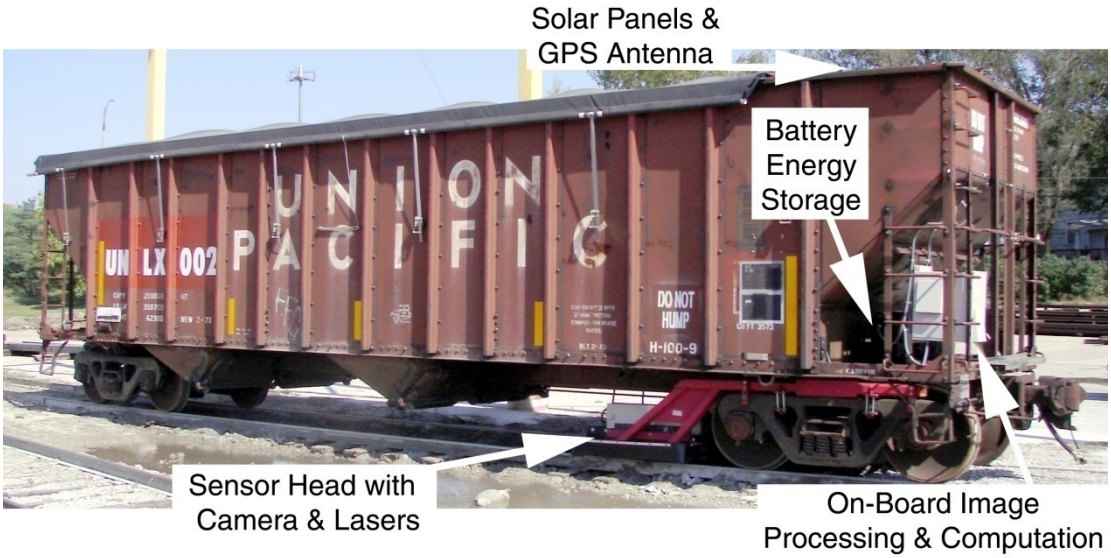

Figure 4-1: System Instrumentation

All of these components will be described in detail in the following sections.

4.1.1 Sensor System

The sensor head is attached to highly rigid steel beams that are fastened to the side frames as shown in Figure 4-2. The beams are bolted to the side frames without modification of the side frames.

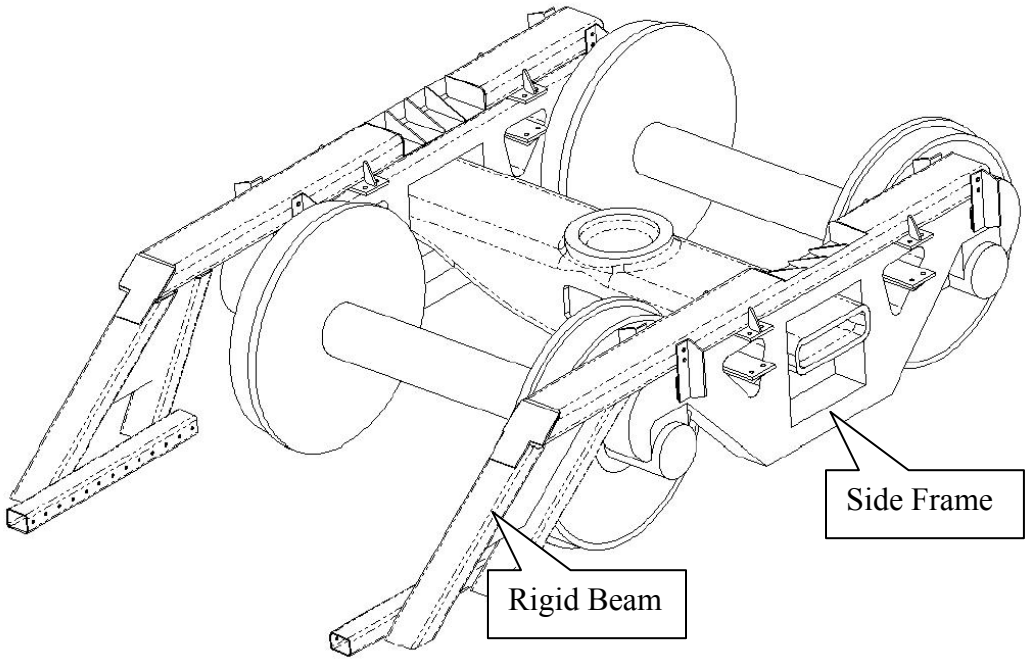

Figure 4-2: Hopper Car Truck and Rigid Beams Assembly

These beams suspend the sensor heads out in front of the wheel/rail contact point and over the top of the rail. Investigations into rigidity have shown that the beams are sufficiently rigid to be considered stationary relative to the side frames (Norman, 2004). Therefore, the measurement will not be affected by the bending or movement of the beams. An actual view of the assembly is shown in Figure 4-3.

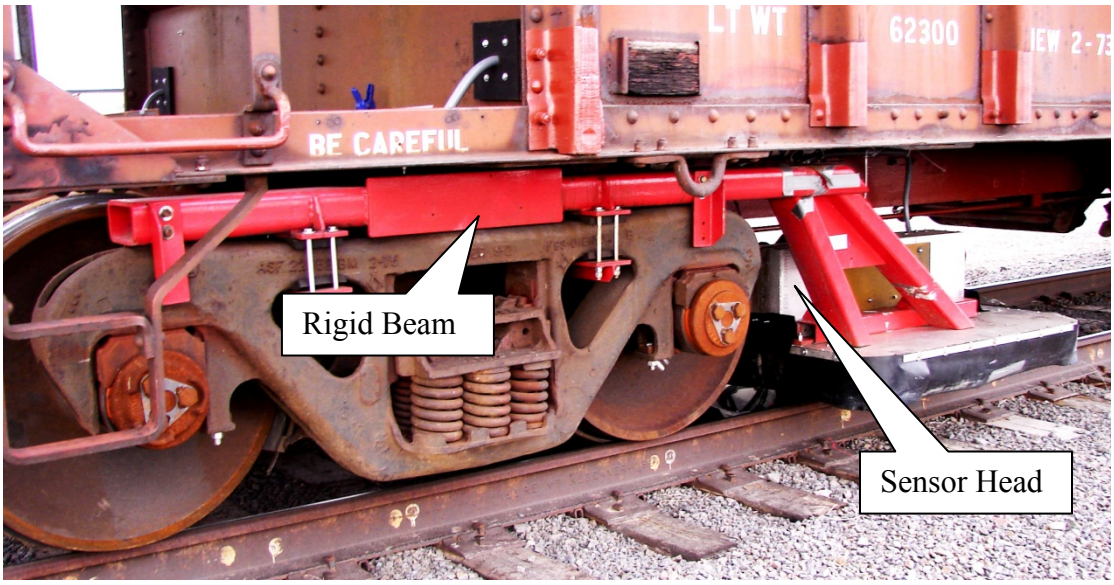

Figure 4-3: The Rigid Beam on the Side Frame

A sensor head holds a digital vision system and two line lasers as shown in Figure 3-2. The camera and line lasers are rigidly attached to an enclosed sensor assembly which is mounted at the end of the rigid beam on the side frame. These lasers are projected at an acute angle (~40˚). They cross and create curves (because of the curved profile of the rail head) across the surface of the rail.

The assembly of the sensor head is shown in Figure 4-4. The two laser holders are adjustable to ensure that the lasers project at an appropriate angle. The height of the camera is also adjustable. This ensures that well-proportioned images will be captured.

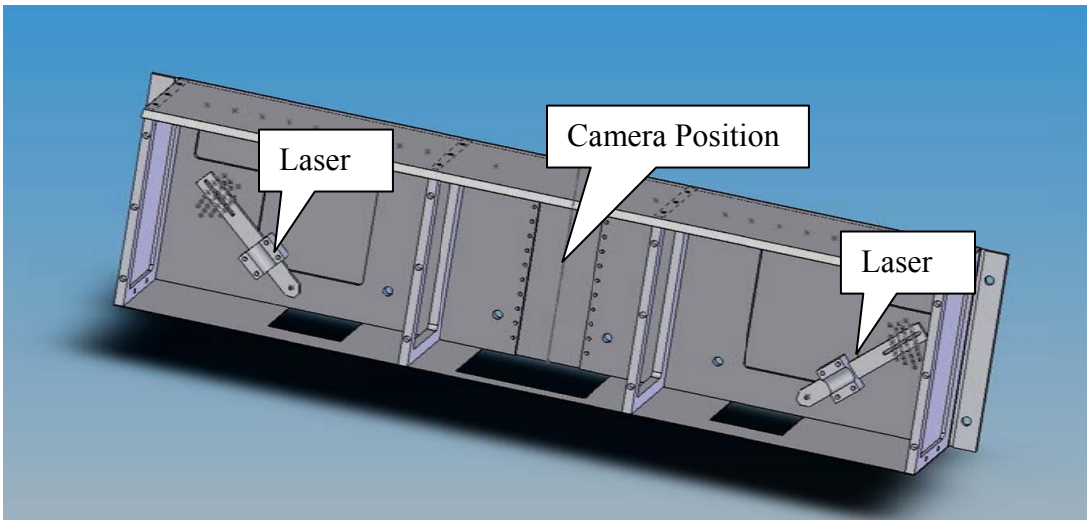

Figure 4-4: Sensor Head Assembly

Ambient light, specifically sunlight, ruins the image of the laser lines across the rail and makes it impossible for the image processing program to distinguish the laser lines. Therefore, a shroud assembly is made to shade the sunlight. The shroud is a light aluminum frame bolted to the bottom of the rigid beam. Rubber landscaping material is attached along the bottom edge to add further shading. This material is flexible, making it resistant to rocks and debris, but is also continuously solid, making it resistant to wind effects. As shown in Figure 4-5, even in very sunny conditions, the shroud provides adequate shading for the lasers and camera image.

Figure 4-5: Shrouds Attached to the Rigid Beams

A typical sensor image is shown in Figure 4-6. The video image shows the laser beams intersecting the top of the rail. Images are captured and processed in real time to output the distance between the laser lines (*d* in Figure 3-2).

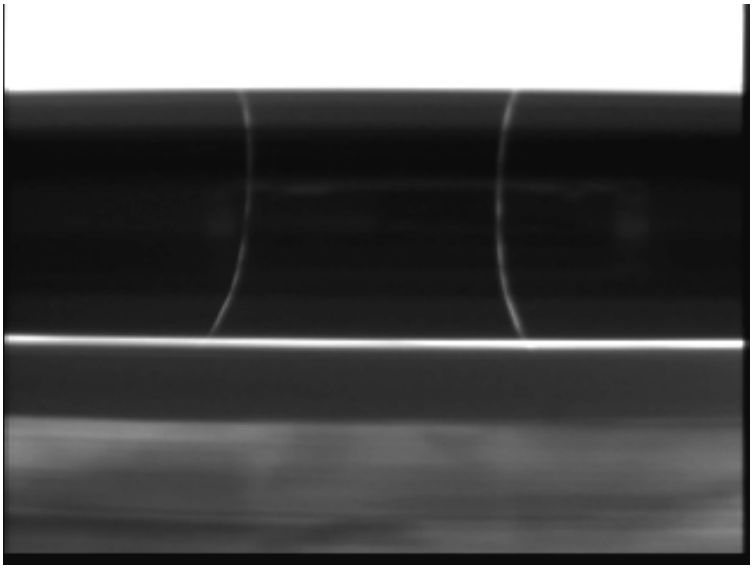

Figure 4-6: Typical Test Image

This measurement is geometrically related to the height of the sensor above the rail (*h* in Figure 3-1). As the sensor moves closer or farther from the rail surface the distance between the laser lines changes. Using a calibration technique which will be described in detail in later sections, Yrel can be calculated from the distances between the laser lines in the images. As the system's output, Yrel is the relative displacement between the rail surface under the camera and the wheel/rail contact line. Yrel can then be mathematically related to track stiffness and modulus (Lu et al, 2007; McVey, 2005; Norman, 2004).

The real-time image processing and data management is performed by computers on board. These computers are installed in an enclosed box as shown in Figure 4-7. A GPS receiver and two DAQ boards are also installed in this box. All of the cables and wiring for the equipments are run through flexible conduits. This sealed box protects the computers and other electrical equipments from harsh environments.

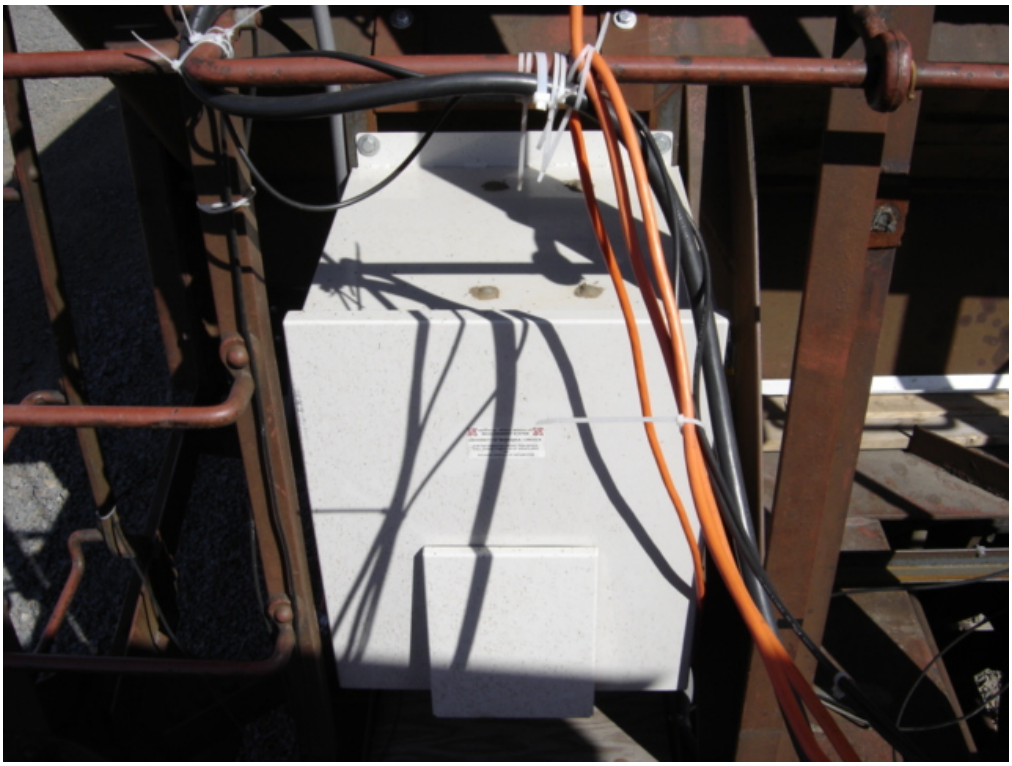

Figure 4-7: Enclosed Box for Computers

4.1.2 GPS and Encoder

The measurement system includes a GPS receiver. The latitude and longitude are reported in real time and recorded in the output data. The GPS data are used to get milepost information by comparing it with Precision Measurement Vehicle (PMV) data and provides accurate coordinates for each location of interest.

The GPS receiver used in the system is a NovAtel OEM4 model which is capable of absolute single-point positioning accuracies of 1.8 meters circular error probable (CEP) (GDOP (geometric dilution of precision) < 2; no multipath). However, this level of accuracy is really only an estimation, and may vary widely depending on numerous GPS system biases, environmental conditions, as well as the GPS receiver design and engineering quality.

Numerous factors will influence the single-point position accuracies of any GPS receiving system. As the following list will show, a receiver's performance can vary widely when under the influences of these combined system and environmental biases:

1. Ionospheric Delays. The Earth's ionospheric layers cause varying degrees of GNSS (Global Navigation Satellite System) signal propagation delay.
2. Tropospheric Delays. The Earth's tropospheric layer causes GNSS signal propagation delays.
3. Ephemeris Errors. Some degree of error always exists between the broadcast ephemeris' predicted satellite position and the actual orbit position of the satellites.
4. Satellite Clock Errors. Some degree of error also exists between the actual satellite clock time and the clock time predicted by the broadcast data.
5. Multipath. Multipath signal reception can potentially cause large pseudo range and carrier phase measurement biases.

In general, all these factors combined may cause an error of up to 60 feet. GPS errors may cause problems when data from multiple tests are compared in trending analysis, because data from different tests may be out of alignment. As a result, data pre-processing will be needed to align the data before comparison.

In order to obtain more accurate and reliable GPS readings, a more sophisticated differential GPS system was proposed to upgrade the current GPS system. Some differential GPS systems can achieve an accuracy to within centimeters.

Due to the GPS error, there may be some stretches in the data in terms of mileposts. An encoder has been introduced into the system to eliminate this stretching problem caused by the GPS error.

4.1.3 Power Supply and Management System

Two rugged computers are used to process images in real time and save the data. In order to reduce power consumption when the testing vehicle is not moving, the whole measurement system enters a "sleeping" mode in which the lasers and cameras are turned off and the PCs remain in standby mode. The total power consumption is about 50 watts when the system is in full-on testing mode and 10 watts in sleeping mode.

An on-board power supply and management system was developed to make automated testing possible. As shown in Figure 4-8, four solar panels installed on the top of the testing vehicle provide the power source for the measurement system. The solar panels are rated at 400 watts maximum. A battery pool consisting of eight deep-cycle marine batteries is used as energy storage and as a buffer to provide stable and consistent power to the system during both day and night. The eight batteries have a total capacity of 400 Amp-hours which can supply 4 days of continuous testing or 16 days of "sleep" mode without inputs from the solar panels. The batteries are enclosed in the black box as shown in Figure 4-8 along with a solar panel voltage regulator which manages the battery recharge process and prevents the batteries from being overcharged. Inside of the battery box, two watt meters were also installed to provide information about the measurement system's energy usage and energy input from the solar panels.

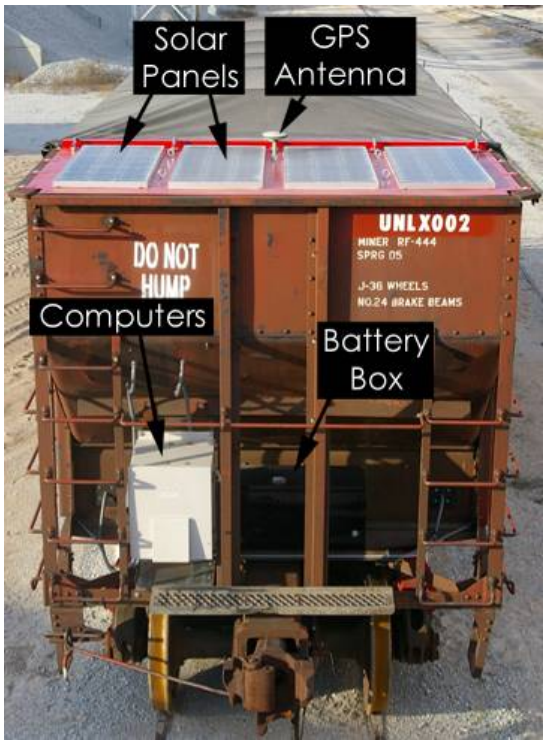

Figure 4-8: Power Supply System

The power supply system has proved to be sufficient and reliable during automated tests in March and April of 2008. In these tests, the batteries were returned fully charged after the six-day, 1300-mile-long journey.

4.1.4 Remote Supervision and Data Downloading

The voltage across the batteries, the current input from the solar panels and the ambient temperature are monitored by the computer in the white box shown in Figure 4-8. This information can be recorded and sent back to a server on the internet through wireless communication which enables the power supply system to be remotely monitored.

The data which were logged and uploaded in real time from the computer on board to a remote server through the internet during the test in April of 2008 are

displayed in Figure 4-9. As shown by the current and voltage traces in this figure, the batteries were charged during the daytime. The output of the solar panels was measured as high as 150 watts. The highest output from the solar panels usually occurred in the morning to compensate for the power consumption during the nights. While in sleeping mode, the batteries can be fully charged before noon and the voltage of the batteries will remain constant for the rest of the day.

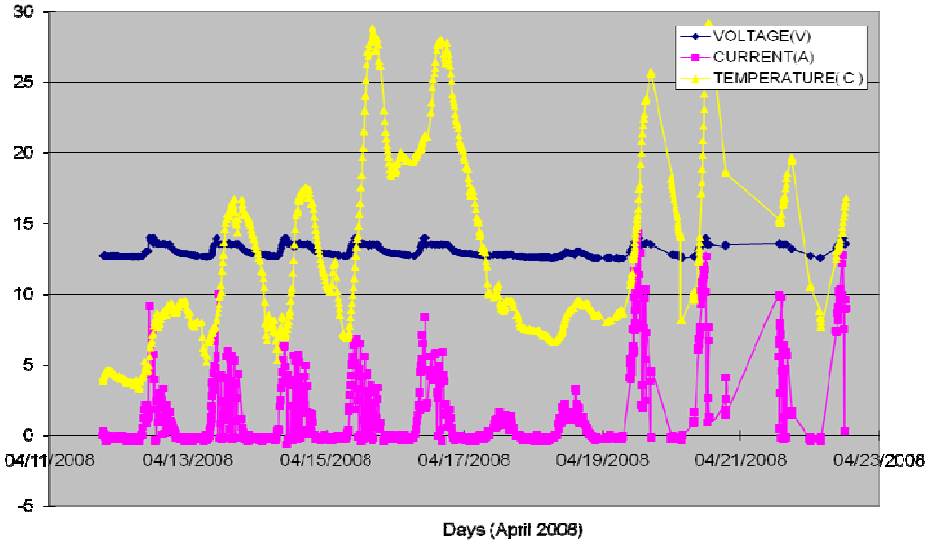

Figure 4-9: Power Supply System Monitoring Information in the April 2008 Test

4.1.5 Testing Results Database

The testing vehicle has been tested on thousands of miles of track. As a result, huge amounts of data have been produced from these tests. Therefore, a database was set up to organize and manipulate these data. A website was created to search through the database and to develop plots. A screenshot from this website is shown in Figure 4-10. The website can also produce lists of exception locations from the database and plot them on maps as shown in Figure 4-11.

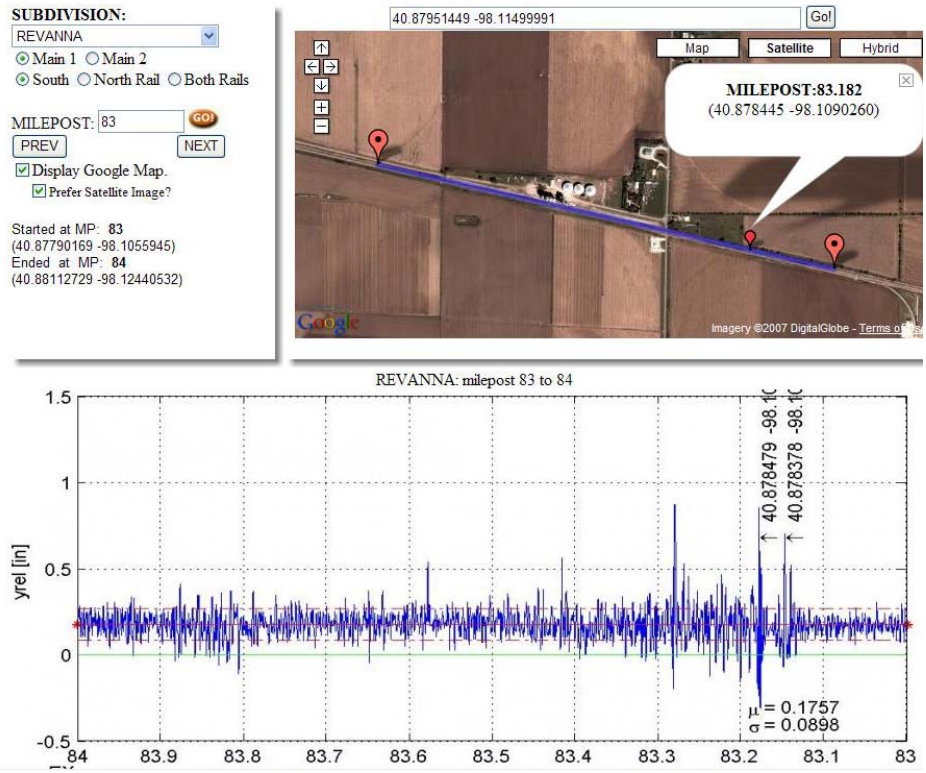

Figure 4-10: Database Website Screenshot

	MILEPOST	Yrel-mean	sigma-ratio	sigma	mean	Latitude	Longitude	Track	Rail	Direction
1	58.812	1.210	14.010	0.090	0.070	41.33039474	-102.13791656	2	NORTH	SM-NP
2	142.437	1.210	8.870	0.140	0.170	41.81102753	-103.59835815	1	NORTH	NP-SM
3	114.192	1.180	13.940	0.080	0.160	41.68216324	-103.09439087	1	SOUTH	NP-SM
4	58.813	1.180	12.070	0.100	0.070	41.33039856	-102.13793945	2	SOUTH	SM-NP
5	115.442	1.180	10.450	0.110	0.150	41.68928528	-103.11663055	1	SOUTH	NP-SM
6	115.124	1.160	7.200	0.160	0.200	41.68748474	-103.11096191	1	NORTH	NP-SM
7	105.108	1.140	9.580	0.120	0.090	41.62158585	-102.93901825	2	NORTH	SM-NP
8	115.452	1.100	9.370	0.120	0.120	41.68927765	-103.11681366	2	NORTH	SM-NP
9	93.489	1.060	19.190	0.060	0.060	41.55511475	-102.73339844	2	SOUTH	SM-NP
10	158.126	1.030	12.400	0.080	0.130	41.93171692	-103.86266327	1	SOUTH	NP-SM
11	94.694	1.030	25.110	0.040	0.090	41.56366730	-102.75334930	1	SOUTH	NP-SM
12	105.106	1.020	8.060	0.130	0.060	41.62157822	-102.93900299	2	SOUTH	SM-NP
13	-0.110	0.980	13.720	0.070	0.100	41.16049194	-101.07314301	2	NORTH	SM-NP
14	56.286	0.940	8.520	0.110	0.100	41.31824875	-102.09281158	2	SOUTH	SM-NP
15	137.961	0.930	10.640	0.090	0.130	41.78478622	-103.51911163	2	NORTH	SM-NP
16	123.100	0.920	15.840	0.060	0.140	41.71881866	-103.25904083	1	NORTH	NP-SM
17	142.414	0.910	10.330	0.090	0.150	41.81090164	-103.59796143	1	NORTH	NP-SM
18	147.296	0.910	10.330	0.090	0.140	41.84682465	-103.67591095	1	NORTH	NP-SM
19	145.501	0.900	6.290	0.140	0.150	41.82800293	-103.65322113	2	NORTH	SM-NP
20	55.307	0.880	6.840	0.130	0.100	41.31840134	-102.07398224	2	SOUTH	SM-NP

GOOGLE MAP

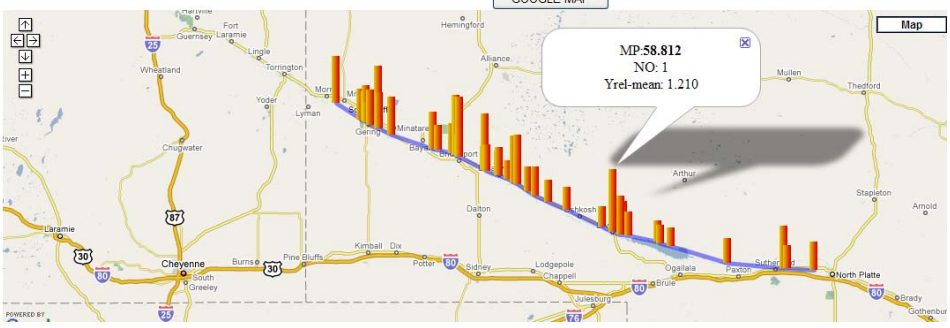

Figure 4-11: Exception Locations List from the Website

4.2 Real-time Image Processing

4.2.1 Basic Algorithm

In the typical image captured during the test shown in Figure 4-6, the laser lines are easily identifiable on the top of the rail. The image processing program scans through all the pixels on each horizontal line of the image and finds the peaks of the pixel intensities which represent the locations of the laser lines. Subsequently, the laser lines can be reproduced as shown in Figure 4-12. After scanning through the image and obtaining the valid points on each laser line, some points may be considered as valid but out of the curve due to reflections on the rail surface or other noise captured in the images as shown in Figure 4-13. These outliers are filtered out and cubic curves are applied to fit the remaining valid points.

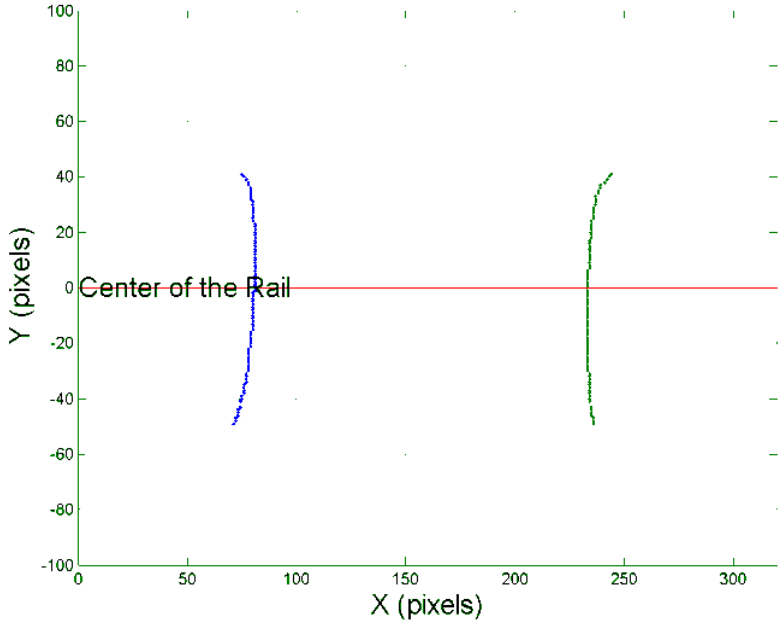

Figure 4-12: Reproduced Laser Curves

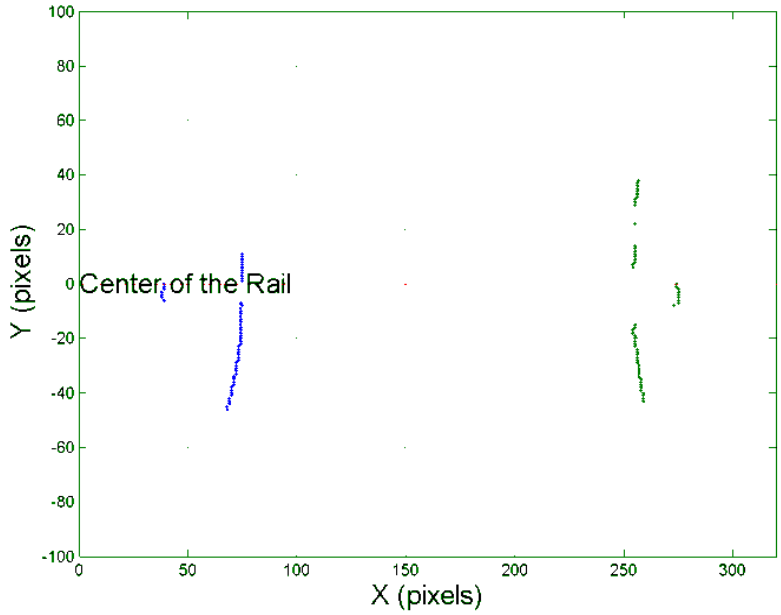

Figure 4-13: An Imperfect Image Example

4.2.2 Verification Using Neural Networks

The current image processing method for the measurement system has some limitations when the system works under certain extreme conditions and the images captured are not ideal. The image in Figure 4-6 is a typical one captured by the system. In this image, the laser curves only appeared on the top of the rail and they are clear and easy to identify. However, images like the one in Figure 4-14 are not ideal to process. In this image, the lasers lines projected on the bottom of the rail and tie were captured by the camera and bright reflections appear on top of the rail. These effects may cause the program to obtain incorrect distances between the laser curves.

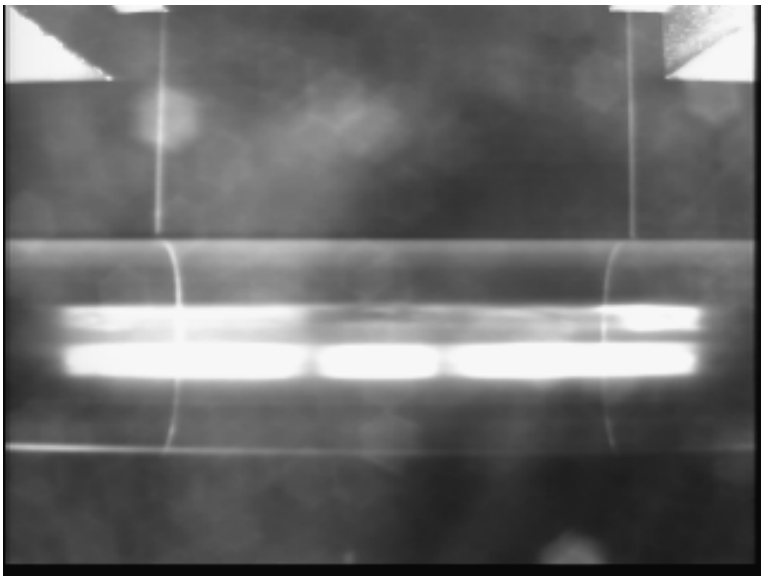

Figure 4-14: Various Images Captured by the Camera

In order to avoid false alerts caused by incorrect image processing, a neural network is introduced into the system to verify the image processing. Based on the image processing algorithm, a few elements were determined to be important indicators of how well images were processed.

First, the number of valid points on each laser line is a key parameter in the image processing. The program scans through all the pixels on each horizontal line in the image and finds the peaks of the intensity which represents the location of the laser curves on the top of the rail. However, if there is no obvious peak on some horizontal line, the program will conclude that no laser curve was found in this location. After scanning through all of the horizontal lines, only the valid points compose the curves. Therefore, the number of valid points on each laser curve indicates how well the curves were interpreted.

Another factor consists of determining the number of outliers. There may be some points valid but out of the curve. The program will filter out these outliers. Better image processing is achieved with fewer outliers.

The standard deviation of the fitting curve is a third consideration in the image processing. After filtering out all the outliers, the program will fit remaining valid points to a cubic curve and calculate the standard deviation of the fitting. Smaller standard deviation indicates better image processing.

The position of the center lines between the two lasers presents yet another issue for image processing, because in general the two laser curves should be symmetric along the vertical center line of the image.

Finally, the change in rail position from the last two images also plays an important role in the image processing. When the system passes by turnouts, there will be changes in rail and occasionally multiple parallel rails are captured in the image. When the lasers are projected onto multiple rails, it is important to pick the correct rail. Therefore, the position of the rail in the images should not drift dramatically.

The above five parameters were used as inputs to construct a neural network as shown in Figure 4-15. Two units are used in the hidden layer. About 50 images were processed and the five parameters resulting from those images were saved as training samples. Each of these images were then reviewed and assigned to an output based on whether the program processed the image correctly. The network was then trained using these samples and the weighted values were determined.

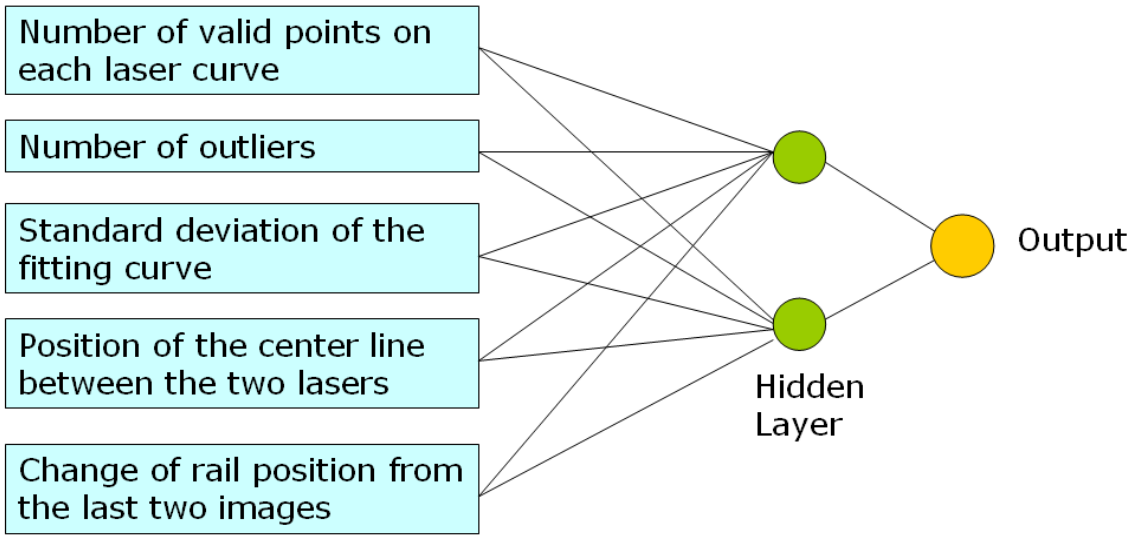

Figure 4-15: Neural Network Structure

The trained neural network was then implemented into the image processing program. Each image is verified based on the output from the network. A threshold of 0.6 was used to decide if the image was processed correctly. Figure 4-16 shows the results output from the program without using neural networks. A number of outliers exist which are caused by incorrect image processing.

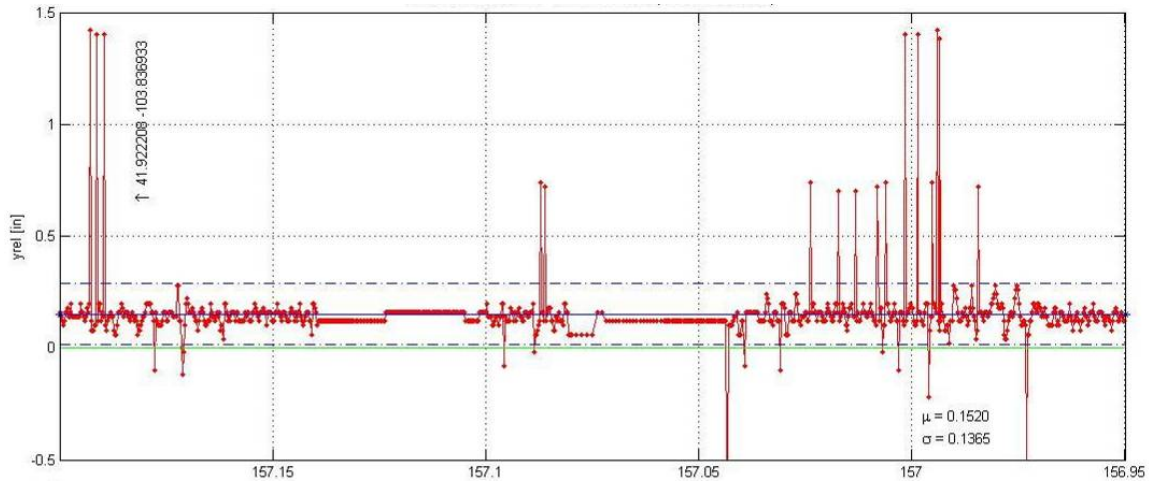

Figure 4-16: Processing Results without Using a Neural Network

The results from the program with the neural network are shown in Figure 4-17. After each image was processed, the neural network was used to verify if the processing was successful. If the output from the neural network indicated the image was processed incorrectly, the result from current processing is discarded and the reading from the last image is saved. As shown in Figure 4-17, all of the outliers were eliminated which shows that the neural network works well to identify the incorrect image processing.

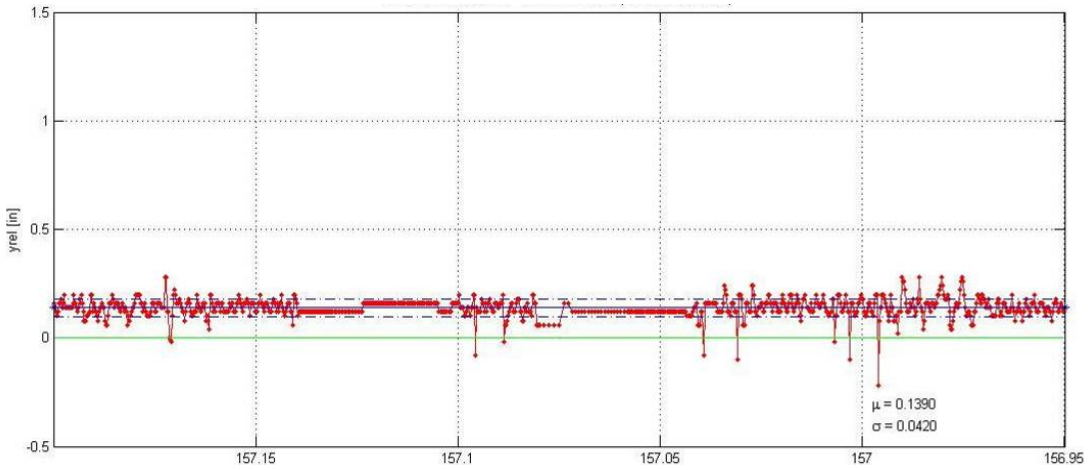

Figure 4-17: Processing Results Using Neural Network Verification

4.3 Calibration Approach and Procedure

As shown in Figure 3-1, Yrel is the relative displacement between the rail surface under the sensor and the wheel/rail contact line. Yrel is the measurement system's output.

The system processes images in real-time and obtains the number of pixels between the two laser lines in the images. This number of pixels is the system's direct

measurement. In order to convert this number of pixels into the value of Yrel in inches, a calibration must be conducted.

The purpose of the calibration procedure is to obtain the relation between the system's direct measurement (*n*, the number of pixels between the laser lines in images) and the expected output (Yrel).

Figure 4-18 shows how to convert the number of pixels into the actual distance in inches. An image of a ruler on top of the rail was captured. The six inch ruler corresponds to 208 pixels in the captured image. Therefore, one inch in the image corresponds to 208/6=34.67 pixels (i.e. if the number of pixels between the two lines is *n*, the actual distance *d* is *n*/34.67 inches).

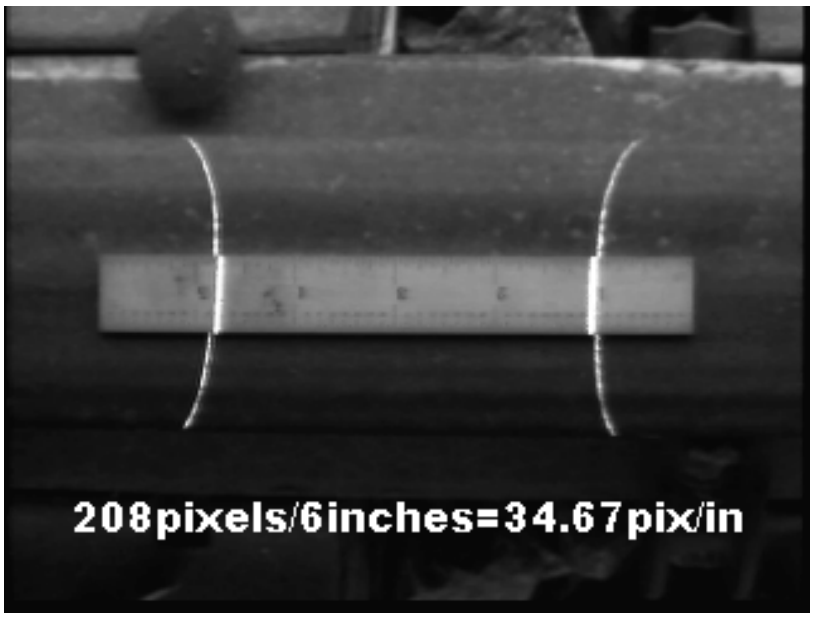

Figure 4-18: Converting Number of Pixels into Distance in Inches

Now the problem consisted of finding the relation between *d* and *Yrel*.

If at one moment, *Yrel=Yrel** and *d=d** are known, and the ratio of *ΔYrel* and *Δd*, ($R = \frac{\Delta Yrel}{\Delta d}$) is also known, then the relationship between *ΔYrel* and *Δd* may be determined as follows:

First, *ΔYrel* and *Δd* may be represented as:

ΔYrel=Yrel-Yrel*

Δd=d-d*

Then it follows that,

$$Yrel = Yrel^* + \Delta Yrel = Yrel^* + R \cdot \Delta d = Yrel^* + R \cdot (d - d^*) \quad \text{Equation 4-1}$$

Therefore, the calibration problem consisted of finding *Yrel*, d** and *R* which involves the following steps.

4.3.1 Finding the Ratio of *Δd* and *ΔYrel* (*R*)

The ratio of *Δd* and *ΔYrel* (referred to as *R*) can be calculated based on the geometry of the laser beams and the rail.

Figure 4-19 is the diagram of the sensor head and the rail.

The distance between the two laser heads is 28.112";

The vertical distance from the laser heads to the top of the rail is 13";

The distance between the two laser lines in the images (d) is 3.768" (131pixels);

Therefore, the ratio of *ΔYrel* and *Δd* is:

$$R = \frac{\Delta Yrel}{\Delta d} = \frac{13}{28.112 + 3.768} = 0.40778$$

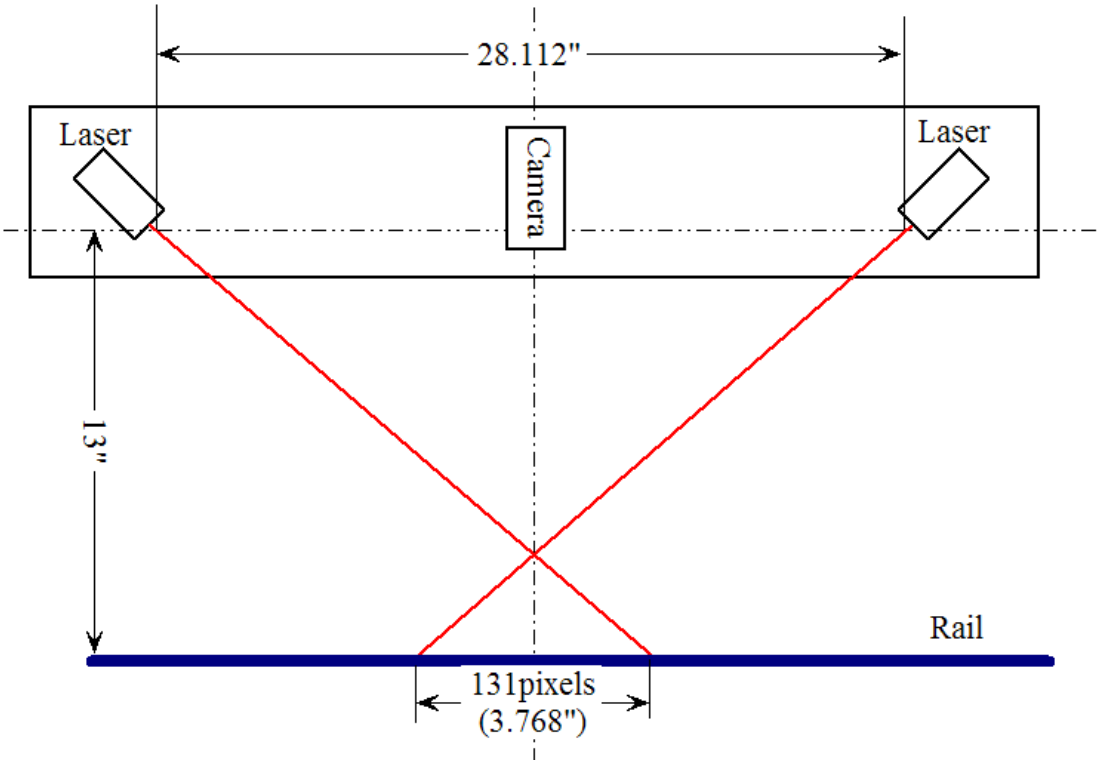

Figure 4-19: Calibration (Geometry of Sensor Head and Rail)

Therefore, one pixel in the image represents $\frac{1}{34.67} \cdot 0.40778 = 0.01176$ inch of $\Delta Yrel$.

4.3.2 Verifying the Ratio of Δd and $\Delta Yrel$ (R)

A special plate is made for this calibration procedure. The device consists of seven steps as shown in Figure 4-20 and Figure 4-21. The lowest step is 1/4 inch high while the other six steps are 1/8" high. When doing the calibration, this plate is placed on top of the rail under the camera, and the two laser lines project onto the plate. Therefore, an image similar to Figure 4-22 is captured by the camera.

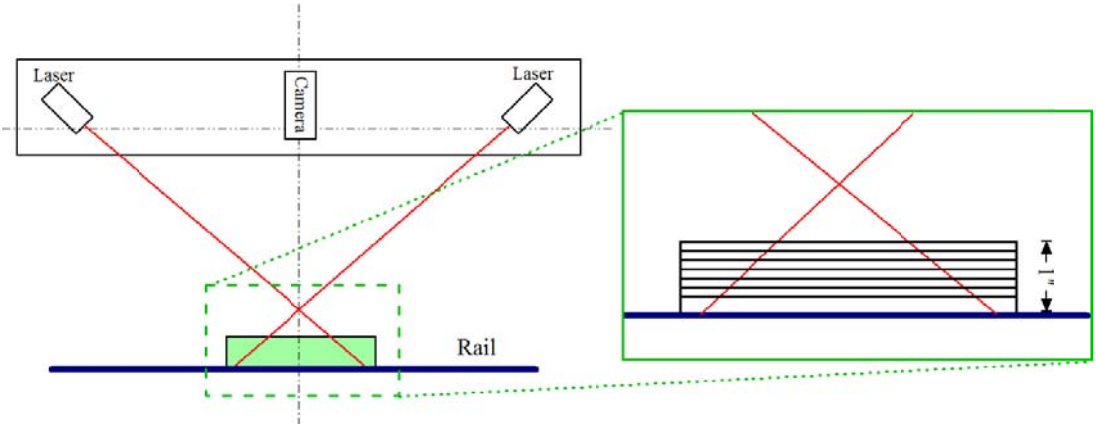

Figure 4-20: Calibration Plate on the Top of the Rail

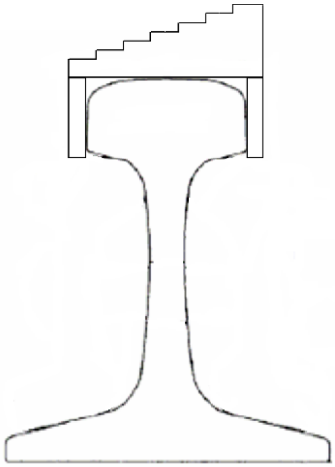

Figure 4-21: Calibration Plate on Top of the Rail (Side View)

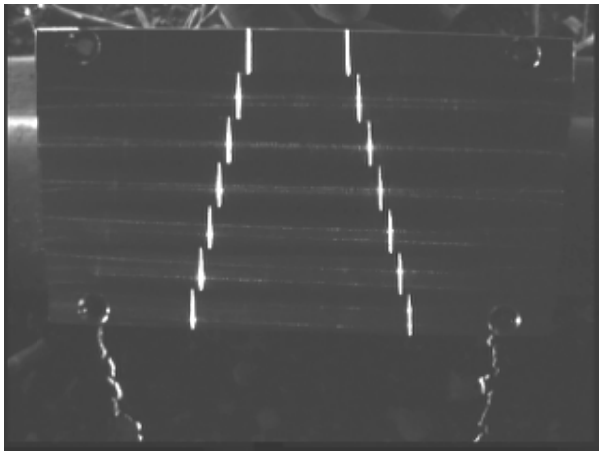

Figure 4-22: Captured Image of the Calibration Plate

The image in Figure 4-22 is then processed. The distances between the laser lines on each step of the plate were obtained and plotted in Figure 4-23 with respect to the step's height above the rail. As shown in Figure 4-23, a linear line fits the data points very well (R^2=0.9988). From the line fit, one pixel in the image represents $\frac{1}{84.857} = 0.01178$ inch of $\Delta Yrel.$

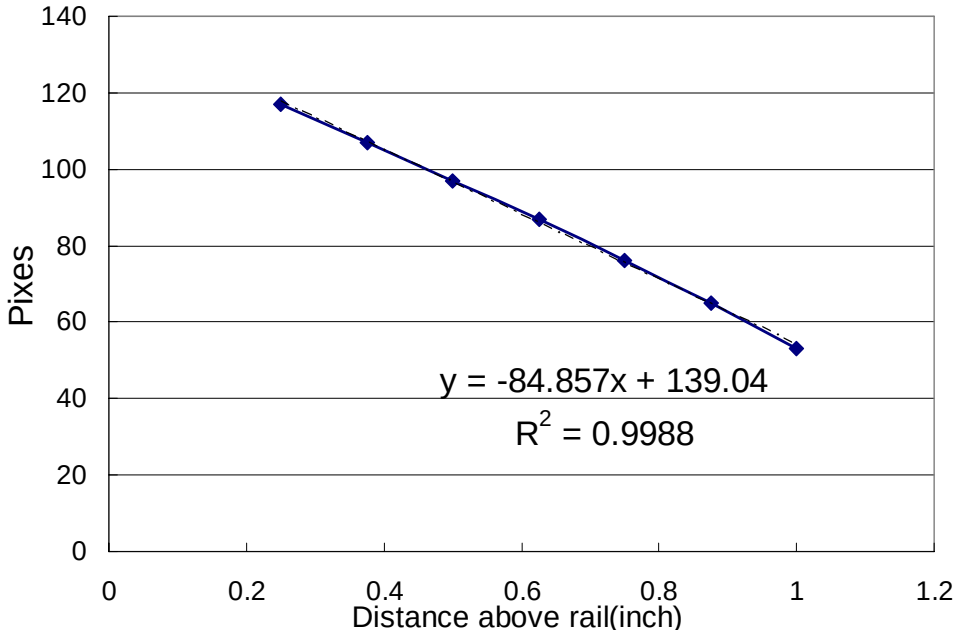

Figure 4-23: Calibration Results

This result verifies the calibration results very well. Based on the geometric relation, one pixel in the images was calculated to represent 0.01176 inch of Yrel. The difference between the results from the two different methods is (0.01178-0.01176)/0.01176 = 0.17% which is negligible.

This difference may be attributed to many factors including the limited resolution of the captured images, the wide laser lines in the images, measurement error during the calibrations, etc. Some of these factors will be discussed in detail in section 4.4.

4.3.3 Finding *Yrel** and *d**

After calculating the ratio of Δd and $\Delta Yrel$, all that is needed is to find a reference point where both the relative deflection (*Yrel*) and the distance between the laser lines (*d*) may be determined.

Assuming that a section of track is perfectly uniform and the modulus over the section is constant, the deflection of the rail under the axles will be identical over the entire section. If a train moves over this section at a very slow speed, the rail deflection at one fixed point as a function of time can be mapped from the time domain into the space domain so that the static rail profile under the axles can be obtained. The dynamic load factor can be ignored since the train speed is slow.

Figure 4-24 demonstrates the setup for capturing the rail deflection with a video camera. A sticker is placed on the side of the rail head as a marker while a video camera away from the track captures this sticker in its view. Another marker is placed on the ballast four feet away from the sticker.

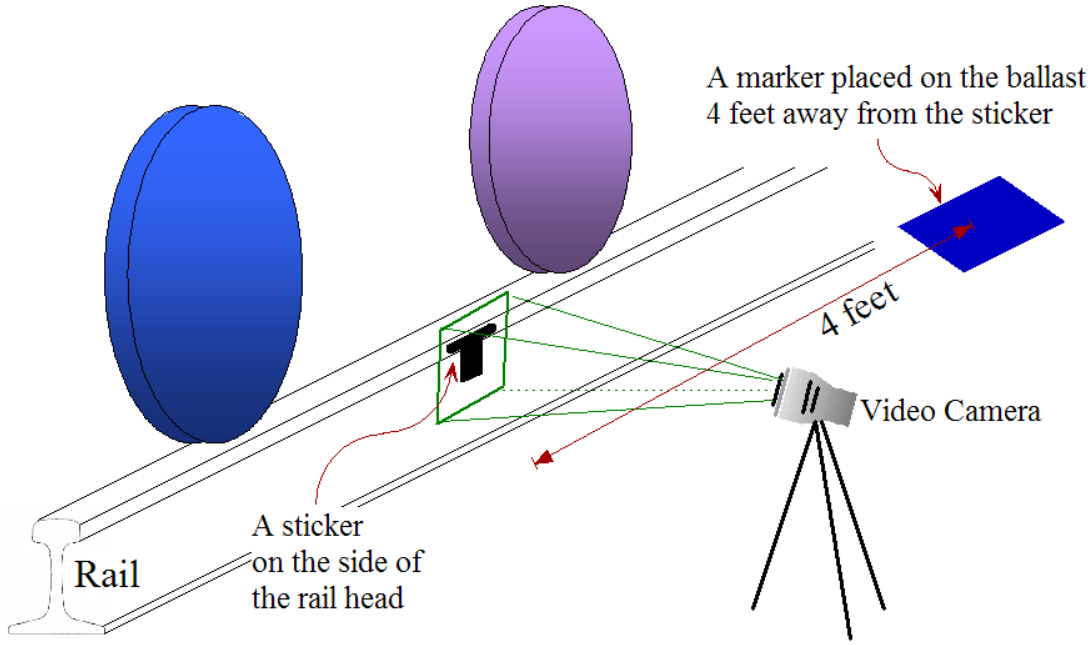

Figure 4-24: Capturing the Rail Deflection with Video Camera

The measurement vehicle is pulled at a constant speed and passes by the video camera. Meanwhile, the video camera captures and saves the video for post-processing. An image from the captured video is demonstrated in Figure 4-25. As the wheels of the measurement vehicle move closer to the position of the marker, the deflection of the rail increases and the marker in the camera image goes down. When the wheels move away from the marker, the marker goes up in the video.

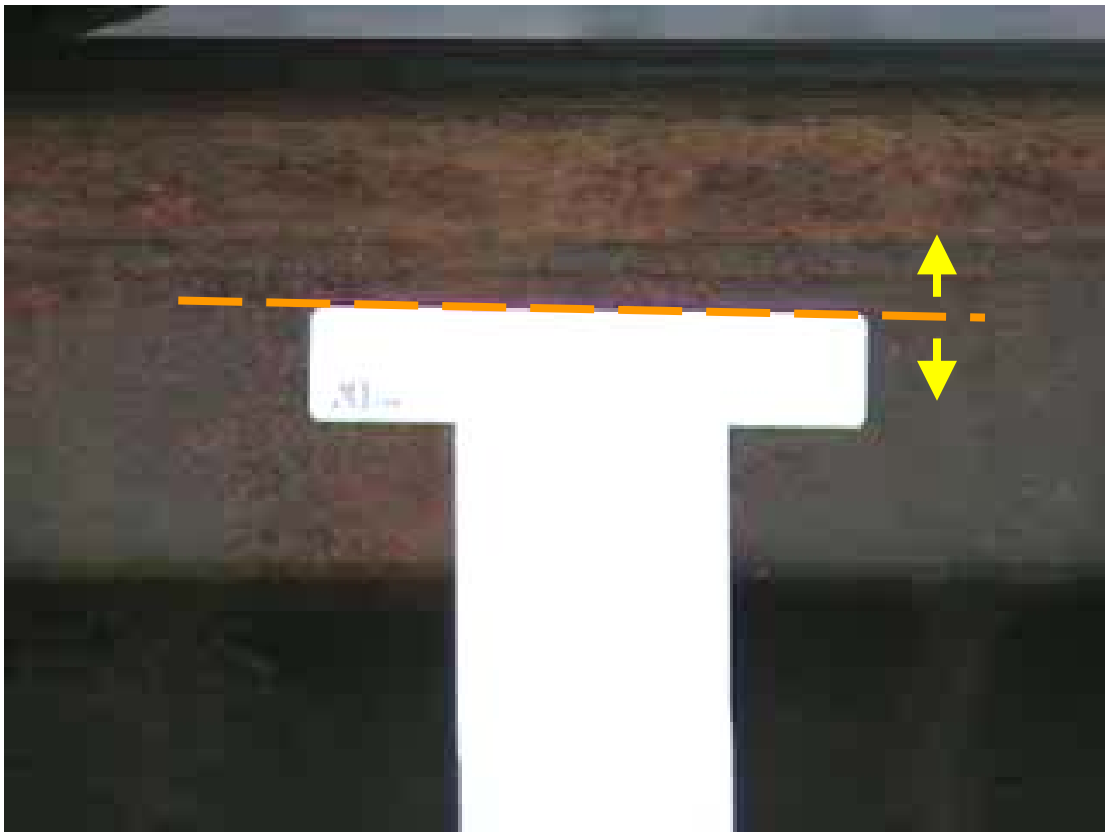

Figure 4-25: Captured Video Showing the Rail Deflection

An image processing program was developed to process the video and determine the vertical position of the top edge of the marker as shown in Figure 4-25. Assuming the deflection of the rail is zero when the locomotive and measurement vehicle are far away from the marker, the vertical position of the marker in the video can then be converted into the actual deflection of the rail which is plotted in Figure 4-26. When the sensor head passes by the marker, the two ends of the shielding shroud will block the marker from the camera view which causes the image processing program to fail during that time. Therefore, *Yrel**, the vertical height difference between the rail surface under the camera and the wheel/rail contact plane, is shown in Figure 4-26. From these calibration data, *Yrel** is 0.045 inch.

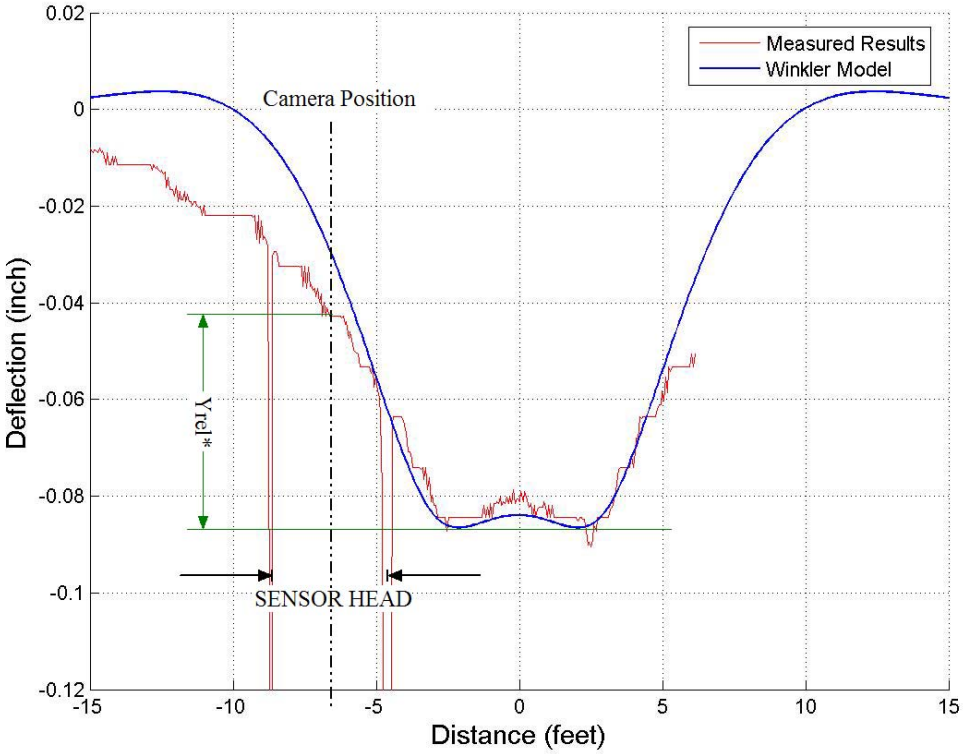

Figure 4-26: The Deflection Curve of the Rail from Calibration

During the calibration procedure, the measurement camera in the sensor head also captures the video of the laser lines on the top of the rail. This video is post-processed to capture the image of the marker placed on the ballast as shown in Figure 4-27. From this image, the distance between the two laser lines (d^*) is obtained.

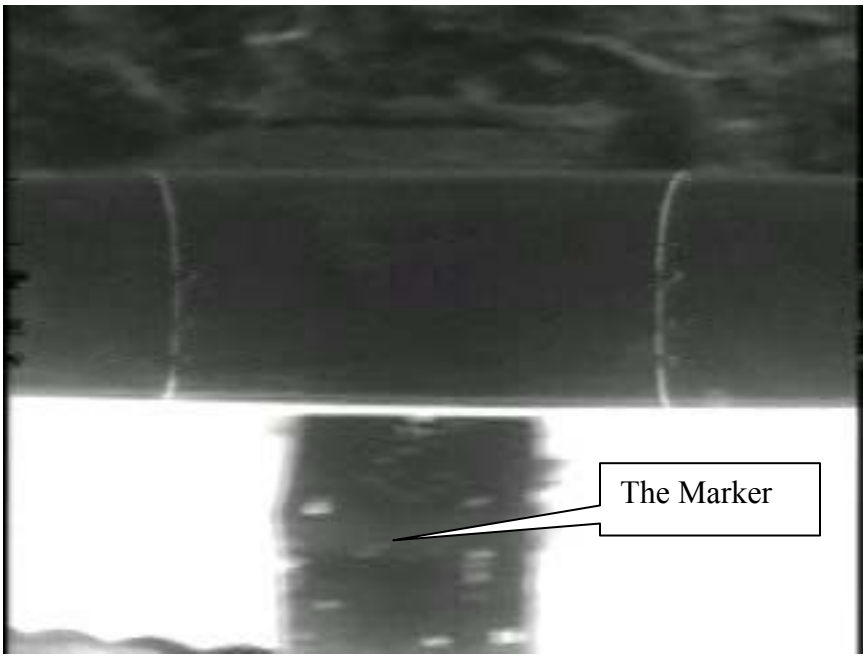

Figure 4-27: Captured Image when Sensor Head Passes by the Marker

This calibration procedure assumes that the section of track (about 40 feet around the sticker's position) is uniform. However, track conditions may change from tie to tie. Even though this procedure was done on a section of specially selected quality track, there is no guarantee that modulus over the section is constant. Therefore, the accuracy of the result is worthy of further examination.

4.3.4 Verifying Calibration Results

After obtaining the ratio of Δd and $\Delta Yrel$, $Yrel^*$ and d^*, the distance between the two laser lines in the images can be converted into the measurement results, *Yrel*, by applying Equation 4-1. However, as stated above, it is difficult to accurately determine $Yrel^*$ and d^*. Therefore, another procedure was developed to verify $Yrel^*$, d^* and the entire calibration results.

A mechanical shop for railroad vehicles (shown in the satellite map in Figure 4-28) is involved in this procedure. The track in this shop is assumed to be absolutely stiff such that no rail deflection will be considered when trains move across this section of track. This assumption is reasonable since the track in the shop is in good condition and the rail is supported by a quality concrete foundation.

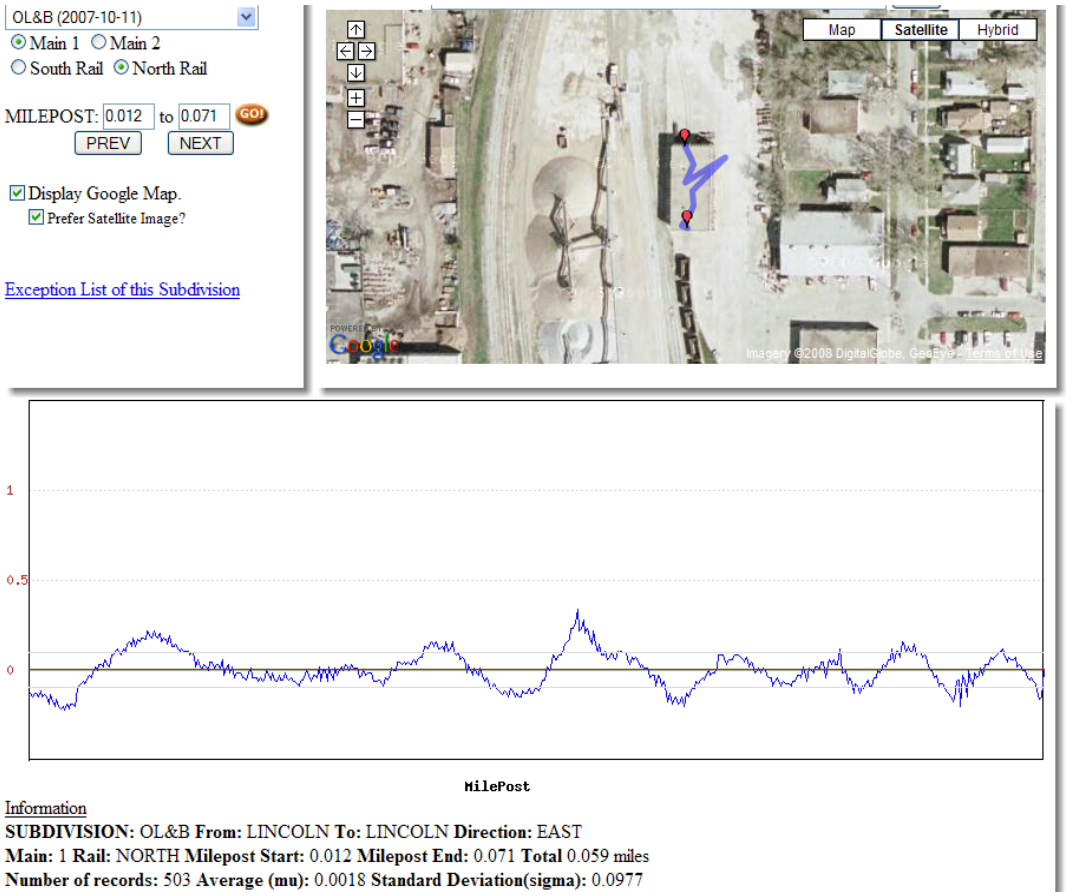

Figure 4-28: Yrel Data from the Mechanical Shop

The results of the Yrel data for this section of track are plotted in Figure 4-28. As shown in the information section of this figure, the average of Yrel over this section of track is 0.0018". Since this value is very close to zero, it confirms the calibration results very well. The variations of Yrel, which are relatively small (standard deviation is less than 0.1"), are attributed to the pre-existing geometry variations of the track.

4.4 Error Analysis

System's measurement error will be discussed in this section. The potential factors causing measurement errors include limited sampling rate, the wide laser lines in images and the laser beam drifting.

4.4.1 Errors Caused by Limited Sampling Rate

The cameras in the current measurement system produce analog video signals in NTSC standard which is 30 frames per second. As a result, individual data points are spaced approximately every two feet when the measurement vehicle travels at 40 mph. However, Yrel measurements may change considerably within two feet since certain track modulus and geometry variations occur over extremely short distances. Therefore, this limited sampling rate may result in measurement errors.

For example, 50 feet of data is presented in one-foot increments in Figure 4-29. The highest peak within the 50 ft range is point B, which is 0.77". If the test is conducted at a speed of 40 mph, the system will record readings every two feet. As a result, the peak at point B could be missed while only the data points at A and C would be recorded. Hence, an error of 0.04" (the difference between point A and B) would result. Since the errors based on limited sampling rate depend on how the actual data varies over short distances they are difficult to quantify. Some locations such as joints are much more sensitive to this sampling rate issue because the actual Yrel data can change dramatically over a few ties. Based on examination of the data from past tests, the error could be up to 0.2" at some locations.

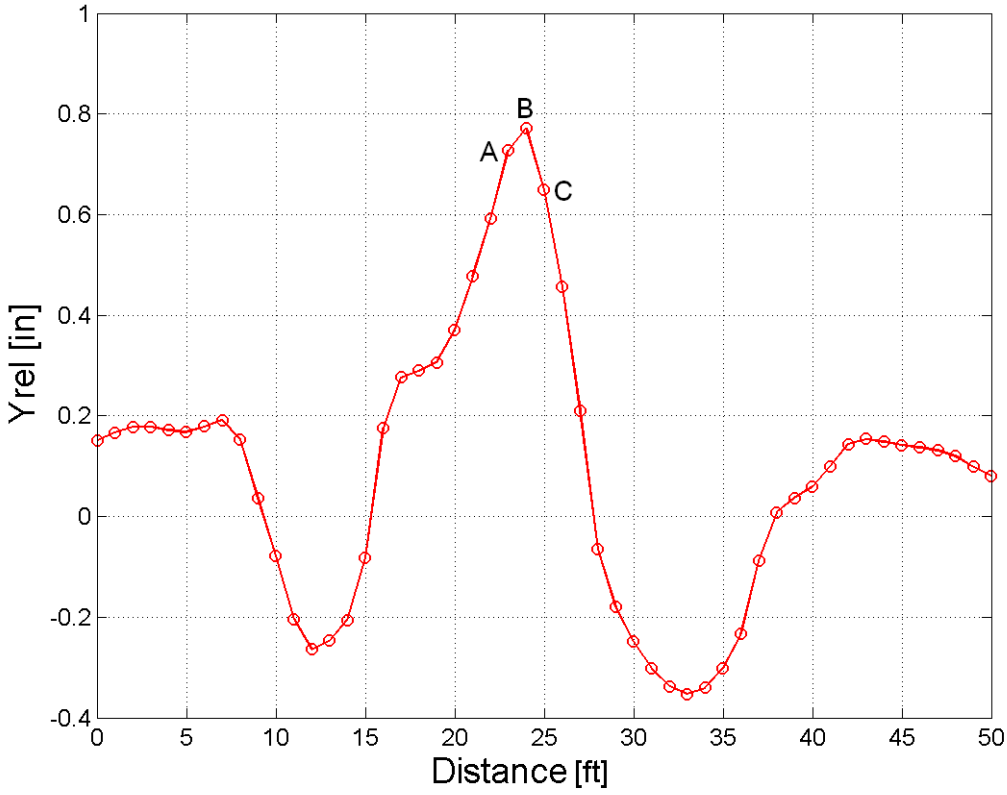

Figure 4-29: Limited Sampling Rate Causing Measurement Errors

To address the problem caused by the limited sampling rate, high-speed cameras are proposed to upgrade the system's sampling rate to 120 frames per second. Therefore, the data can be collected every six inches at a testing speed of 40 mph. This will greatly improve the system's measurement repeatability and accuracy.

4.4.2 Measurement Resolution

The measurement system is based on image processing. The most direct measurement output is the number of pixels between the two laser lines in the images. Therefore, the measurement resolution is directly determined by the resolution of the captured images.

The current frame grabbers are set to capture images in half frame mode which is 320x240 pixels. Based on the calibration results, for images of 320x240 pixels, one pixel in each image represents 0.0118 inch of Yrel. Hence, the measurement system's resolution is 0.0118 inch.

However, the current cameras and frame grabbers can easily be upgraded to capturing images of 640x480 pixels. In that case, the system's resolution may be improved to 0.0059 inch.

4.4.3 Laser Line Width

The image-processing program identifies locations of the laser lines by finding peaks of pixel intensities. However, as shown in Figure 4-30, a laser line can be as wide as three or four pixels in a captured image. Therefore, it is difficult for the image processing program to precisely distinguish which pixel should represent the location of the laser lines, especially when two adjacent pixels have the same intensity. Although the curve fitting algorithm used in the image processing program greatly reduces the error caused by this factor, it is reasonable to conclude that an error of ±1 pixel (±0.0118" in Yrel) may result.

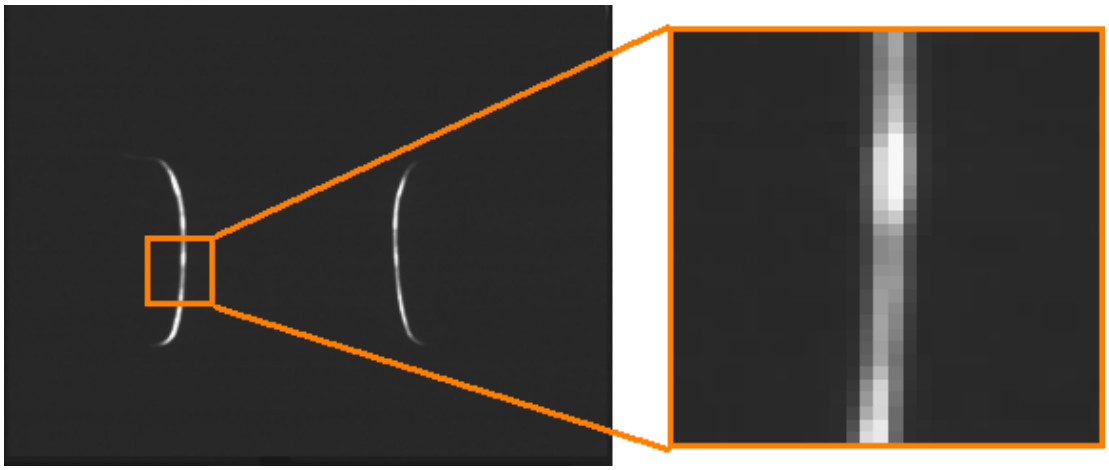

Figure 4-30: Laser Line Width

4.4.4 Laser Beam Drifting

The laser line generator's boresight accuracy is rated at a maximum of 2.5mm/m. Boresight accuracy, known as pointing accuracy, is a measure of the angular difference between the beam propagating axis (where the laser beam is pointing) and the mechanical axis (where the laser housing is pointing). Due to the nature of the measurement principle and the calibration procedure, the boresight accuracy has no effect on the measurement result because the measurement is not related to the mechanical axis of the laser housing at all. As a result, no measurement error is caused by the boresight inaccuracy.

However, pointing stability, a measure of how much the laser beam alignment drifts over a period of time, will cause errors. The laser line generator's pointing stability is rated at <50 μrad. The geometry relation between the lasers and the rail is shown in Figure 4-31, where H is the vertical height of the laser generator above the rail, α is the angle between the laser beam and the vertical direction, $\Delta\alpha$ is the drifted angle and Δd is the drifted distance of the laser line on the rail.

From the geometry relation, we know that

$$\Delta d = H \cdot \tan(\alpha) - H \cdot \tan(\alpha - \Delta\alpha)$$ Equation 4-2

From the calibration, we know H=13.6, α=50°, and the maximum Δα is 50μrad. Therefore, Δd is calculated to be 0.00165 inch. Based on the geometric relation from the calibration, 0.00165 inch in Δd will result in a ΔYrel of 0.00165x0.853=0.0014 inch.

Considering the worst case in which both laser beams are drifting towards the camera at the same time or away from the camera at the same time, the maximum error will be doubled. Therefore, the maximum error of Yrel that the laser beams drifting can cause is 0.0028 inch, which is negligible.

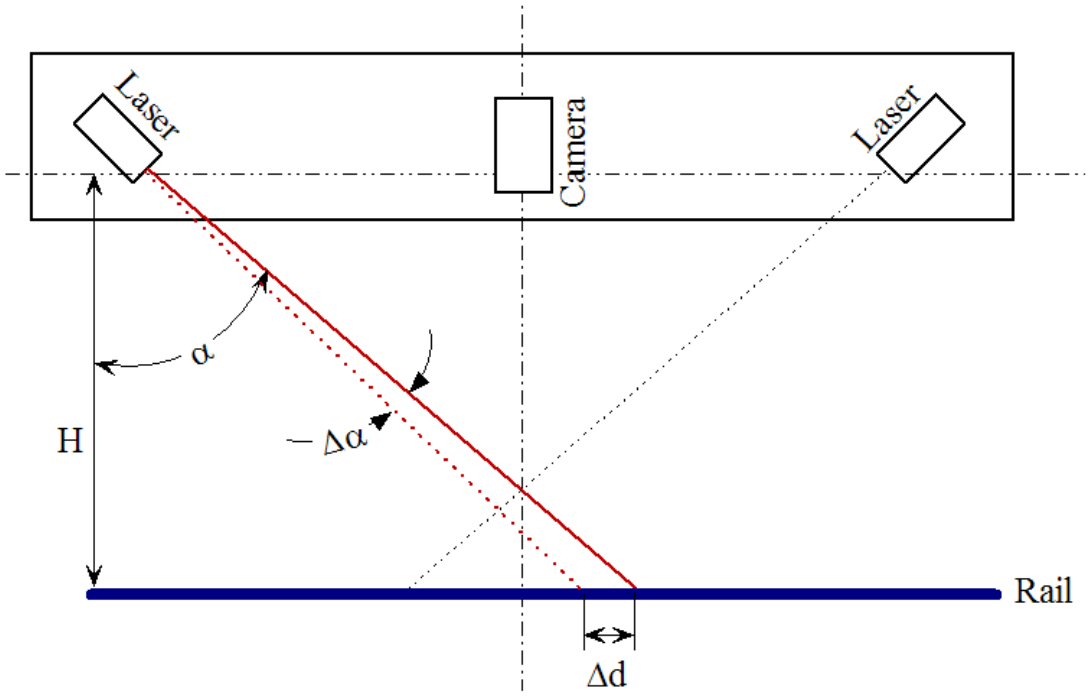

Figure 4-31: Laser Beam Drifting

5 FIELD TESTING AND DATA ANALYSIS

5.1 Revenue Service Testing

Since 2006, the measurement system has conducted revenue service tests in many locations including the Burlington Northern Santa Fe (BNSF) Railway's St. Joseph subdivision in Kansas, and the Union Pacific Railroad (UPRR)'s South Morrill subdivision, Sidney subdivision, Ravenna subdivision and Powder River subdivision in Nebraska. Some short distance tests such as between Lincoln and Ashland, NE and between Lincoln and Tecumseh, NE were also conducted.

Recent tests focused on the 160 miles of heavy axle load freight line of the Union Pacific Railroad on the South Morrill subdivision of the North Platte division. The tests were performed on Main 1 (primarily unloaded with approximately 50 MGT/year) and Main 2 (primarily loaded with approximately 250 MGT/year). Repeated tests were conducted on this subdivision in October 2006, December 2006, February 2007, April 2007, January 2008, April 2008, and June 2008. Tests were done at speeds up to 60 mph in a work train consist. The automated testing ability of the system made these tests easy to conduct and cost-efficient. These repeated tests were performed in different seasons, under different weather conditions, an d at different speeds, providing tremendous amounts of data for analysis. Figure 5-1 shows the measurement vehicle in the consist of a coal train during a test.

Figure 5-1: System in Revenue Service Testing

An example of data recorded over a distance of one mile is shown in Figure 5-2. The plot shows the relative deflection of the rail, Yrel (as defined in Figure 3-1), as a function of GPS coordinates given in degrees of longitude and latitude. The data are overlaid on a satellite image (Google Map). In this figure it is possible to qualitatively trace changes in relative deflection to specific track events such as grade road crossings, culverts, and bridges.

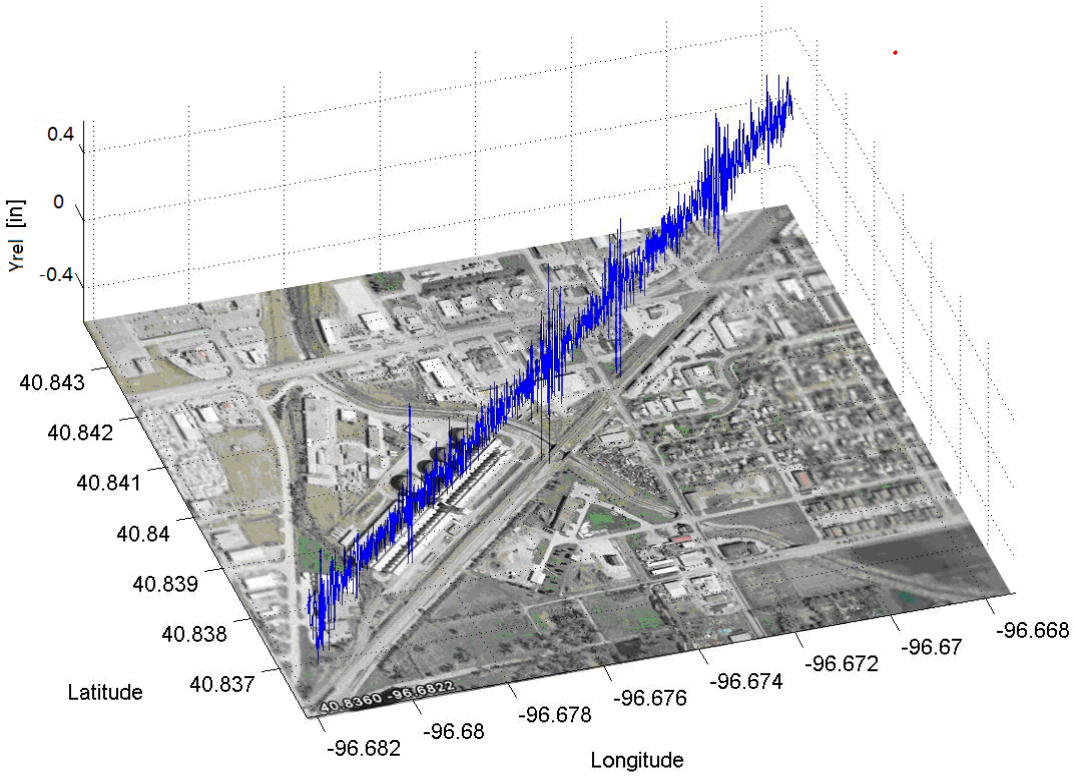

Figure 5-2: Yrel Data Overlaid on a Satellite Map

Figure 5-3 shows data sampled over one mile of track. The plot shows the relative rail deflection between the measurement point and the wheel/rail contact point (Yrel as defined in Figure 3-1). Also shown are the mean and standard deviation of the data. The mean represents the average value over the past 0.1 miles of track and the standard deviation corresponds to the mean over that same distance. This distance was chosen arbitrarily as a characteristic length. The mean and standard deviation are therefore dependent on the direction of travel (right to left in this plot).

This section is an interesting example because it corresponds to a high-speed crossover between MP 0.6 and 0.9. A non-insulated joint bar (near 0.9) is located at the right end of the crossover. The relative deflection at this point became very large (over 1") indicating a very low track modulus. The joint bar failed and caused a derailment

only two weeks after the track modulus measurements were taken. This location represented the second highest relative deflection measurement recorded over the nearly 350 miles of track tested for this portion of the test. This spike in relative displacement obviously caused a jump in both the mean and standard deviation of the data. The other end of the crossover (near MP 0.65) also displayed a rise in the standard deviation, indicating a rough section of track.

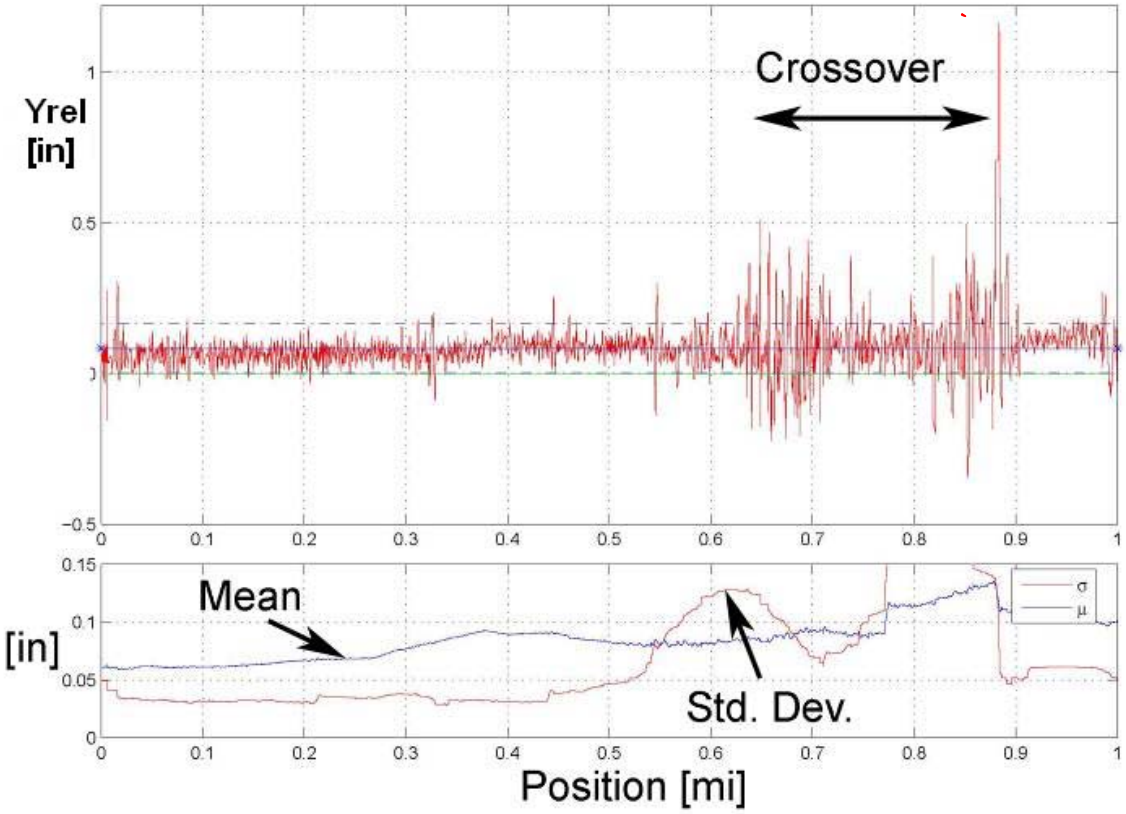

Figure 5-3: A Rough High-Speed Crossover

In contrast to Figure 5-3, an example of one mile of quality track is shown in Figure 5-4. Yrel and therefore modulus were both very consistent over this section of track. The consistent mean and relatively low standard deviation emphasize the track's quality.

The results of these tests suggest that information in these measurements may be useful in indicating unsafe sections of track in need of repair. The contrast between the two figures suggests a quantitative method to more rationally schedule and prioritize track maintenance.

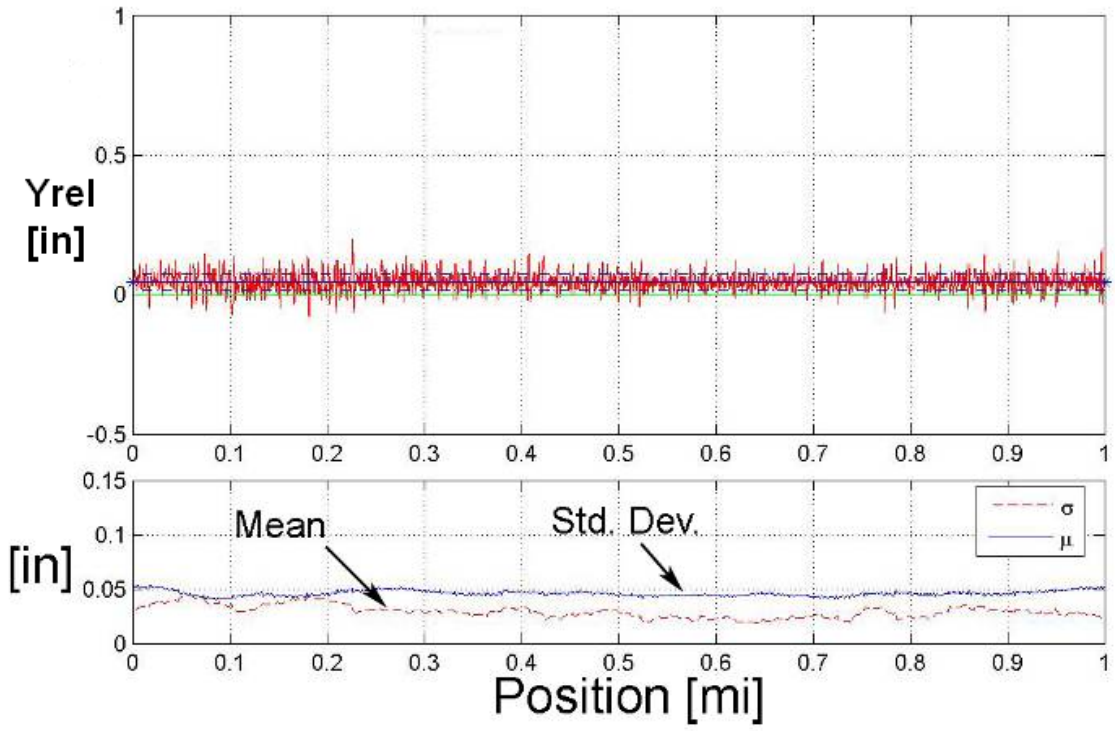

Figure 5-4: Track with Consistent Modulus

5.2 Measurement Repeatability

The multiple tests over the same section of track (South Morrill Subdivision of UPRR) allow for comparison between tests. This comparison highlights the high repeatability of the measurement. At most locations the measurements were very similar for each test.

Measurements over the same section of track from tests in December of 2006, February of 2007 and April of 2007 are shown in Figure 5-5. The measurements from the three different tests show almost no difference over this section of track, which indicates the system's measurement is highly repeatable. The high repeatability of data as shown in Figure 5-5 is observed over most sections of the 320 miles of track in this subdivision.

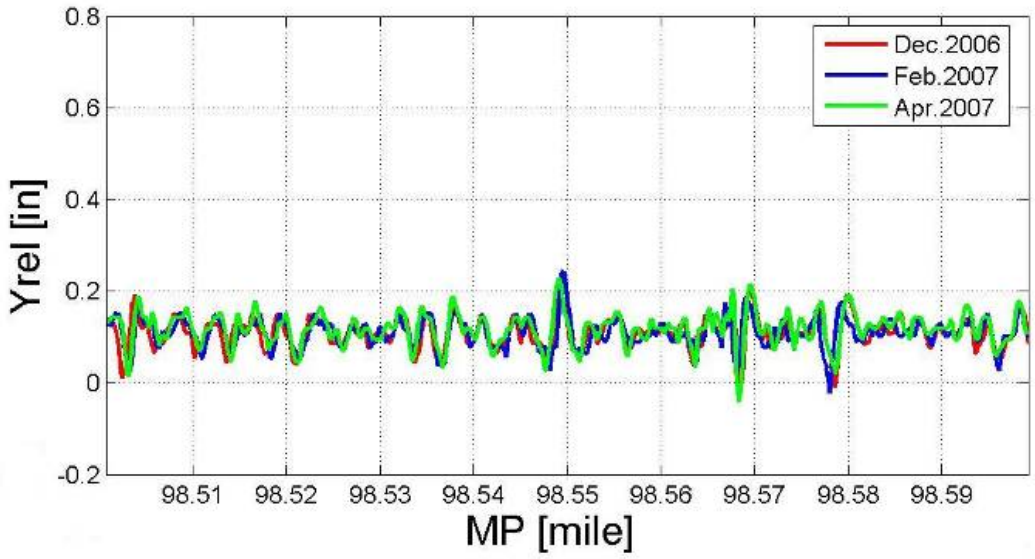

Figure 5-5: Measurements from Multiple Tests

5.3 System Measurement under Various Conditions

The results from multiple tests in South Morrill subdivision also provided abundant data for studies on system's measurement under various conditions such as at different testing speed, under different weather condition, and for different size of rail.

5.3.1 Results From Different Train Speeds

The results of South Morrill subdivision suggest that the measurements are not strongly related to the train speed. The average train speed for the 0.1 miles shown in Figure 5-6 are 48, 22, and 35 mph, respectively.

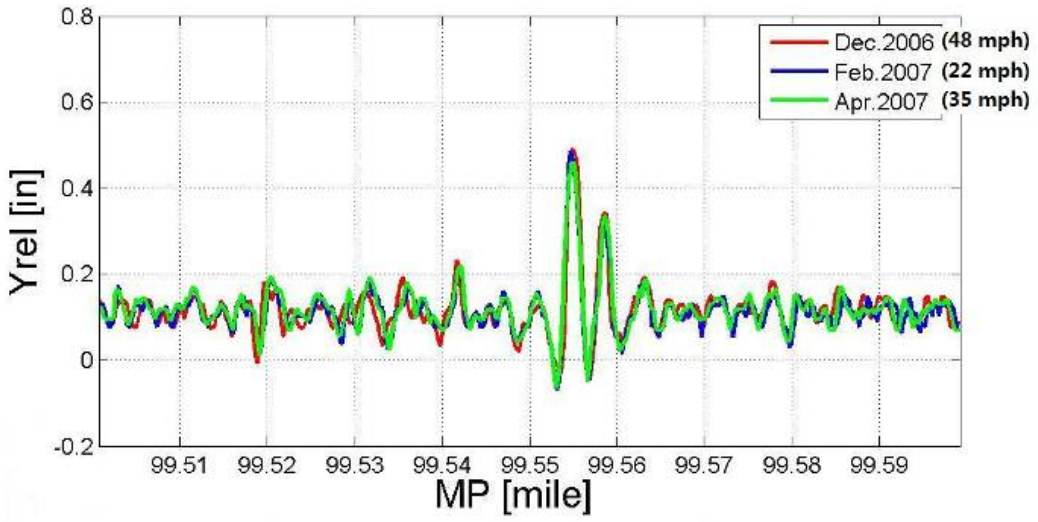

Figure 5-6: Measurements from Different Testing Speeds

Repeated tests over the same section of the track at different speeds were performed during a special validation test on the Yoder subdivision. Four different speeds (20, 30, 40 and 50 mph) were tested. For most of the sections, the measurements from the different speeds are highly repeatable, which indicates that the speed is not a significant factor in the measurements at those locations. However, at some locations differences do exist between the different speeds. The section shown in Figure 5-7 is an example of these locations. The values of the peaks at MP224.4685 corresponding to the four different speeds within this short section (21, 30, 40 and 48 mph) are 0.607", 0.687", 0.692" and 0.77" respectively. The Yrel measurements increased 0.163" when

the train speed increased from 21 mph to 48 mph. This can be explained by the increased dynamic load when the train moves at higher speeds.

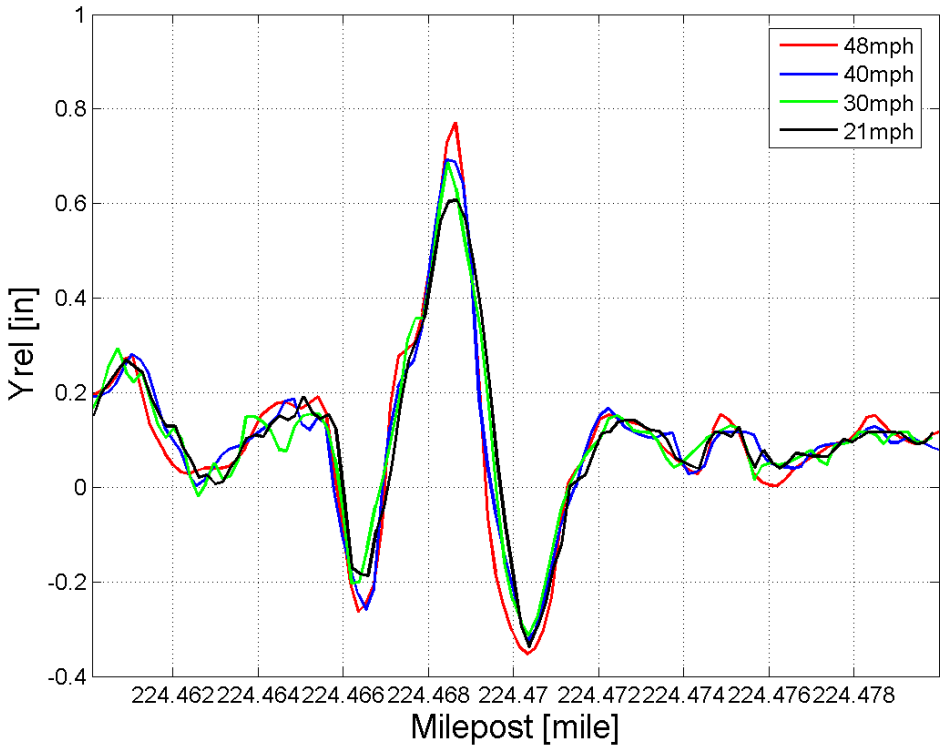

Figure 5-7: Dynamic Loads Effecting Measurements

5.3.2 Results From Different Seasons

Although most of comparisons between tests showed extreme repeatability as shown in Figure 5-5 and Figure 5-6, there were some variations in certain sections of track. The most noticeable variation is the comparison between the December, 2006 test and the other tests. At multiple locations of the track, the relative deflection data (Y_{rel}) from the test in December, 2006 has an offset compared with the results from other tests as shown in Figure 5-8. The test in December, 2006 was special because it was conducted in extreme weather conditions with falling snow and an ambient temperature around a high of 20° F. Figure 5-8 shows similarity in the shape of the measurements,

but a shift in the Test 2 measurement. The December 2006 test has a lower mean value indicating the track is stiffer (smaller Y_{rel}). This could indicate a change in track modulus associated with frozen subgrade that may contain moisture. These results suggest the system could be useful to quantify seasonal variations in track modulus caused by factors such as variations in subgrade moisture.

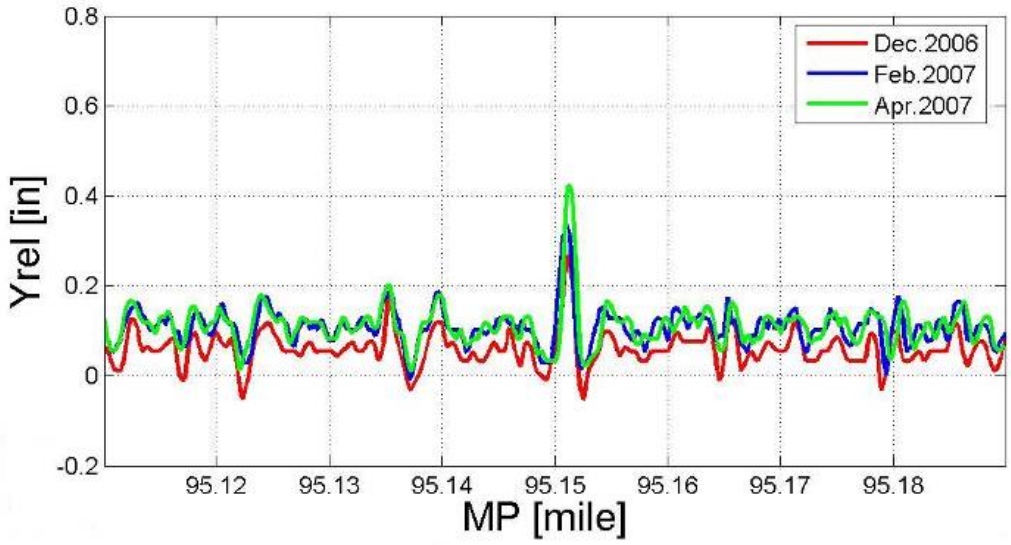

Figure 5-8: Variations of the Measurements

Interestingly, the offset of the measurements shown in Figure 5-8 only occurred at some track sections. Figure 5-9 shows a section of track where only the measurements on the left half of the figure has this offset while on the right half of the figure the results from the three tests are very similar. This could indicate variations of subgrade moisture can lead to greater (or lesser) seasonal variations in track modulus.

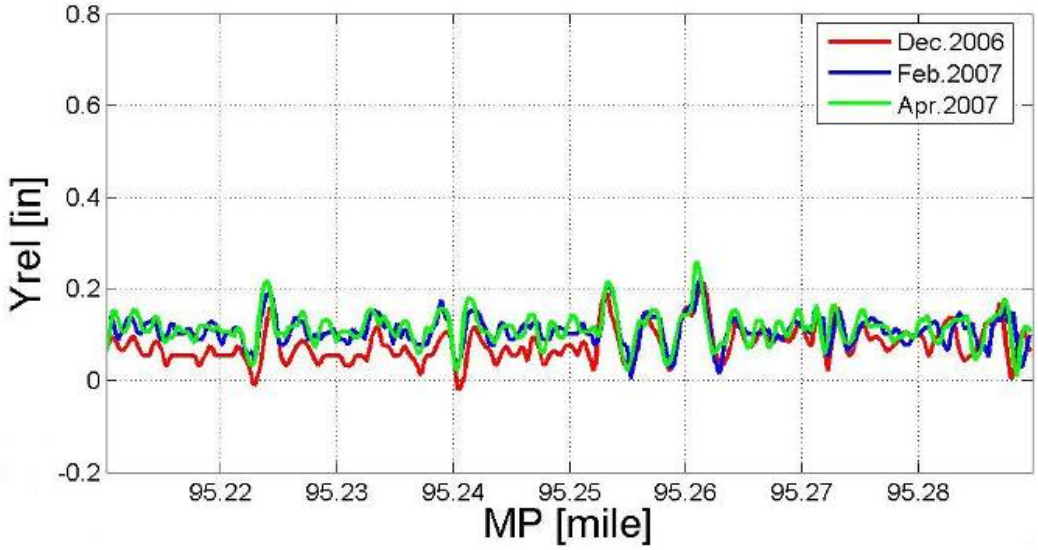

Figure 5-9: Variations in Some Sections of Track

5.3.3 Results from Different Rail Sizes

One method used to inspect the change in Yrel data over long distances up to an entire subdivision is to plot the average Yrel measurement over every 500 feet. The data from three tests on the South Morrill subdivision are presented using this procedure as shown in Figure 5-10. The sizes of the rail over the entire subdivision are also displayed. A general correlation exists between the 500 feet Yrel averages and the rail sizes. For example, the size of the rail between MP82 and MP104 is 141 lb per yard. The data from all three tests display a noticeable decrease in Yrel over these 22 miles. However, it is difficult to single out one factor's effect since the track performance is affected by many interconnected sources. Further theoretical studies and data analysis are needed to examine how Yrel data varies as the rail size changes.

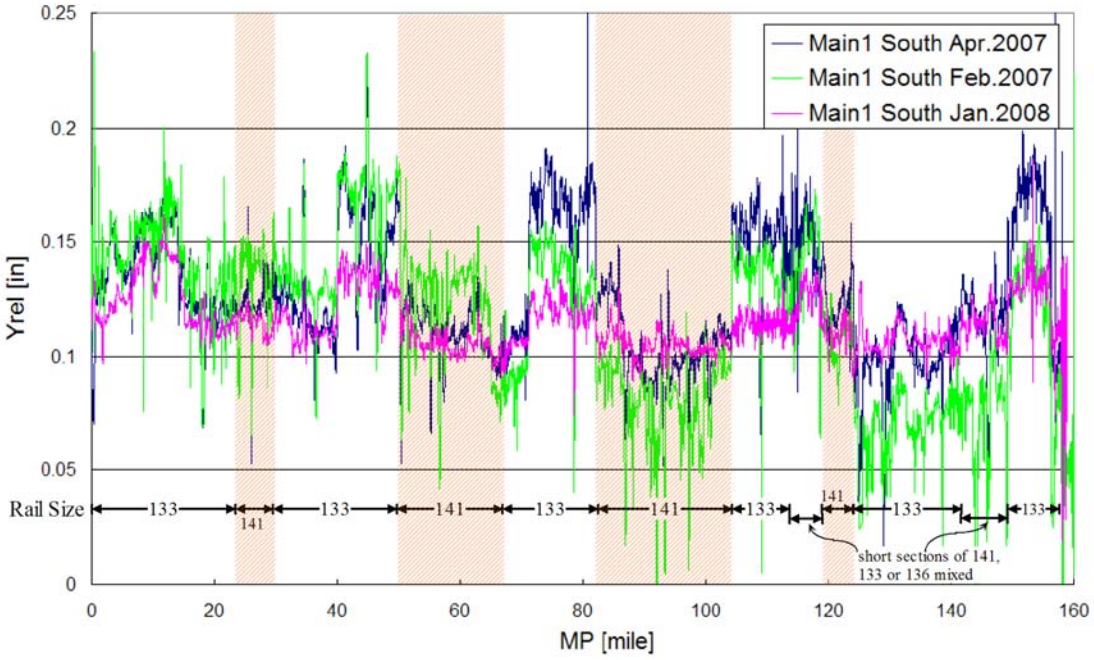

Figure 5-10: Average Yrel from Three Tests on Different Size Rail

5.4 Measurement Validation

A special validation test was conducted in October, 2008 on the UPRR's Yoder Subdivision between Cheyenne, WY, and Yoder, WY. The purpose of this validation test was to confirm the measurements collected by the system. Three methods were proposed and performed.

5.4.1 String Measurements

As described in section 3.1, Yrel is the distance from the rail surface under the camera to the wheel/rail contact plane. Therefore, the method depicted in Figure 5-11 to measure Yrel is very straightforward. Here, a string is pulled to pass the bottoms of the two wheels. Then the distance from the top surface of the rail under the camera to the string is the Yrel reading at this location.

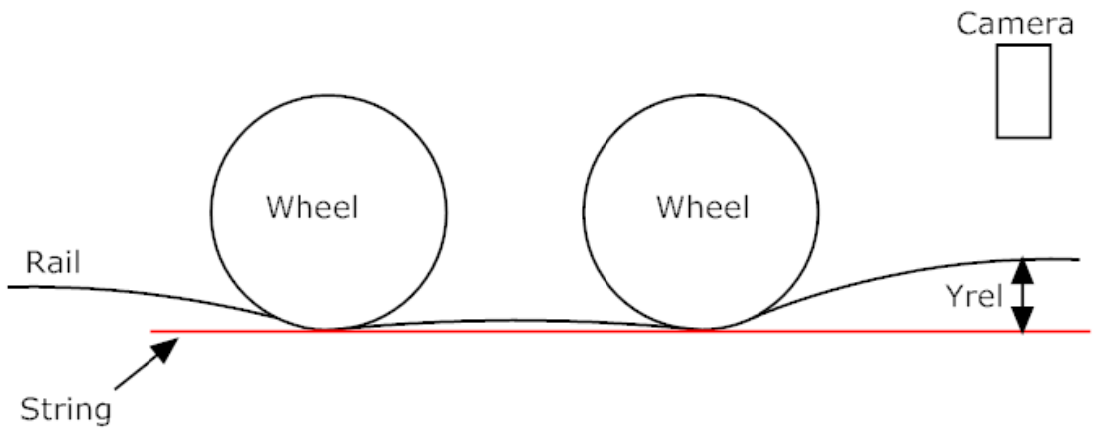

Figure 5-11: String Measurement Diagram

As shown in Figure 5-12, a specially made magnetic ruler is attached to the rail during the field measurement to make the reading process easier. The string is tightly held from the two ends as it barely touches the bottom of the two wheels. The distance from the top surface of the rail under the camera to the string is read to compare with the Yrel reading from the measurement system.

Figure 5-12: Field String Measurement

The string measurement was performed at three locations during the validation test. The measurement results and the Yrel measurements from the testing vehicle are listed in Table 5-1. The field string measurements and the Yrel measurements each differ by less than 0.1 inch.

Table 5-1: String Measurement and Yrel Measurement

Locations	Yrel (inch)	String Measurement (inch)	Difference (inch)
#1	1.000	1.004	0.004
#2	0.703	0.610	0.093
#3	0.703	0.669	0.004

The string measurements from these three locations closely matched the Yrel measurements from the testing vehicle, which suggests that the system's Yrel measurements are correct. However, this type of string measurement is not very accurate. A significant practical limitation is ensuring that the string perfectly passes the bottom of each of the two wheels – a rather difficult task. This limitation can easily contribute a relatively large error in the measurement results. To provide more accurate results, further methods are proposed and described in the following sections.

5.4.2 Survey Measurements

This method uses a surveyor's total station as shown in Figure 5-13 to independently measure the vertical deflection of the rail. Such instruments are commonly available with an indicated accuracy of less than one millimeter. In this scenario, rulers used as targets are attached to the side of the railhead by strong magnets as shown in Figure 5-13.

Figure 5-13: Instruments Used in Survey Measurements

Figure 5-14 demonstrates the measurement scenario. Thirteen rulers are placed every three feet on the side of the rail so that the total measurement range is 36 feet. This distance is usually enough to cover the entire deflection basin. First, the unloaded profile of the rail is measured by using the total station and a glass Porro prism commonly used in surveying. Next, the total station is used to measure the height of each ruler on the side of the rail while the rail is unloaded. After the measurements are recorded, the locomotive parks the measurement vehicle on this section of the track such that the inboard axle is directly on top of the center ruler as shown in Figure 5-14. The total station is then used to take the height measurement of each ruler a second time. The difference between the two height measurements for the same ruler is the rail deflection at that ruler's location. Adding the deflection measurement to the unloaded rail profile, the loaded rail profile can then be determined. Analyzing the resulting measurements would allow for the confirmation of the measured Yrel reading.

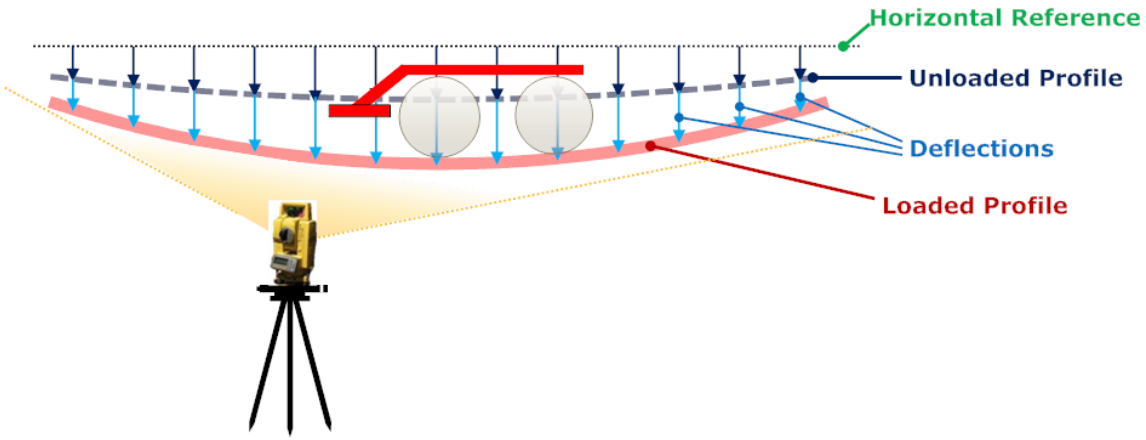

Figure 5-14: Measurement of Vertical Rail Position by Surveying

Survey measurements were conducted at two locations during the validation test. Measurement results from one of these locations are presented in Figure 5-15. The curve demonstrates the loaded profile of the rail with one wheel at position 0 and the other at a position of 70 inches since the distance between the two axles is 70 inches. The profile points at these two locations are connected with a line which is then extended by -48 inches in the horizontal direction because the horizontal distance between sensor head and inboard axle is 48 inches. As a result, the distance from the end of the line to the rail at position -48 inches is the Yrel measurement at this location. As shown in the figure, Yrel measures 0.732 inch at this location.

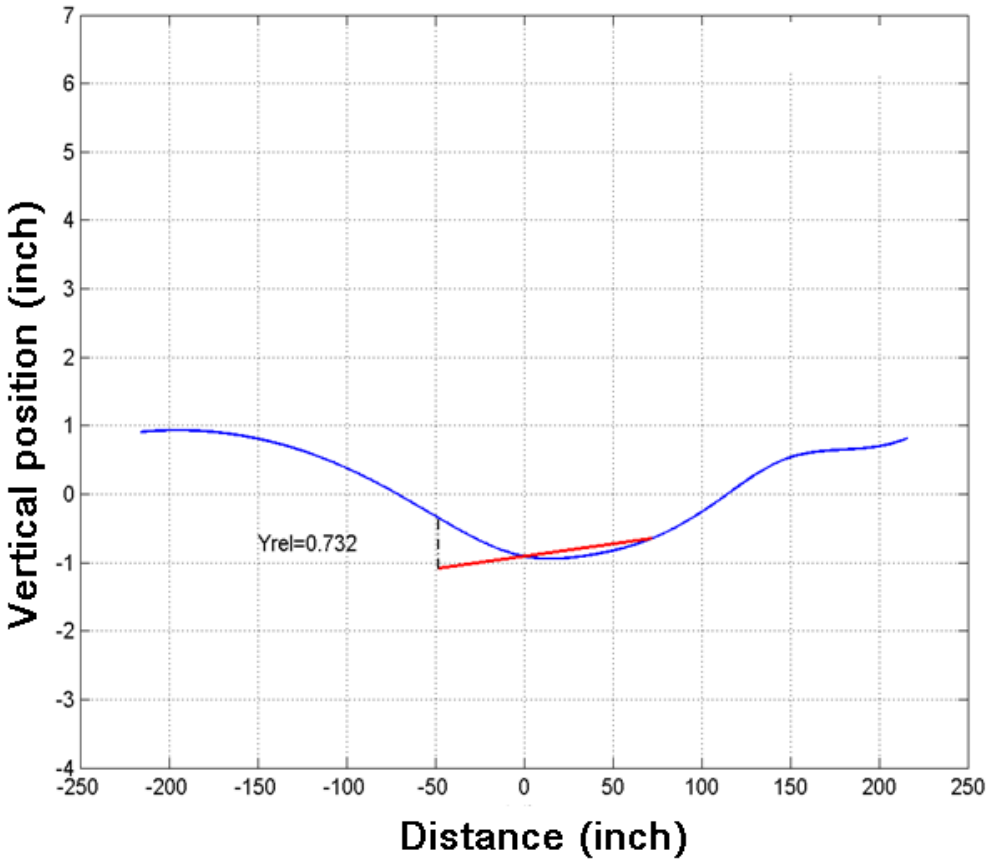

Figure 5-15: Survey Measurement Results

The testing vehicle's measurements are compared with the survey measurements from each site as shown in Table 5-2. The two methods produced almost identical results at both sites. This suggests that the testing vehicle's measurements are accurate and reliable.

Table 5-2: Comparison between System Measurement and Survey Measurement

	Yrel Measurement from testing vehicle (inch)	Yrel Measurement from surveying (inch)	Difference (inch)
Site A	0.738	0.732	0.006
Site B	0.150	0.150	0.000

5.4.3 Absolute Deflection Measurements by Cameras

Similar to the calibration procedure described in Section 4.3.3, a common camcorder is used to observe the vertical displacement of the rail as shown in Figure 5-16. A white magnetic strip is affixed to the rail to use as a target. The camera records the video of the white strip as the moving train passes the location. The video is then post processed to determine the vertical location of the strip over time. This process is much simpler than using LVDT's as described in Section 2.3 and will provide complete information on the passing train. A section of sampled deflection data processed from a video of a coal train is presented in Figure 5-17. In this section of data, a series of coal hoppers causes the rail to deflect about one half inch and three heavier locomotives at the end of the train to deflect the rail over 0.9 inches.

Figure 5-16: Wayside Camera Measurements Setup

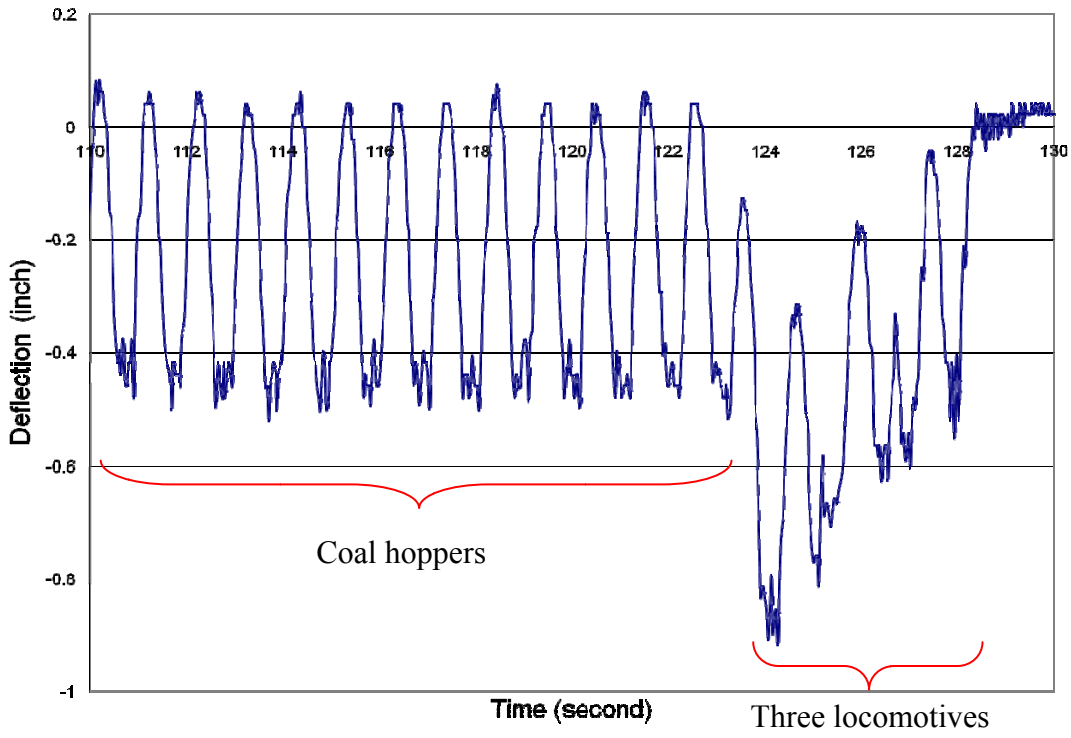

Figure 5-17: Sample Data of Absolute Deflection from Wayside Cameras

During the validation test, this type of absolute deflection measurement was conducted at three locations where survey measurements were also performed. The raw data of deflection over time from one of the locations is plotted in Figure 5-18. Here, the deflection caused by the locomotive, the test vehicle (UNLX002) and the geometry car are identified respectively. The maximum deflection of the rail caused by the test vehicle load occurred at point A, which is the moment when the axles pass by the position of the magnetic strip. The maximum absolute deflection was determined to be 1.1 inches for this location. Similar plots were made for the other two locations, and the absolute deflections were evaluated.

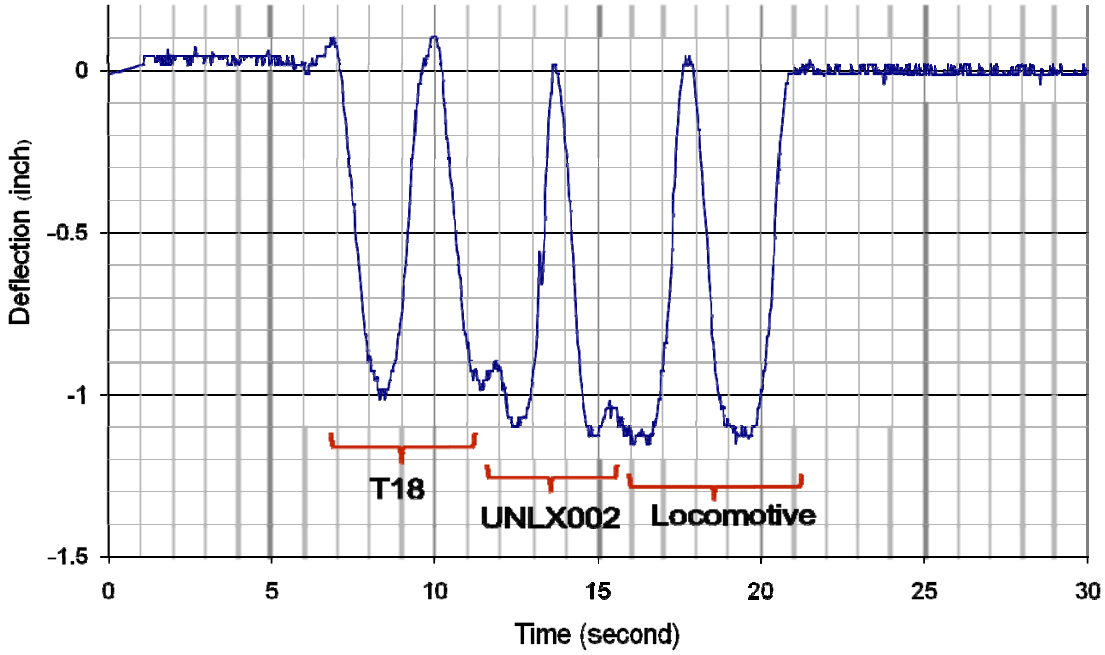

Figure 5-18: Deflection Data from Camera Measurement

Table 5-3 contains all of the deflection data from the surveying measurements and the camera video at the three locations. The three deflection measurements from the camera are very close to the corresponding ones from the surveying technique. The differences are less than 0.1" at each location, so the two types of measurements support one another.

Table 5-3: Comparison between Absolute Deflection Measurements from Surveying and Camera

	Deflection from surveying (inch)	Deflection from camera (inch)	Difference (inch)
Location #1	0.35	0.34	0.01
Location #2	1.14	1.1	0.04
Location #3	0.7	0.8	0.1

5.5 Trending Analysis

One focus of recent testing on the UP's South Morrill subdivision is on using trends in measurements made over time to better predict track performance and better schedule maintenance. It is hoped that this will ultimately lead to a reduction in derailments.

5.5.1 Data Pre-processing

Due to GPS misalignment, data from different tests may not exactly coincide with each other in terms of milepost. Figure 5-19 shows the two sets of data from the same section of track. An offset exists between the two curves.

Measurements from two tests over approximately 0.05 miles of track are shown in Figure 5-19. The figure clearly shows that the measurements from both tests have similar shape. However, the two sets of data have an obvious horizontal offset. The offset represents errors in the milepost location associated largely with GPS error in localizing the data. Despite errors in GPS measurement, the shape of the curve is maintained because the relative GPS measurement (one data point with respect to the next) is much more accurate than two independent absolute GPS measurements.

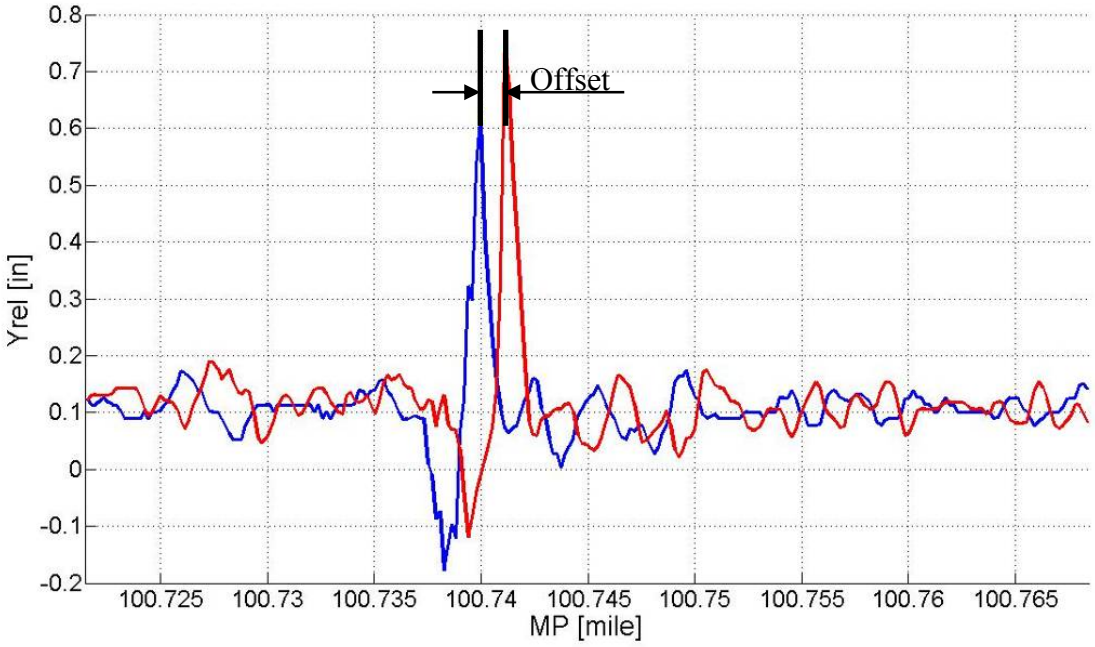

Figure 5-19: The Original Data from Two Tests

For the purpose of trending, it is desirable to remove the offsets so that relative comparisons can be made over short sections of track. The relative comparisons would evaluate one measurement relative to a previous measurement made at the same location at an earlier time.

To remove the offset in milepost, the cross correlation function is introduced to mathematically quantify the offset. Cross correlation is a standard method of estimating the degree of correlation between two sets of measurements. Consider two series *x(i)* and *y(i,),* both of length N, where *i*=0,1,2...N-1. The cross correlation, $\hat{R}_{xy}$, at delay *m* is defined as :

$$\hat{R}_{xy}(m) = \frac{1}{N}\sum_{n=0}^{N-1} x(n)y(n+m) \qquad \text{Equation 5-1}$$

where *m*=-(N-1),…,-2 -1,0,1,2,…,N-1

For various values of m, $\hat{R}_{xy}$ is in the range $-1 \le \hat{R}_{xy} \le 1$. The bounds indicate maximum correlation while 0 indicates no correlation. A high negative correlation indicates a high correlation but where one series is the inverse of the other series.

The results of applying the cross correlation function to the two series in Figure 5-19 at numerous values of m (between -100 and 100) is shown in Figure 5-20. This figure shows the cross correlation as a function of offsets. Clearly, the cross correlation reached a maximum when the offset was 8 feet. The value of the cross correlation at this offset is 0.8, indicating a high correlation between the data (this also suggests the measurements are highly repeatable).

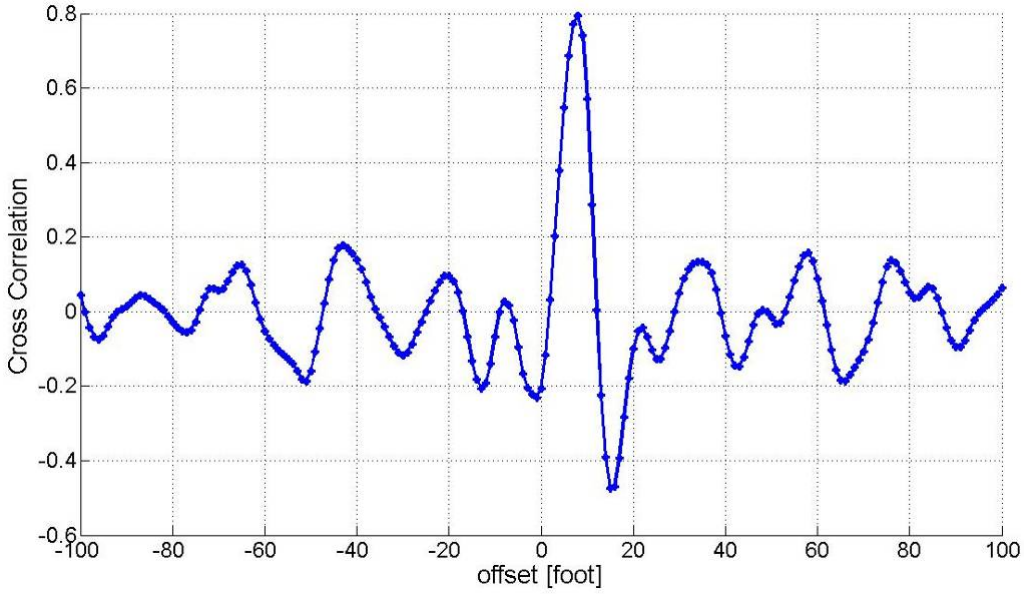

Figure 5-20: Cross Correlation

Based on the cross correlation plot, the second series in Figure 5-19 was shifted by 8 feet and the new plot is shown as Figure 5-21. Now the two series of data line up well, which is helpful and convenient for further data comparison and analysis.

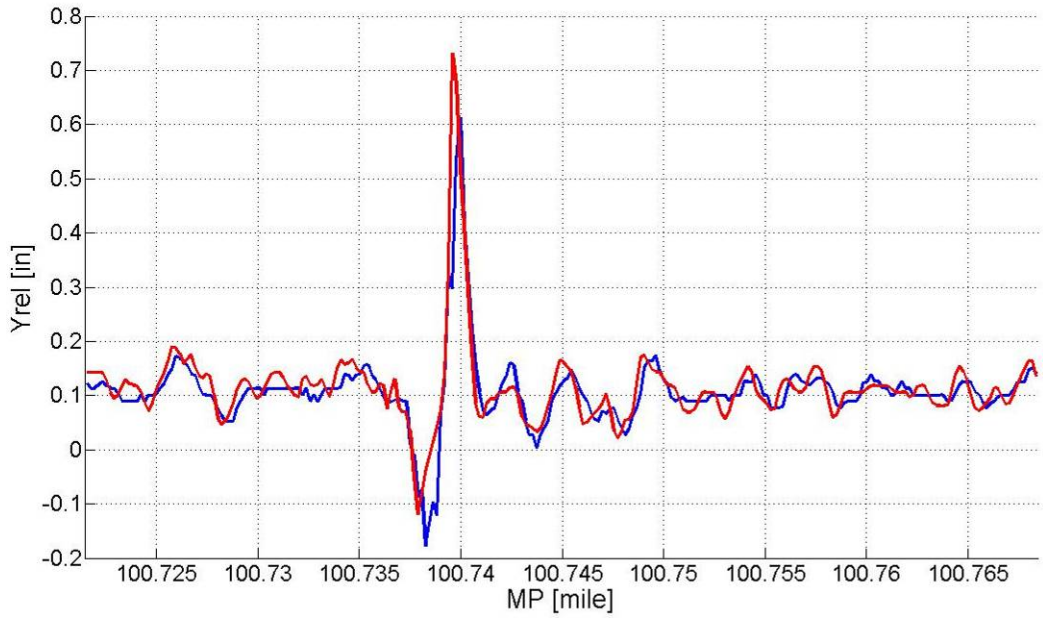

Figure 5-21: The Shifted Data from Two Tests

5.5.2 A Trending Example

Some trending results from the South Morrill subdivision are now presented. Several tests were conducted over the same approximately 160 miles of this sub-division at three-month intervals. Figure 5-22 shows the relative deflection measurement (*Yrel*) over 0.1 miles of track from MP A.70 to A.80 (exact mileposts are removed). Here the third axis (into the page) illustrates the time interval between the tests in months. Figure 5-22 clearly demonstrated the changes in this section of track as a function of time. Specifically, two locations are singled out over time. It can be seen that MP A.76 is not changing quickly over time while MP A.74 corresponds to a peak in the measurement (soft spot) that is increasing over time (becoming softer).

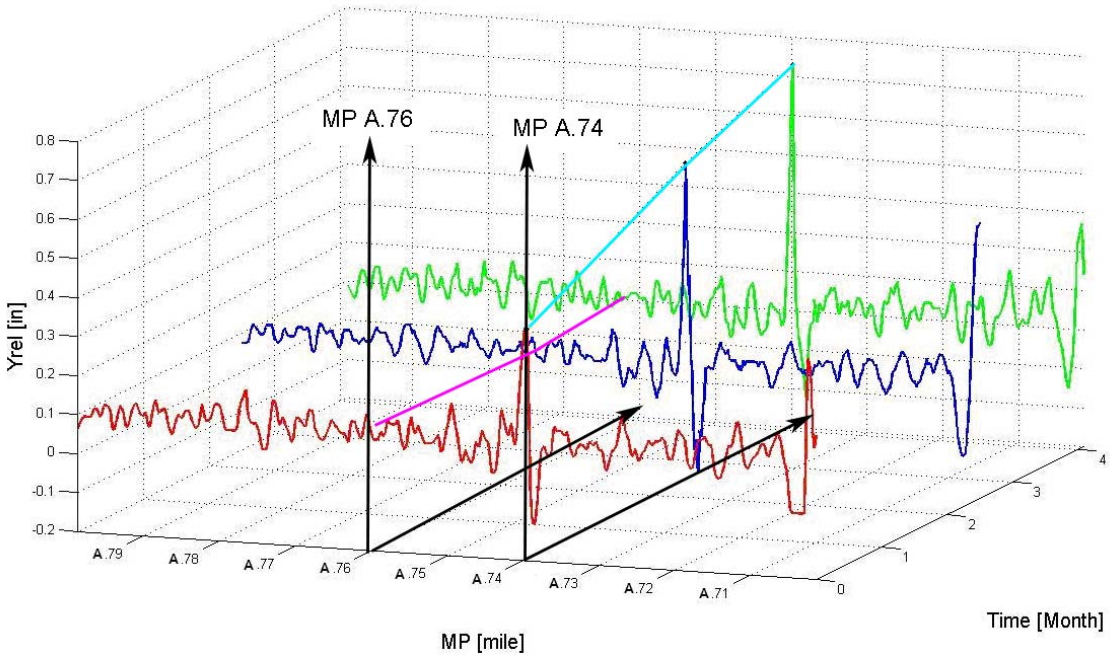

Figure 5-22: Data from 3 Tests at MP A.74

From the measurements shown in Figure 5-22, two sections at MP A.74 and A.76 are extracted as an example and shown as a function of time in Figure 5-23. Since three tests were performed, three data points are shown in each of the plots for these milepost locations. Given these data, a prediction can be made based on the trends. In this case a line is fitted to the data and used as the prediction. A correlation can be produced to indicate how well the line fits the three data points. Having only three points (three tests) of course may not accurately predict the trend, and clearly the prediction has uncertainty. More testing will improve the prediction. With more available tests it may be desirable to use other curves (rather than linear extrapolation) to improve the prediction.

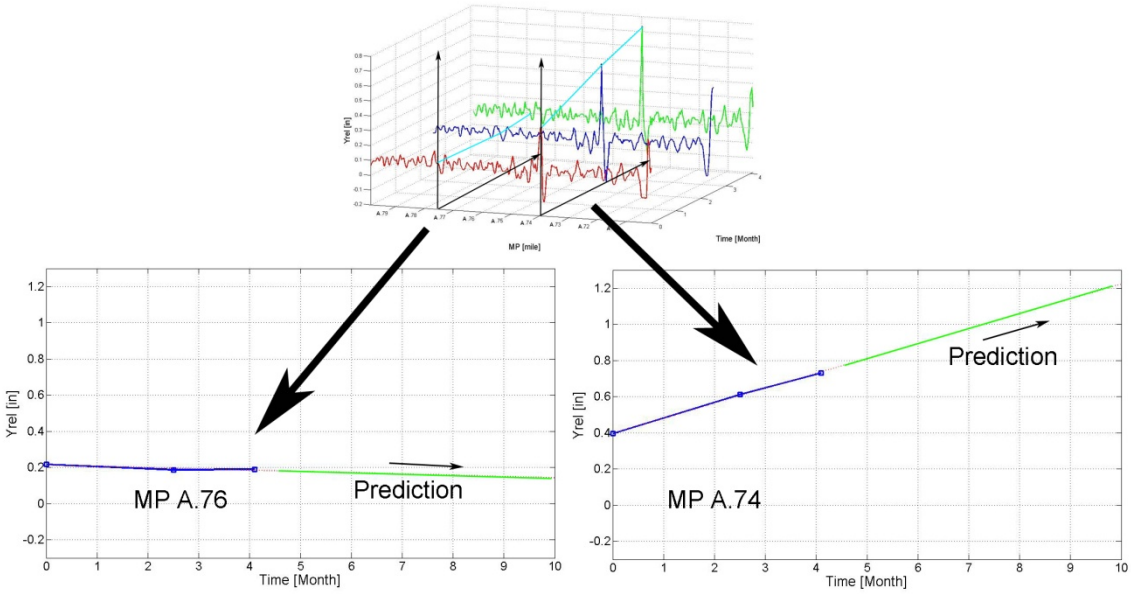

Figure 5-23: Trending at MP A.74 and A.76

To further illustrate the possible usefulness of this technique MP A.74 is shown again in Figure 5-24. Here an assumption is made that a given threshold of relative displacement, Yrel, would be undesirable. Based on previous measurements, a value of 1.2 inches is chosen and indicated by the red dashed line. Now, the linear prediction can be used to estimate the time required to reach this threshold. In this case, five and a half months from the last test is the window for maintenance. The accuracy of this prediction is difficult to quantify, however, this is a tool that can be used to prioritize maintenance based on actual track data. It is also possible to apply this technique to other track measurements such as gauge, gauge restraint, cross-level, and other standard measurements.

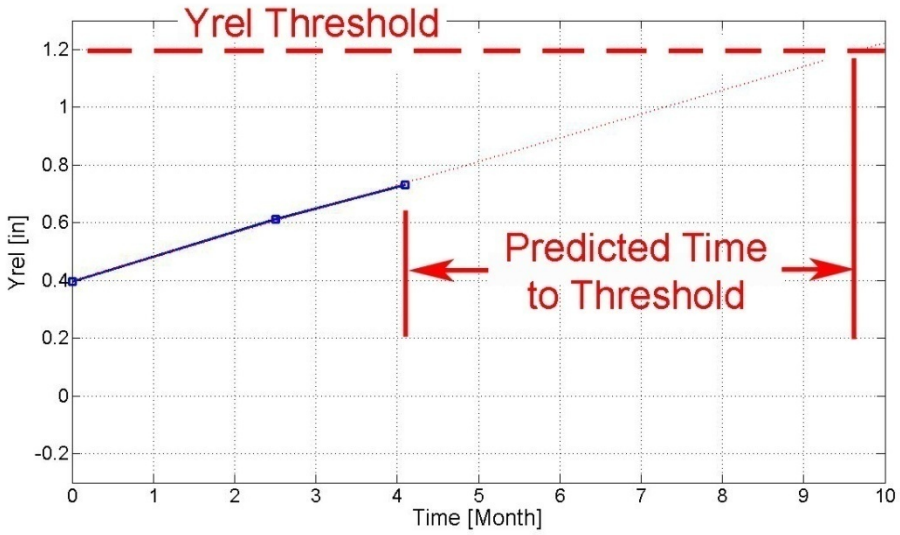

Figure 5-24: Test Data at MP A.74 as a Function of Time

The above approach can now be applied over the entire section of track between A.70 and A.80. This range is broken into 12 ft bin lengths and a curve fit is created for each bin. The Yrel measurements are shown in Figure 5-25 for the three tests. A subplot is created that represents the slope of the trending line (linear curve fit in Figure 5-24). Here the slope, given by $\frac{\Delta Yrel}{\Delta Time}$ in units of inches per month, is approximated as the difference between the two tests. When both differences are equal it represents a linear change over time. The figure shows that MP A.74 is changing approximately linearly over time at a relatively fast rate while the other part of the track in this section shows little change. The location of MP A.74 corresponds to a muddy road-crossing, and the needed maintenance schedule can now be estimated (given some amount of uncertainty).

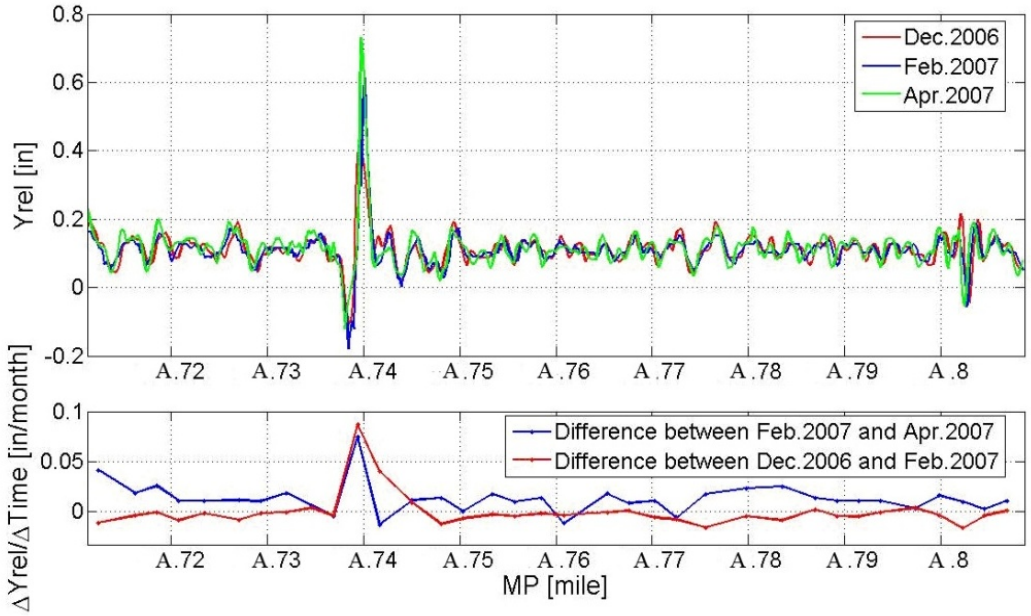

Figure 5-25: Trending from MP A.70 to A.74

5.5.3 Trending Results for Bridge Approaches

Data used in this section come from tests performed on the BNSF's Creston, St. Joseph, and Ravenna subdivisions. Tests were performed over two bridge approaches as shown in Figure 5-26 and Figure 5-27. The two soft approaches to the bridge corresponding to high Yrel can be identified in the figures. Both bridges are concrete ballast deck bridges. Trending from two tests on the bridge at MP B.6 is shown in Figure 5-26. An examination of the two measurements of Yrel indicates little change in the measurement. This is confirmed in the trending analysis where the rate of change was never more than 0.02 inch per month.

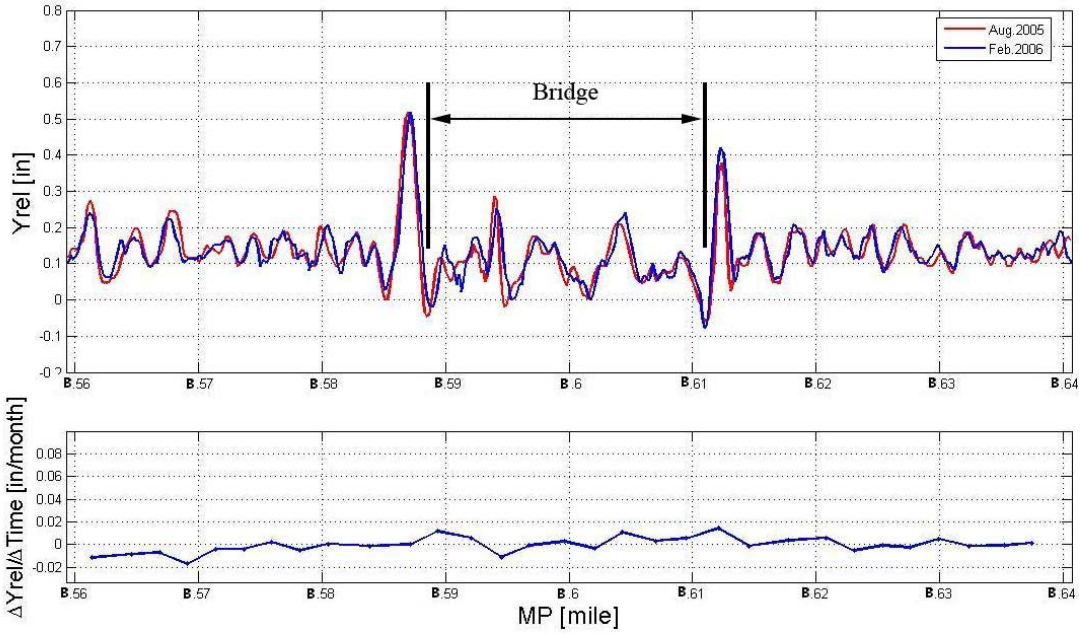

Figure 5-26: A Bridge at MP B.6

Trending for a second bridge near MP C.64 is shown in Figure 5-27. Here, three tests were performed, and again an examination of each of the Yrel measurements indicates little change in the measurement near the bridge. This is confirmed in the trending analysis. However, a few significant observations may be made. First, the difference between the June and February tests is consistently more substantial than the difference between the August and February tests. It could be speculated that more moisture was present in the track structure in June as compared to both February and August. Second, a significant change can be seen near MP C.60. Here the June test indicates both stiff and soft locations with large variations in Yrel as compared to the other tests. This is also clearly indicated in the trending results. It is suggested that such a "blip" in the trending might warrant further investigation by a track inspector.

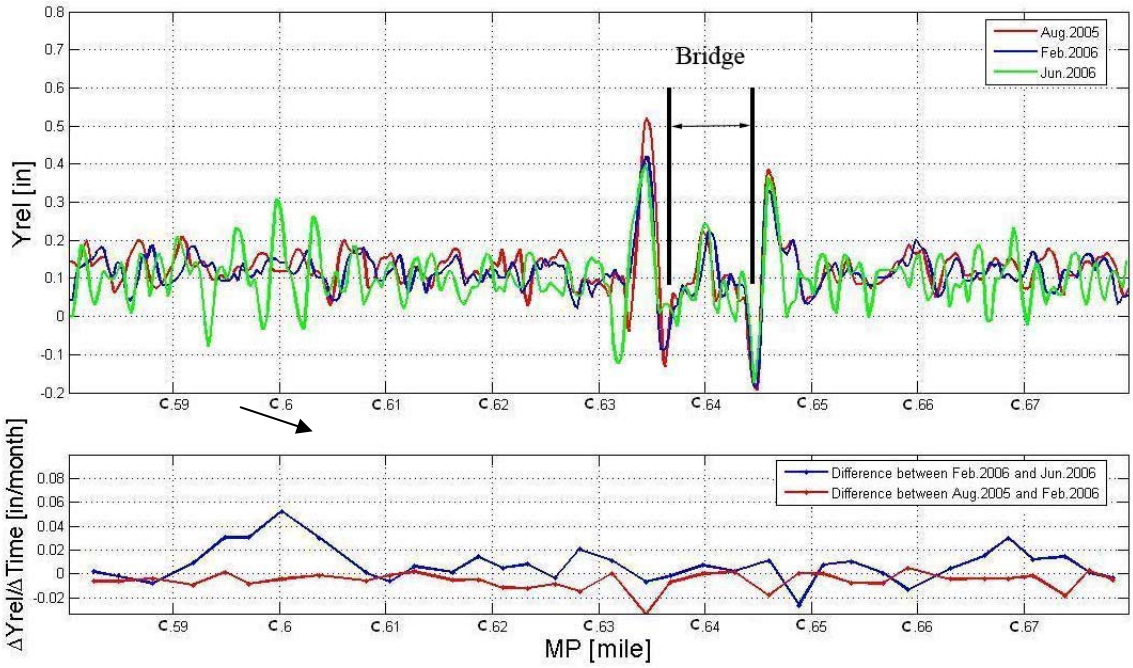

Figure 5-27: A Bridge at MP C.63

5.6 Implementation of Track Geometry Data

Based on the analysis in section 3.4.2, combining Yrel data and space curve data from the track geometry vehicle can provide information regarding vertical track displacement. In other words, using ECO data calculated from rail profile data, the element in Yrel contributed by the track geometry variation can be eliminated. ECO data is calculated by using the equations in section 3.4.1. Since Yrel data and ECO data come from two different measurement systems which have two separate GPS systems, an offset between the position readings from each GPS system is expected. As a result, an alignment algorithm is required for implementing geometry data into Yrel measurements.

The Yrel and ECO data were aligned by the same method used in the trending analysis, which included calculating the cross correlation between the two sets of data

and shifting the distance where maximum cross correlation occurs. The procedure is done by a program written in C++ and described in detail as follows.

The geometry data are measured in increments of one foot, however Yrel data is not. As a result, an interpolation is needed to transform Yrel data into one foot increments so that the cross correlation function can be applied to the two sets of data. This interpolation was done by the function "interp1" (one-dimensional data interpolation) in MATLAB. The method "pchip" (piecewise cubic Hermite interpolation) was used.

After the Yrel data is interpolated into one foot increments, it is then divided into sections of 300 ft. The length of 300 ft was chosen because it appeared to be able to create higher cross correlation for most of the sections.

Then, the GPS latitude and longitude data for each 300-ft section are used to extract the corresponding 300 ft of ECO data, as well as the 300 ft of ECO data before and after the corresponding 300 ft. Altogether, 900 ft of ECO data will be available for the next step of the procedure. For example, over the 300 feet (MP19.536 to MP19.478) shown in Figure 5-28, the GPS latitude and longitude for the starting data point (A) is given as 41.185069 -101.425016. The program searches through the ECO data and finds the point where the GPS is the closest to point A which is 41.185073 -101.4250164 (point B). Then, the 600 ft after point B and 300 ft before point B are extracted for the cross correlation calculation and data shifting.

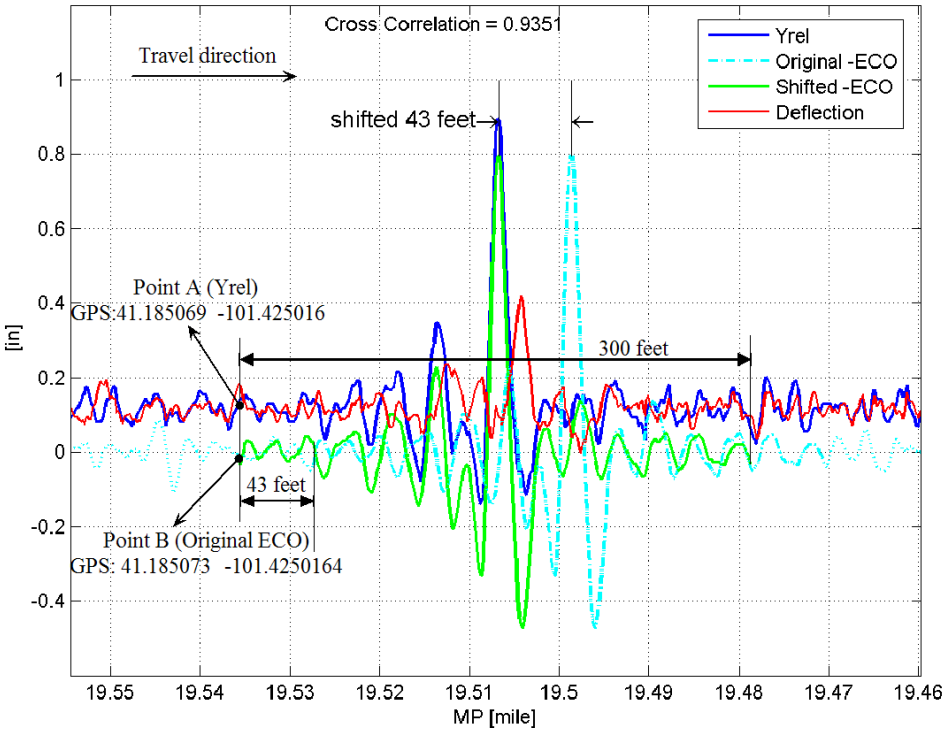

Figure 5-28: Data alignment for ECO and Yrel data

The next step is to calculate the cross correlation between the two series which include the 300 ft after point A in the Yrel data and the 300 ft after point B in the original ECO data. The program calls a subroutine to finish the calculation and return the cross correlation values as a function of m ($-150 \leq m \leq 150$).

Now the value of m corresponding to the maximum cross correlation value is determined. For the example data shown in Figure 5-28, the offset value was 43 ft and the maximum cross correlation was 0.9351 which indicates a very high correlation between the two data series. After the offset value is determined, the ECO data is simply shifted by this offset distance. For the section shown in Figure 5-28, the 300 data points from the original ECO data (from the 43rd point after point B to the 342nd point after B) are cut off to match the 300 ft of Yrel data. This process is then repeated for every 300 ft long section until all 158 miles of data are analyzed.

Finally, relative deflection values are simply calculated by subtracting "-ECO" from Yrel.

5.7 Exception Criteria

The Yrel data presents a multitude of information about the track condition but can be difficult to interpret. Therefore, a list of exception criteria is being propagated to automate and simplify the interpretation of such rail deflection and track modulus information. In this case, the exception criteria identify points of interest in the data.

5.7.1 Mathematical Formulation of Exception Criteria

The preliminary exception criteria are based on identifying distinct changes in the condition of the track. Changes are identified relative to a mean and standard deviation of the surrounding track. The mean may be calculated as:

$$\mu = \sum_{i=1}^{n} \frac{d_i}{n} \qquad \text{Equation 5-2}$$

Where μ is the mean, d_i is a single data point, and n is the number of data points over a characteristic length of track. Currently, 0.1 miles is used as the characteristic length.

Given the mean as calculated in Equation 5-2, the standard deviation can be determined by:

$$\sigma = \frac{\sum_{i=1}^{n} d_i - \mu}{(n-1)}$$ Equation 5-3

With these two definitions, several exception criteria may be generated. One standard criterion is to create a deviation ratio by computing the ratio (σ_{ratio}) of the current deviation with the standard deviation such as:

$$\sigma_{ratio} = \frac{d_i - \mu}{\sigma}$$ Equation 5-4

This is often used in industry as a quality control metric. For example, a given parameter should never vary beyond "six sigma". The difficulty with this metric in the evaluation of the relative deflection is that it can lead to false exceptions. For example, a smooth section of track such as the one in Figure 5-4, has a consistent mean and the standard deviation is very small (around 0.05"). As a result, any medium sized change (e.g. greater than 0.30") will create an exception when in reality this medium sized change in data does not represent a problem.

A more basic criterion is to compare the difference, given by Δ, between an individual data point and the mean as in:

$$\Delta = d_i - \mu$$ Equation 5-5

This criterion is straightforward and easy to apply.

5.7.2 Prioritized Exception Results

The above exception criteria may only capture a small percentage of the information contained in the relative displacement data. However, past tests suggest that they are useful in identifying track sections in need of maintenance.

A test was conducted on August 9, 2006 from Bill, WY to North Platte, NE. The test was performed on the Union Pacific Railroad's Powder River and South Morrill subdivisions. The line consisted of double track with approximately 250 MGT/year on main track No. 2 and 50 MGT/year on main track No. 1. The test was conducted in a special work train consist. Testing was done at speeds of up to 60 mph and the total test length was approximately 270 miles.

Table 5-4 shows the results of this test. Values for both the difference criteria exceptions, Δ, and the deviation ratio exceptions, σ_{ratio}, are shown. The sites are ranked in descending order of the Δ criterion over the entire 270 miles of the test (i.e. #1 having the largest value of Δ=1.424", #2 having the second highest value of Δ=0.989", and so on). Under this criterion, mile post A.47 was the "worst" section over the 270 miles of the test. Note that the exact mile post numbers were changed to letters so as not to identify specific sites of track.

Table 5-4: Prioritized Exceptions over 270 miles of Track

	MP	Track Feature	Δ	σ	μ	σ ratio
1	A.47	Signal	1.424	0.062	0.112	22.85
2	B.89	Turnout	0.989	0.065	0.142	15.12
3	C.97	Signal	0.973	0.100	0.121	9.72
4	D.65	Unknown	0.970	0.112	0.078	8.64
5	E.51	Turnout	0.919	0.122	0.099	7.56
6	F.95	Turnout	0.916	0.133	0.11	6.91
7	G.97	Unknown	0.828	0.127	0.129	6.53
8	H.30	9' CBC	0.815	0.115	0.097	7.10
9	I.17	Unknown	0.800	0.085	0.119	9.42
10	J.58	Turnout	0.796	0.083	0.118	9.56
11	K.43	Crossing	0.773	0.054	0.119	14.23
12	L.44	Crossing	0.753	0.120	0.098	6.30

Several observations may be made from this exception list. First, there is not an exact correlation between the difference criterion, Δ, and the deviation ratio criterion, σ_{ratio}. For example, site MP F.95 is the sixth highest when ranked by the difference criterion, but has a relatively small deviation ratio. This is a result of a large standard deviation surrounding the turnout (a rough turnout). Therefore, even though there is a large data reading at this site, the deviation ratio is relatively low (as compared to site K.43 for example).

5.7.3 Consequences of the Exception Criteria

Post processing of the data indicated a correlation with two of the top ten deflection locations and the location of two derailments. These were within 30 days of the track modulus measurement date.

The exception list was generated based on the Δ criterion and was independent of the knowledge of the derailments. The site with the second highest difference exception, MP B.89, coincided with the location of a defective field weld which caused an eight car derailment 14 days after the test. The site with the tenth highest exception at MP J.58 coincided with the location of a broken joint bar derailment 30 days after the test.

The site with the second highest Δ was mile post B.89. The raw data from that location are shown in Figure 5-29 for one mile of track. The exception at MP B.89 is clearly visible with a large peak in relative displacement. The standard deviation is also larger around this turnout. This large relative displacement suggested a problem with the joint 14 days before it caused a derailment.

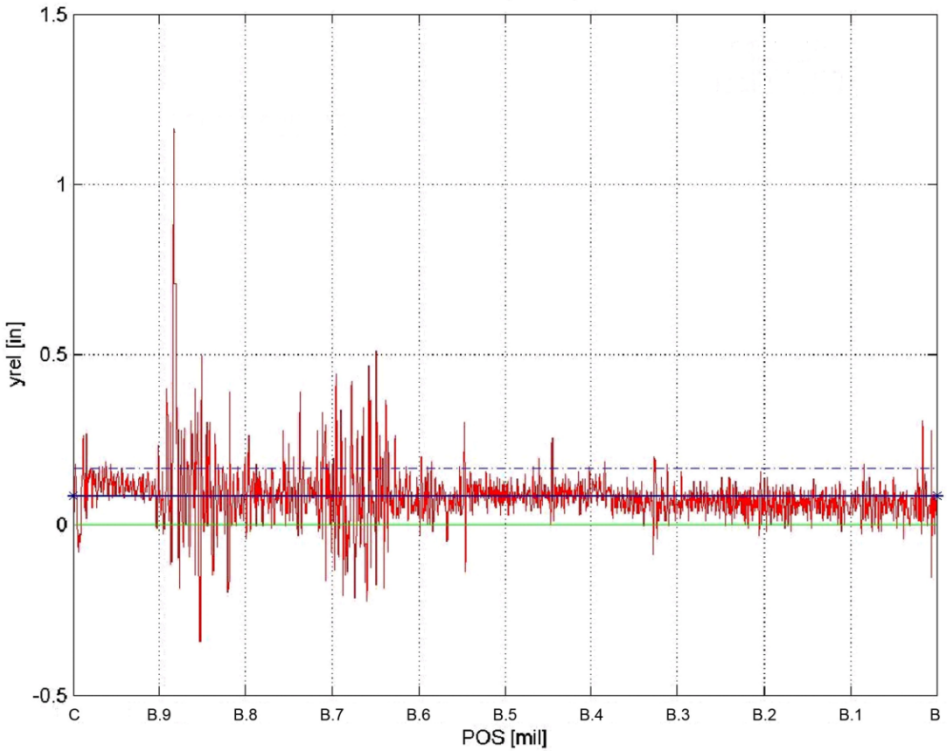

Figure 5-29: Site of Broken Field Weld 14 Days after Test

The site with the tenth highest Δ was at mile post J.58. The raw data from that location are shown in Figure 5-30 for one mile of track. The exception at MP J.58 is also visible with a large peak in Yrel measurements. The standard deviation is also larger around this turnout with both ends of the turnout clearly visible. The track failed 30 days after the data was collected. The assumption is that the low modulus continued to degrade, resulting in increasingly larger defections until failure of the non-insulated joint.

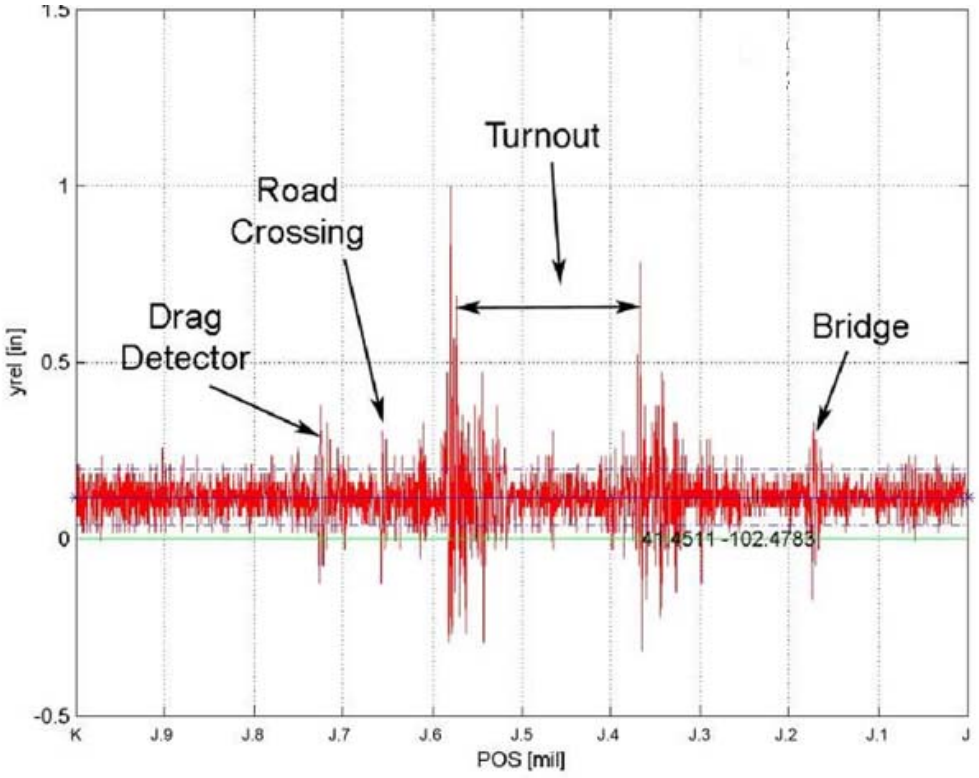

Figure 5-30: Failed Non-Insulated Joint 30 days post-test

5.7.4 Using "Yrel+ECO" as an Exception Criterion

Following the procedure described in section 5.6, the data from the vertical track deflection measurement system and track geometry car can be combined and the relative deflections ("Yrel+ECO") can be calculated. These "Yrel+ECO" results eliminate the

effects of track geometry variations and are more directly related to the track supporting foundation. Therefore, it is reasonable to consider "Yrel+ECO" as an exception criterion. "Yrel+ECO" is used as a major criterion to select locations for field investigations, and the subsequent visits suggest that this criterion is fairly useful in terms of identifying track support problems.

5.8 Comparison between Different Measurement Systems

5.8.1 Comparison of Vertical Track Deflection (VTD) with Vehicle-Track Interaction (VTI)

A track quality measurement system known as Vehicle Track Interaction (VTI) is currently in use by the Union Pacific Railroad. This system has been successfully integrated into revenue service. The VTI system uses accelerometers mounted on various locations of a railroad vehicle to measure vertical accelerations. The system is used on both locomotives and hopper cars and has been fully integrated into revenue service with sophisticated communication and data processing infrastructure.

Results presented here are from a test conducted on a locomotive that passed over the same section of track (the Powder River and South Morrill subdivisions) two days after the vertical rail deflection measurements presented in section 5.7.2 and 5.7.3. The relevant VTI results come from an accelerometer mounted to the axle of the locomotive (below the suspension system). The acceleration data are used (with knowledge of the locomotive's mass and suspension characteristics) to estimate loads between the wheel and rail.

The VTI measurements and the vertical deflection measurements are fundamentally different. For example, a smooth section of track with a low modulus will show no significant difference in VTI measurements as compared to a smooth section of high modulus track. However, this difference will be captured by the vertical track deflection system.

5.8.2 Comparison of Revenue Service Results from VTD and VTI

A test of the same section of track (270 miles of the Powder River and South Morrill subdivisions) was conducted using the VTI system on August 11, 2006 – two days after the VTD measurements were made. Some results of this test are shown in Table 5-5 as a comparison between the two measurements. Selections of the ranked results from VTI measurements are shown in the left four columns. The right two columns show how the same measurements appear in the Δ criterion exceptions from Table 5-4. Only the locations common to both tables are shown in Table 5-5.

Table 5-5: Prioritized Exceptions of VTI Data

VTI Rank	MP	Acceleration (g)	Estimated Axle Force (lb_f)	Δ (inch)	Rank of Δ
1	X.5	28.15	104,500	NA	NA
:	:	:	:	:	:
5	G.97	24.97	84,800	0.828	7
:	:	:	:	:	:
27	J.58	27.27	69,650	0.083	10
:	:	:	:	:	:
62	B.89	27.78	64,600	0.89	2
:	:	:	:	:	:
123	A.47	22.09	59,000	1.424	1
:	:	:	:	:	:
249	C.97	17.1	52,300	0.973	3

The most important conclusion to reach from Table 5-5 is that the two measurements are fundamentally different. The highest force estimated from the VTI data (at MP X.5) does not appear in the top twelve Δ criterion exceptions of Table 5-4. The top VTD exception (at MP A.47) appears at #123 in the VTI measurements. The two derailment locations described above appear on both lists (highlighted in both tables). The derailment that occurred 14 days after the vertical modulus measurements (MP B.89) appears as #2 on the VTD list and #62 on the VTI list. Similarly, the derailment that occurred 30 days after the test (MP J.58) was #10 on the VTD list and #27 on the VTI list. However, an enormous impact load at MP X.5 is not indicated in the top 12 of the VTD measurements. Clearly, these are different measurements.

5.8.3 Comparison of Revenue Service Results of Yrel and ECO

The relation between Yrel and ECO has been explained in section 3.4.2. Although high correlations exist between Yrel and ECO, they are fundamentally different measurements. Results from revenue service tests further confirm the fundamental differences.

A test was conducted in South Morrill subdivision in April, 2007. The VTD system and UPRR's track geometry car (EC5) collected data over the same 160 miles of track on the same day. Exception lists were produced based on Yrel measurements and calculated ECOs from the geometry car's space curve data.

Table 5-6 lists the top 20 locations in the VTD list along with their rankings in the ECO list. Among the three highlighted sites, #4 and #17 in the list are the locations where a derailment occurred one week before the testing day. The track was under construction at these locations on the day of the test. The #1 item in the list is the location where another derailment occurred two weeks before the test. Again, the track was under construction on the day of the test.

It can be observed that nine of the top 20 sites in the VTD list did not show up on the ECO list (ECO list includes 200 sites). Besides the derailment locations, only four locations (#5, #9, #18 and #20 in VTD list) were identified by both top 20 lists. In addition, these locations rank differently on each list.

Table 5-6: Comparison between VTD and ECO (Ranked by VTD)

VTD RANK	Δ (inches)	ECO RANK	ECO (inches)	MP	DESCRIPTION
1	1.18	1	1.1954	58.813	Derailment
2	1.13	N/A	N/A	11.802	Unknown
3	1.06	N/A	N/A	93.489	Signal
4	1.02	4	1.02	105.106	Derailment
5	0.94	7	1.0196	56.286	Road crossing
6	0.92	N/A	N/A	14.37	Signal
7	0.9	N/A	N/A	9.628	Unknown
8	0.88	93	0.625	55.307	Road crossing
9	0.87	28	0.8514	115.447	RR XING
10	0.86	12	1.0038	23.102	Signal
11	0.85	N/A	N/A	38.938	Signal
12	0.84	N/A	N/A	116.774	Unknown
13	0.83	N/A	N/A	147.589	Unknown
14	0.83	NA	N/A	31.294	Signal
15	0.8	43	0.7383	39.228	Road crossing
16	0.78	N/A	N/A	100.149	Switch
17	0.76	25	0.8672	105.152	Derailment
18	0.76	9	1.0157	19.508	Road crossing
19	0.75	33	0.793	24.594	Road crossing
20	0.75	3	1.172	53.56	Road crossing

A list ranked by ECO data was also produced as shown in Table 5-7. In this table, 18 of the top 20 locations in the ECO list were also in the VTD list (VTD list includes 90 sites). However, most of these locations have lower rankings in the VTD list. Except for the derailment locations and five unknowns, almost all of the top 20 locations in the ECO list are road crossings.

Table 5-7: Comparison between VTD and ECO (Ranked by ECO)

ECO RANK	ECO (inches)	VTD RANK	Δ(inches)	DESCRIPTION
1	1.1954	1	1.18	Derailment
2	1.1406	33	0.61	Road crossing
3	1.1172	20	0.75	Road crossing
4	1.0976	4	1.02	Derailment
5	1.0351	48	0.58	Crossover Switch
6	1.0312	72	0.52	Unknown
7	1.0196	5	0.94	Road crossing
8	1.0196	29	0.63	Culvert
9	1.0157	18	0.76	Road crossing
10	1.0156	22	0.7	Road crossing
11	1.004	82	0.51	Road crossing
12	1.0039	10	0.86	Road crossing
13	1.0001	81	0.51	Unknown
14	0.9961	46	0.58	Unknown
15	0.9687	56	0.55	Road crossing
16	0.9649	52	0.57	Road crossing
17	0.9414	59	0.55	Unknown
18	0.9336	N/A	N/A	Road crossing
19	0.9218	30	0.63	Unknown
20	0.8828	N/A	N/A	Road crossing

5.9 Field Investigations

The VTD measurement system conducted a test in a coal train consist at the South Morrill subdivision in June, 2008. About a month earlier, UPRR's EC5 geometry car collected track geometry data on the same subdivision. The track geometry data provided by UPRR was then integrated into the VTD's Yrel measurements so that Yrel and ECO measurements could be compared and relative deflection measurements could be calculated.

Based on both the VTD's Δ criterion and the calculated relative deflection measurements, 15 sites were selected and field investigations were completed on July 1st, 2008. The track visits identified the reasons for large Yrel and deflection measurements at all sites with varying levels of maintenance urgency. Among them, one site was taken out of service immediately and two additional sites were called for maintenance to be repaired. A variety of track problems were identified including poor joints, broken ties, muddy ballast, and crushed rail head, etc. Some of the sites will be discussed in detail in the following sections. The actual mileposts for these sites are concealed in the discussions.

5.9.1 Site 1: A Crushed Rail Head

The data from the first site is plotted in Figure 5-31. The peak in the Yrel data on the north rail measures 0.89" while the ECO measurement is 0.34". As a result, the relative deflection is calculated as 0.55".

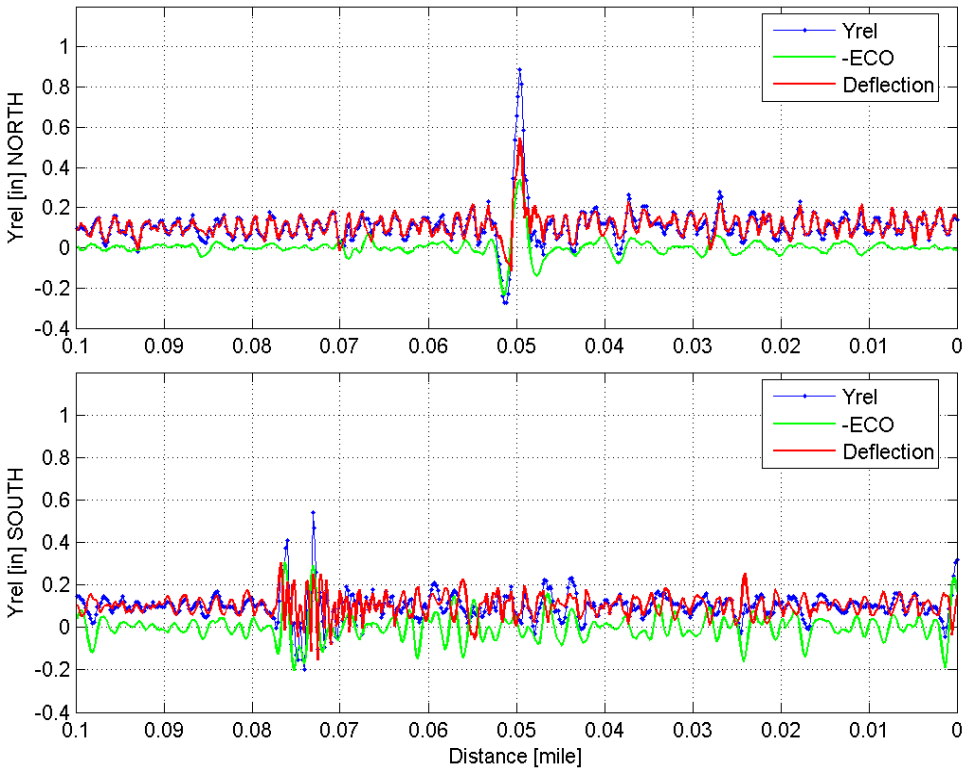

Figure 5-31: Data at the Crushed Rail Head Site

The pictures of this location are displayed in Figure 5-32. The white-colored ballast indicates that strong pumping has occurred. The track inspector estimated the pumping to be up to three quarters of an inch. The rail profile dropped down half an inch at the crushed spot. This site was investigated two weeks after the test. The track inspector suggested that the weather was damp and a flash flood warning was issued around the testing time, so that the deflection was expected to be large.

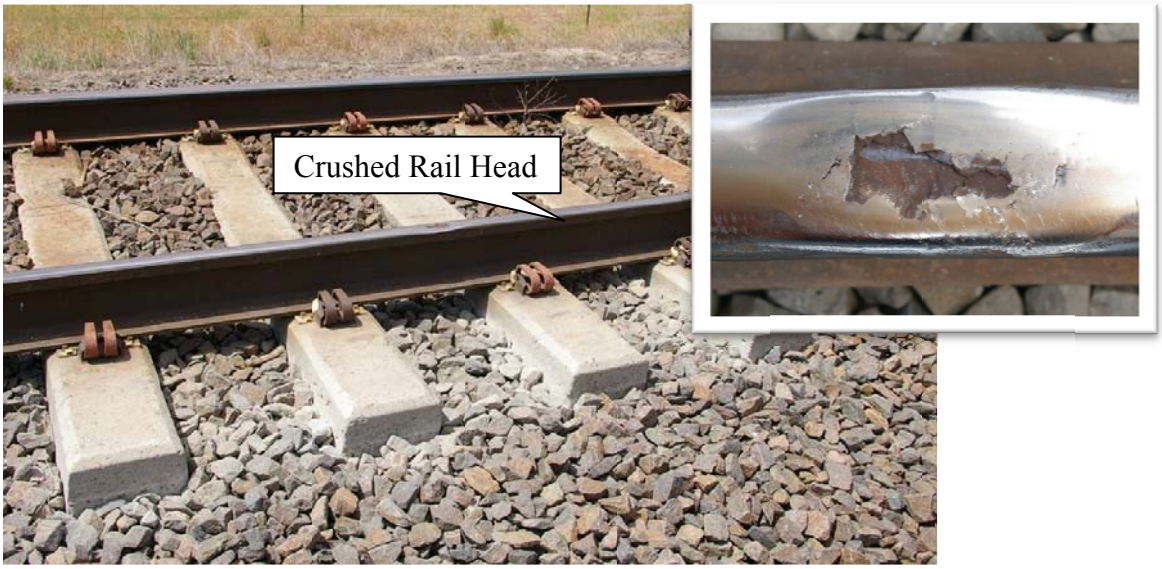

Figure 5-32: A Crushed Rail Head

5.9.2 Site 2: A Muddy Crossing

A number of road crossings are listed in the VTD exceptions list. Most of them exhibited fouled ballast and broken ties. Data from one particular site are shown in Figure 5-33. On the south and north rails, two peaks of Yrel data may be observed. They represent the two approaches to the road crossing. The approach at the east side of the crossing appears to be much worse than the west side based on the Yrel data. The deflections at both rails on the east approach are almost 0.6".

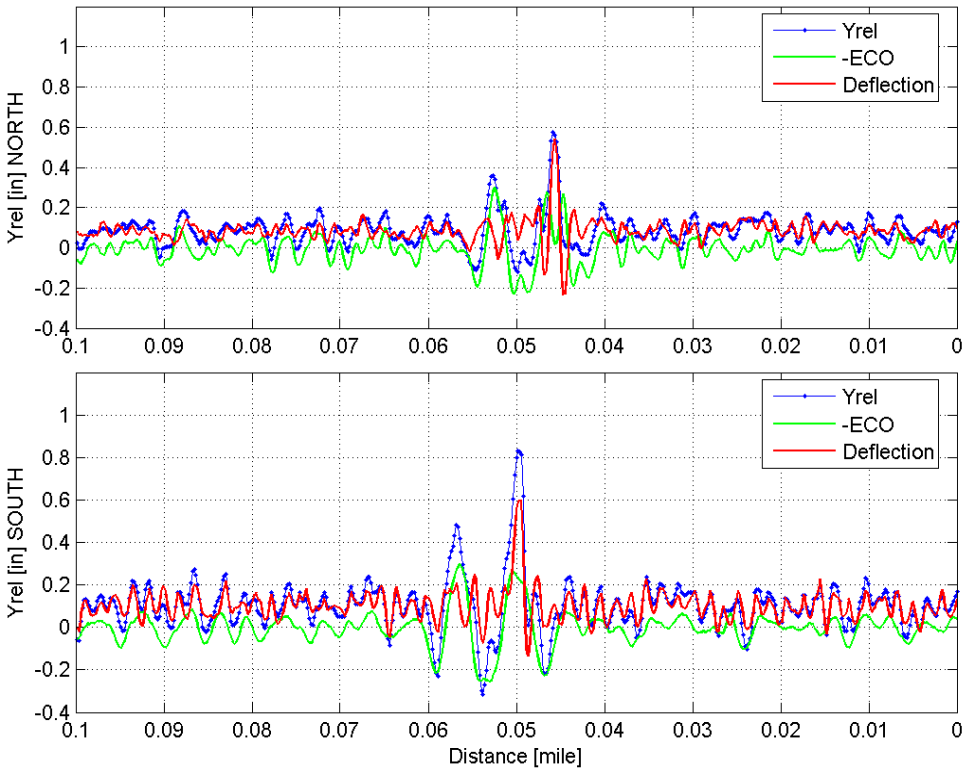

Figure 5-33: Data at the Muddy Crossing Site

At least four ties were center cracked and some of them appeared to have horizontal cracks at the bottom. The muddy ballast and the tie cavities indicated large movements of the ties. Based on observation, the ties were estimated to have moved by over 0.5". This muddy area was located at an approach to a road crossing. The other side of the road crossing was also muddy. This explains the two peaks in the Yrel data. Again, the track was much wetter on the day of the test.

Figure 5-34: The Muddy Crossing

5.9.3 Site 3: A Failing Joint

Approximately half of the sites in the VTD exception list are joints. The measurement system demonstrated a notable ability to identify bad joints. Figure 5-35 shows the data at one particular joint. In this case, Yrel measured 1.21” at the joint with an ECO reading of only 0.3”. Therefore, the deflection is over 0.8”.

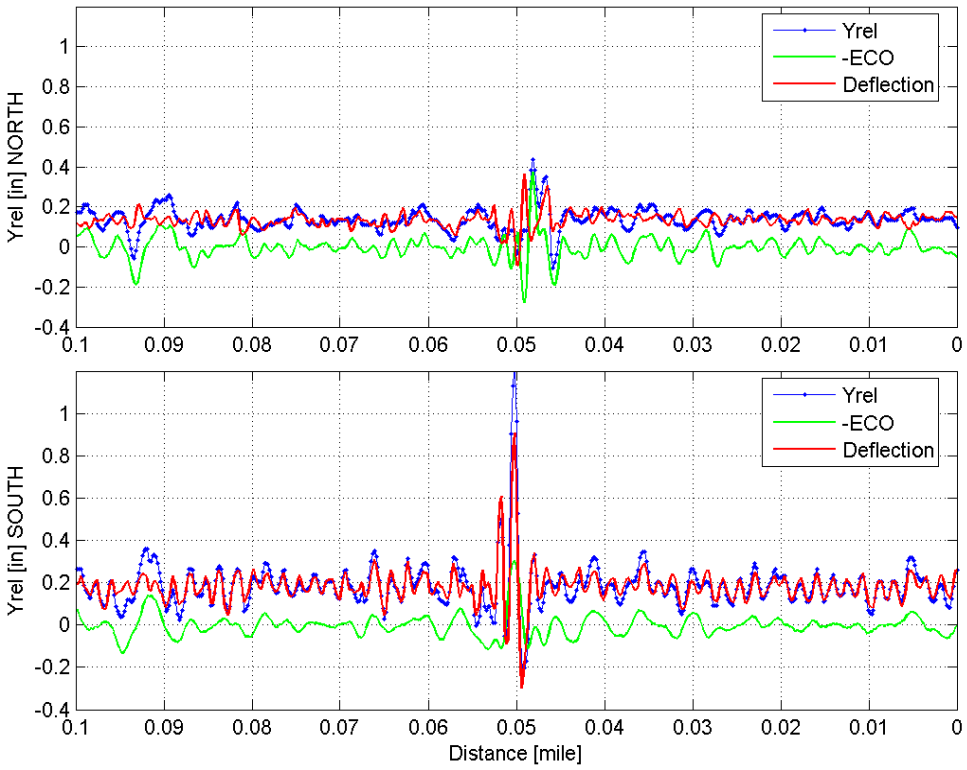

Figure 5-35: Data at the Failing Joint Site

Figure 5-36 shows the condition of the insulated joint. This supported joint is rare in North America where suspended joints are dominant. The supporting tie in the center was in a very poor condition. The tie was split and a large portion (left part in the picture) was nearly separated from the rest of the tie. Applying pressure with a foot was enough to deflect the tie. The bolts on the joint bars were loose and one of them would actually rotate as a train passed. The track inspector commented that this joint was probably among the worst 10% of all joints. A wayside camera measurement was taken as a coal train passed the site. The video showed that the deflection at the joint was over 1.2 inches under the loads of the locomotives.

Figure 5-36: The Failing Insulated Joint

5.9.4 Site 4: A Series of Broken Ties

The peak in the Yrel data from this site reads 0.95” while the ECO is 0.41”. The site is located on a portion of tangent track with no joints or crossings. Field measurements of the MCO (mid-chord offset) were consistent with the geometry car measurements. As shown in Figure 5-37 the curve of Yrel data from this site has a special shape when compared to the data from other sites. Unlike the sharp peaks in Figure 5-35, the peak here is broader and high deflections occurred over a relatively long distance.

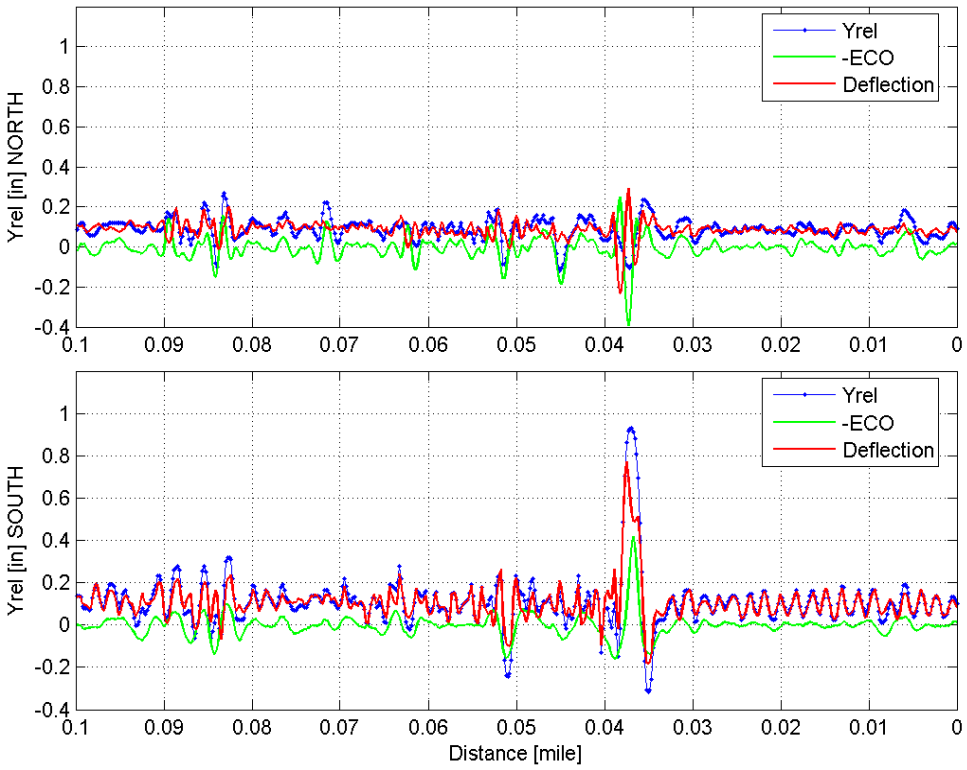

Figure 5-37: Data at the Broken Ties Site

A picture of this site is displayed in Figure 5-38 in which a series of broken ties are clearly visible. The ties barely constrained the south rail. The clips were either missing or unattached to the rail due to the cracks in the ties. The broken parts of the ties could easily be lifted by hand. Recent geometry car tests and VTI tests did not identify an exception at this location. The track inspector explained that defects like these were difficult for track inspectors to notice. The track director immediately stopped service on the track as shown in Figure 5-39.

Figure 5-38: Six Broken Ties in a Row

Figure 5-39: Track Taken Out of Service

5.10 Modulus Estimation

An important goal of the project is to obtain the track modulus information using the system's measurements. The relation between Yrel and track modulus based on the Winkler model was discussed in Section 3.2. The track modulus determined by this relation is an overall effective modulus. The method does not distinguish between voids, poor ballast, soft subgrade, or broken rail components.

Using Equation 3-10 and Figure 3-5, the Yrel measurement can be converted into track modulus. As mentioned earlier, Equation 3-10 is based on the analysis which neglects track geometry variations. The discussions in Section 3.3 explained how using "Yrel+ECO" would eliminate the effect of track geometry variations. Therefore, by using the calculated relative deflection ("Yrel+ECO") as Yrel in Equation 3-10, the modulus measurement can be determined without the effects of track geometry.

The previous results may be implemented in further analysis of site four. The Yrel and ECO data from the south rail of this site as shown in Figure 5-37 were converted into track modulus. The calculated modulus over the same section of track shown in Figure 5-37 is plotted in Figure 5-40. An extremely soft supporting foundation is indicated since the modulus value drops from around 3,000 psi to a mere 200 psi.

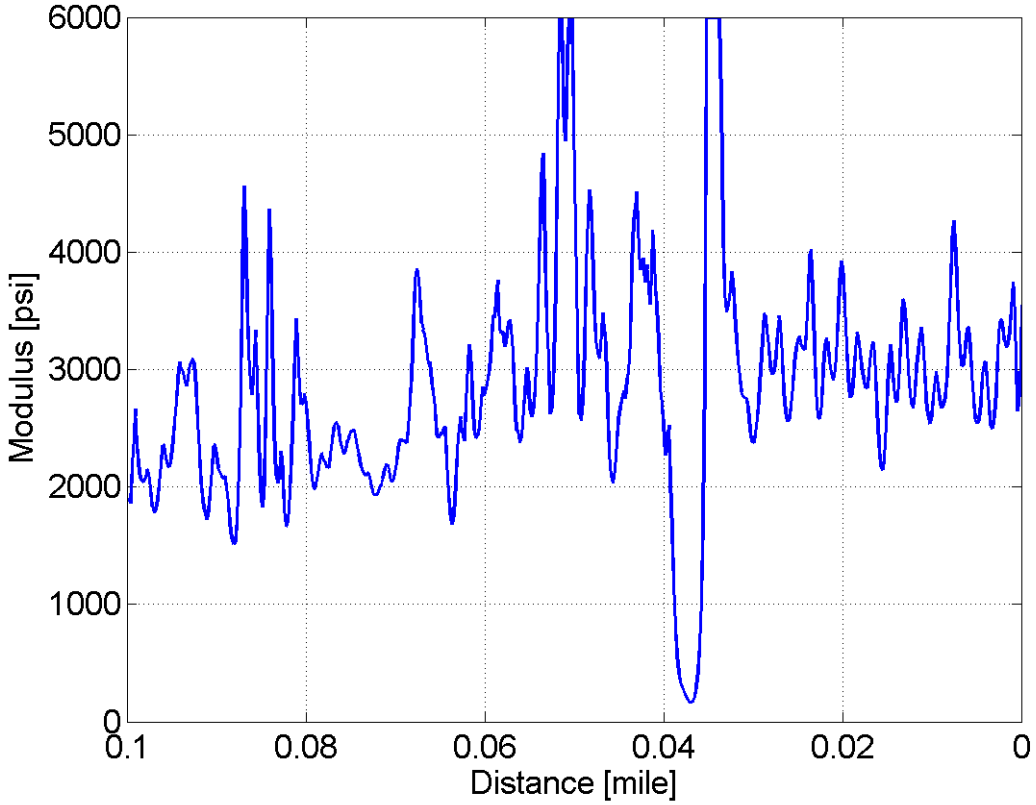

Figure 5-40: Track Modulus Calculated from Relative Deflection Data

6 CONCLUSION

Track modulus is important because it significantly affects track performance and maintenance requirements. Currently there is no vehicle available to measure track modulus and track deflection at revenue speeds in real-time.

A system has been developed to make real-time vertical track deflection measurements from a moving railcar. The deflection measurement can be used to estimate track modulus based on mathematical models describing the relation between loads and track deformation. The system consists of a loaded hopper car outfitted with a camera/laser sensor system to detect the vertical deflection of the rail relative to the wheel/rail contact point. In order to eliminate the effect of track geometry variations, track geometry car data is introduced into the system.

All of the components of the measurement system have been described in detail. The methods and procedures of image processing and calibration were illustrated. The potential errors in the measurements were also analyzed, showing that the system can provide fairly accurate and reliable measurements. Further improvements included upgrading the sampling rate of the measurement system.

The measurement system has conducted revenue service tests over three thousand miles of track. A special validation test was also performed. Based on the results from these tests, a variety of analyses were conducted. The system's measurements demonstrated high repeatability. The influences of various testing conditions (testing speed, testing seasons, rail size) on the testing results were also evaluated. Three validation approaches have been developed, and results from the validation test confirm

that the system measures accurate outputs. Trends in the data from different tests were examined to better monitor the changes in the track quality. Exception criteria were proposed and used to identify and prioritize track locations in need of maintenance. These criteria proved to be valid, although further improvements are still possible. The data from different systems (VTD and VTI, VTD and ECO) were then compared, and the results showed that the VTD system provides unique and valuable information that is not available from the other systems. Furthermore, the VTD system has notable ability to indicate track support problems. Last but not least, the process of using the system's measurements to estimate track modulus was demonstrated.

7 APPENDIX Program Flowchart

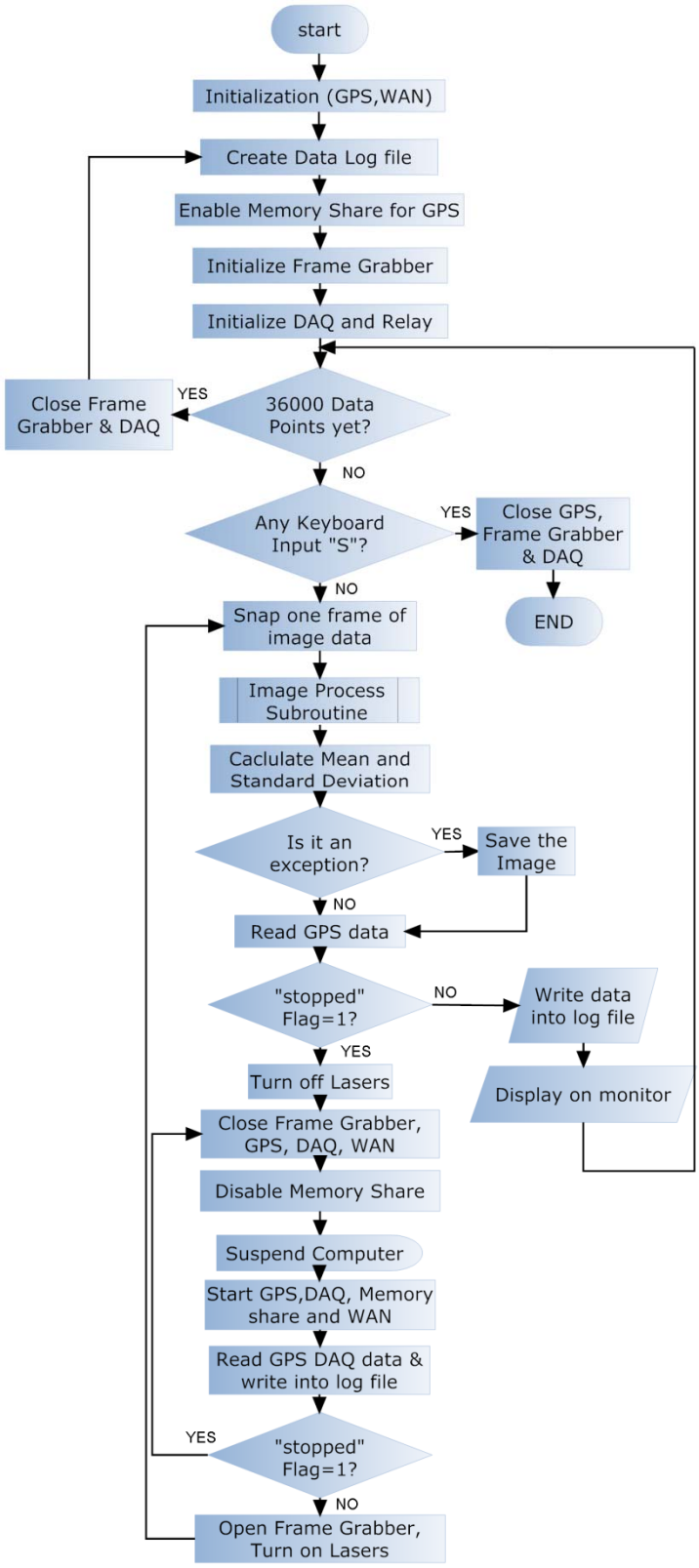

8 REFERENCES

AREMA Manual, 1996, Chapter 16, 10.2.2,5

Arnold, R., Lu, S., Hogan, C., Farritor, S., Fateh, M., El-Sibaie, M., "Measurement of Vertical Track Modulus From a Moving Railcar," *Proceedings of the AREMA 2006 Annual Conference*, Louisville, KY, September, 2006.

Beckwith, T. G., Marangoni, R. D., and Lienhard V, J. H., 1993, *Mechanical Measurements 5th Edition*, Addison-Wesley Publishing Company, Inc. Reading, MA: pp. 464-469.

Boresi, Arthur P. and Schmidt, Richard J. 2003. *Advanced Mechanics of Materials, 6th Edition.* John Wiley & Sons, New York, NY: Chap. 5, 10.

Cai, Z., Raymond, G. P., and Bathurst, R. J., 1994, "Estimate of Static Track Modulus Using Elastic Foundation Models," *Transportation Research Record* 1470, pp. 65-72.

Carr, Gary A, 1999, "Dynamic Response of Railroad Track Induced by High Speed Trains and Vertical Stiffness Transitions With Proposed Method of Measurement", Master Thesis, Tufts University. September 1999.

Carr, Gary A. and Greif, Robert, 2000. "Vertical Dynamic Response of Railroad Track Induced by High Speed Trains," *Proc. of the ASME/IEEE Rail Joint Conference*, pp. 135-151.

Chang, C. S., Adegoke, C. W., and Selig, E. T., 1980, "GEOTRACK Model for Railroad Track Performance," Journal Of the Geotechnical Engineering Division, *Proc. Of the American Society of Civil Engineers*, November 1980, Vol. 106, No. GT11, pp 1201-1218.

Hogan, C., Dick, M., Lu, S., Farritor, S., Arnold, R., GeMeiner, W., Clark, D., "Track Stiffness Measurement with Implementation to Rail/Vehicle Dynamic Simulation," *Proceedings of the AREMA 2008 Annual Conference*, Salt Lake City, UT, September, 2008.

Hogan, C., Design of a System to Measure Vertical Railroad Track Deflection From a Moving Railcar and Implementation to Dynamic Railcar Simulation, Master Thesis, University of Nebraska-Lincoln, August, 2007.

Craig, J. J., 1989, *Introduction to Robotics: Mechanics and Control, 2nd Edition*, Addison-Wesley Publishing Company, Inc., Reading, MA: pp 19-60 .

Davis, D. D., Otter, D., Li, D., and Singh, S., December 2003, "Bridge Approach Performance in Revenue Service," *Railway Track & Structures*, pp. 18-20.

Ebersohn, W., and Selig, E. T., 1994, "Track Modulus on a Heavy Haul Line," *Transportation Research Record* 1470, pp. 73-83.

Ebersohn, W., Trevizo, M. C., and Selig, E. T., 1993, "Effect of Low Track Modulus on Track Performance," International Heavy Haul Association, *Proc. Of Fifth International Heavy Haul Conference*, pp. 379-388.

Federal Railroad Administration, March 2001, "T-16: FRA's High Speed Research Car," *Research Results*, RR01-01.

Heelis, M. E., Collop, A. C., Chapman, D. N. and Krylov, V., 1999, "Predicting and measuring vertical track displacements on soft subgrades," *Railway Engineering*. 117

Kerr, Arnold D. "A Method for Determining The Track Modulus Using A Locomotive Or Car On Multi-Axle Trucks," *Proceedings American Railway Engineering Association*, 1983, Vol. 84, pp 269-286.

Kerr, Arnold D. "On the Stress Analysis of Rails and Ties," *Proceedings of American Railway Engineering Association*, 1976, Vol. 78, pp 19-43.

Kerr, A. D. and Shenton, H. W., "On The Reduced Area Method For Calculating The Vertical Track Modulus," *American Railway Engineering Association Bulletin*, December 1985, Vol. 86, No. 703, pp 416-429.

Kierzenka J. and Shampine L. F., 2001, "A BVP Solver based on Residual Control and the MATLAB PSE," *ACM TOMS*, Vol. 27, No. 3, pp. 299-316.

Li, Dingqing, Hass, Kevin, and Meddah, Abe, June 2002, "Moving closer to performance-based track geometry inspection," *Railway Track and Structures*, pp. 15-17.

Li, Dingqing, and Selig, Ernest T., 1994, "Resilient Modulus for Fine-Grained Subgrade Soils," *Journal of Geotechnical Engineering*, Vol. 120, No. 6, pp 939-957.

Li, Dingqing, and Selig, Ernest T., 1998, "Method for Railroad Track Foundation Design I: Development*," Journal of Geotechnical And Geoenvironmental Engineering*, Vol. 68, No. 7-8, pp 457-470.

Li, Dingqing, Thompson, Randy, and Yoshino, Dio, 2003, “Evaluation of track-gauge-strength degradation in revenue service,” *Railway Track and Structures*, pp. 19-21.

Lu, S., Arnold, R., Farritor, S., "On The Relationship Between Load and Deflection in Railroad Track Structure," *Proceedings of the AREMA 2008 Annual Conference*, Salt Lake City, UT, September, 2008.

Lu, S., Farritor, S., Arnold, R., GeMeiner, W., Clark, D., Al-Nazer, L., Carr, G., El-Sibaie, M., "Measurement of Vertical Track Modulus - Field Testing, Repeatability, and Effects of Track Geometry," *Proceedings of the 2008 Joint Rail Conference*, Wilmington, DE, April 22-24, 2008.

Lu, S., Hogan, C., Minert, B., Arnold, R., Farritor, S., Seeger, W., Oliver, M., Lees, H., Thornton, D., Fateh, M., Carr, G., "Vertical Track Modulus Testing On BNSFs Heavy Haul Coal Line," *Proceedings of the AREMA 2007 Annual Conference*, Chicago, IL, September, 2007.

Lu, S., Hogan, C., Minert, B., Arnold, R., Farritor, S., GeMeiner, W., Clark, D., "Exception Criteria in Vertical Track Deflection and Modulus," *Proceeding of 2007 ASME/IEEE Joint Rail Conference & Internal Combustion Engine Spring Technical Conference*, Pueblo, CO, March 13-16, 2007.

McVey, B., Norman, C., Wood, N., Farritor, S., Arnold, R., Fateh, M., El-Sibaie, M., "Track Modulus Measurement From A Moving Railcar," *Proceedings of the AREMA 2005 Annual Conference, Chicago*, IL, September, 2005

McVey, B, A Nonlinear Approach to Measurement of Vertical Track Deflection From a Moving Railcar, Master Thesis, University of Nebraska – Lincoln, May 2006.

Meyer, Marcus B. 2002, “Measurement of Railroad Track Modulus on a Fast Moving Railcar,” Master Thesis, University of Nebraska – Lincoln, May 2002.

Norman, C., Measurement of Track Modulus From A Moving Railcar, Master Thesis, University of Nebraska – Lincoln, May 2004.

Raymond, G. P., 1985, “Analysis of Track Support and Determination of Track Modulus,” *Transportation Research Record* 1022, pp. 80-90.

Read, D., Chrismer, S., Ebersohn, W., and Selig, E., 1994, "Track Modulus Measurements at the Pueblo Soft Subgrade Site," *Transportation Research Record* 1470, pp. 55-64.

Selig, E. T., and Li, D., 1994, "Track Modulus: Its meaning and Factors Influencing It," *Transportation Research Record* 1470, pp. 47-54.

Stewart, Henry E., 1985, "Measurement and Prediction of Vertical Track Modulus," *Transportation Research Record* 1022, pp. 65-71.

Google map, http://maps.google.com.

Sussmann, T. R., Ebersohn, W., and Selig, E. T., 2001, "Fundamental Nonlinear Track Load-Deflection Behavior for Condition Evaluation," *Transportation Research Record* 1742, pp. 61-67.

Thompson, R., and Li, D., 2002, "Automated Vertical Track Strength Testing Using TTCI's Track Loading Vehicle," *Technology Digest*, February.

Wanek, Mischa, 2004, "Quality instruments for rail-flaw detection," *Railway Track and Structures,* February, pp. 19-22.

Zarembski, Allan M. and Choros, John. "On the measurement and calculation of vertical track modulus," *Proceedings of American Railway Engineering Association*, 1980, Vol. 81, pp. 156-173.

Zarembski, A. M., and Palese, J., August 2003, "Transitions eliminate impact at crossings," *Railway Track & Structures*, pp. 28-30.